PFC/RR-82-17 DOE/ET-51013-47

Coupling to the Fast Compressional Alfven Wave in Alcator A

by

Michael R. Sansone
Plasma Fusion Center
Massachusetts Institute of Technology
Cambridge, MA 02139

June 1982

COUPLING TO THE FAST COMPRESSIONAL ALFVEN-WAVE IN ALCATOR A

by

MICHAEL R. SANSONE

Submitted to the Department of Physics
on May 7, 1982 in partial fulfillment of the
requirements for the Degree of Master of Science in
Physics

ABSTRACT

The purpose of this experiment was to investigate the coupling efficiencies of the fast compressional Alfven-wave in order to evaluate its effectiveness for heating tokamaks to reactor temperatures. The parameters of the experiment were N_e = 1 - 5 x 10^{14} cm^{-3}, B_T = 40 - 80 KG, and f_o = 90 - 200 MHz.

Quadrature phase detection of eleven RF probes located in the toroidal direction was used to measure $k_{\parallel}$ and $k_{\perp}$. Both standing and traveling waves were observed, and $k_{\parallel}$ is typically found to be within the desirable range for heating (0.15 cm^{-1} - 0.5 cm^{-1}). For a variety of conditions, the RF probe signals qualitatively agree with the basic theories associated with the fast compressional Alfven-wave. Also, damping mechanisms are discussed in detail and compared to the experimental values of Q obtained by varying the toroidal magnetic field.

In this experiment, the torus is represented by a resonant cavity which is excited by a half-turn loop antenna located on the low field side of the minor cross section. By constructing an adjoint operator from Maxwell's equations a formal solution for calculating the antenna impedance is obtained. The main results are strong coupling near mode onset, and large radiation resistance for high Q eigenmodes. For propagation near the fundamental ion cyclotron frequency in a hydrogen plasma, the theoretical values of the antenna impedance closely agree with the experimental results. However, the radiation resistance for second harmonic regimes of hydrogen and deuterium plasmas are inconsistant with the previous theoretical model. For these conditions, there exists a background antenna loading which is linearly dependent on plasma density and has no observable cut-offs. The eigenmode component of the radiation resistance from the fast wave is small and is independant of the background loading. It is proposed that this is responsible for the poor heating efficiencies obtained during 100 kw heating experiments. A model based upon near field antenna coupling to a cold collisional edge plasma seems to explain the experimental background loading.

Thesis Supervisor: Dr. Ronald R. Parker

Title: Professor of Electrical Engineering and Computer Science

ACKNOWLEDGEMENTS

I would like to thank Dr. Ronald Parker for his insight and support during the course of this project. Without his strong interest in RF heating systems this experiment could not have been possible. I am also indebted to Dr. Boyd Blackwell for many fruitful discussions on wave propagation and for his guidance during the $k_{\parallel}$ measurements. In addition to the Alcator group, I would like to thank Dr. Martin Greenwald for providing charge exchange data. I am also deeply grateful for the technical support of Cornelius Holtjer, Paul Telasmanick, Marcel Gaudreau and Brian Abbanat.

Table of Contents

1. INTRODUCTION

Heating tokamaks to ignition temperature is one of the major problems arising in thermonuclear research. With present tokamak technology, the simplest and most economical method is ohmic heating. However, it becomes increasingly difficult to reach higher temperatures by this method alone because the plasma resistivity is proportional to $T_e^{-3/2}$, and the toroidal current is limited by MHD instabilities. Neutral beam injection and RF absorption are the prime candidates for supplementary heating of tokamaks to reactor-grade temperatures.

In the past few years, neutral beam injection has been very succesful in low density plasmas. This technique is impractical for the Alcator program because of the required beam energies for the high density regime. For this reason, plasma heating through the absorption of RF plasma waves seems to be a promising alternative. From a technological standpoint, there exists a large amount of RF power for frequencies up to a few gigaHertz, and as a result of this parameter range, several heating approaches need to be considered. Different approaches can selectively heat the ions or the electrons and modify either the bulk or the tail of the particle distribution function. The four major types of heating methods being explored today are:

1. Alfven-wave heating
2. Ion cyclotron harmonic heating
3. Lower hybrid wave heating
4. Electron cyclotron harmonic heating

With the unique tokamak facilities located at MIT, it is possible to examine the problems associated with heating high density plasmas. For the

past few years there has been a major effort in developing ion cyclotron harmonic heating for Alcator A, and at 200 MHz up to 100 kw of RF power has been coupled to the plasma. However, there was no noticeable change in the neutron flux rate, and the charge exchange signals had fast decay times, indicating the formation of energetic tails. In addition, the RF-enhanced charge exchange flux appeared when the cyclotron resonance was located near the plasma edge rather than in the center. Refer to Figure 1.1 for the RF-enhanced charge exchange flux as a function of the toroidal magnetic field and position of the resonance layer.

The prime motivation of this thesis was to gain insight into the poor heating efficiencies in the Alcator A experiment by investigating the problems of coupling to fast compressional Alfven-wave. By examining wave damping mechanisms for typical parameters in conjunction with the antenna impedance a global view of the coupling process can be obtained.

$n_e = 2.5 \times 10^{14}\,cm^{-3}$, HYDROGEN, SHIELDED ANTENNA (A4)

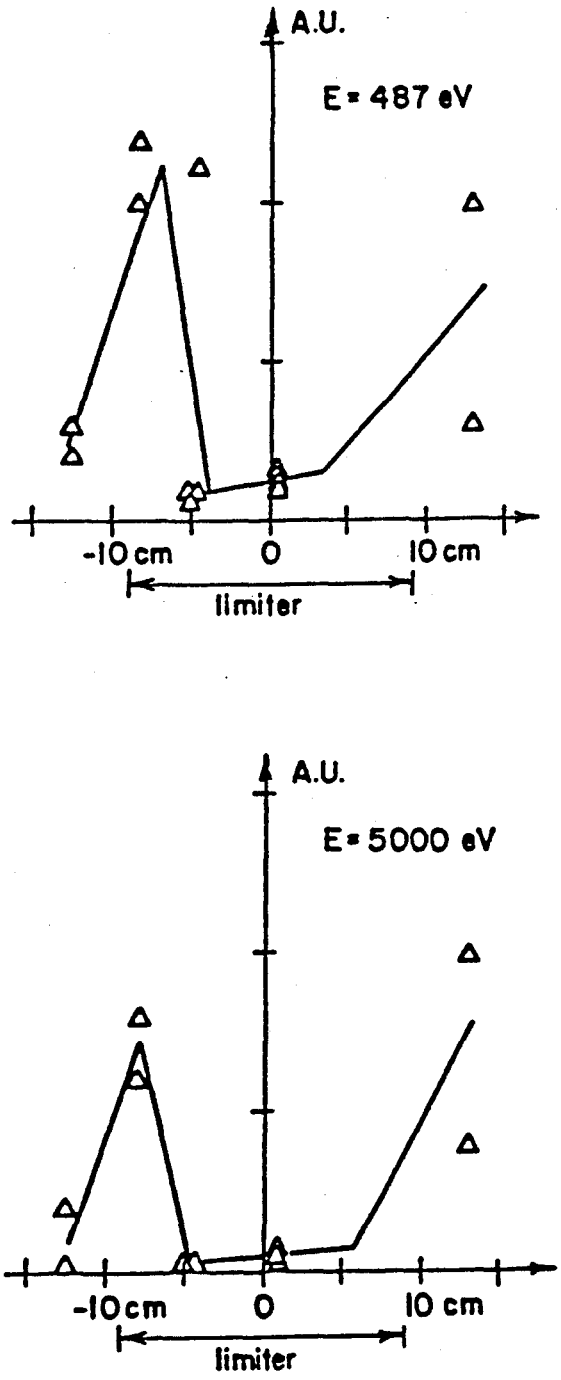

Figure 1.1. RF enhanced charge exchange flux vs. position of the $2W_{CH}$ layer.

2. ELECTROMAGNETIC WAVES IN A PLASMA

Electromagnetic wave propagation in any medium is described by the general set of Maxwell's equations:

$$\nabla \cdot \bar{E} = \rho/\epsilon_0 \tag{2.1}$$

$$\nabla \times \bar{E} = -\mu_0 \frac{\partial \bar{H}}{\partial t} \tag{2.2}$$

$$\nabla \cdot (\mu_0 \bar{H}) = 0 \tag{2.3}$$

$$\nabla \times \bar{H} = \epsilon_0 \frac{\partial \bar{E}}{\partial t} + \bar{J} \tag{2.4}$$

In order to utilize Maxwell's equation for wave propagation in a plasma it is useful to express the plasma current density $\bar{J}$ and the charge density ρ in terms of the local electric field $\bar{E}$. In a plasma the current $\bar{J}$ is simply proportional to the sum of particle velocities $\bar{V}_\ell$ by:

$$\bar{J} = \sum_\ell n_\ell Z_\ell \epsilon_\ell e \bar{V}_\ell \tag{2.5}$$

In this equation n_ℓ is the density of particles with charge eZ_ℓ and ϵ_ℓ is the sign of the charge. In order to relate $\bar{V}_\ell$ and ultimately $\bar{J}$ to the electric field one must solve the equation of motion for a single particle. The induced motion for a particle resulting from the Lorentz force is:

$$m_\ell \frac{d\bar{V}_\ell}{dt} = z_\ell \epsilon_\ell e(\bar{E} + \bar{V}_\ell \times \bar{B}) \tag{2.6}$$

For the present treatment we assume that the density and background magnetic field are static in time and uniform in space. All other quantities are assumed to vary as $\exp j(\bar{k} \cdot \bar{r} - \omega t)$. Fourier analyzing in time and assuming

no zero-order velocities $d\bar{V}_\ell/dt \rightarrow -j\omega\bar{V}_\ell$ to first order.

$$-j\omega m_\ell \bar{V}_\ell = Z\varepsilon_\ell e(\bar{E} + \bar{V}_\ell \times \bar{B}) \tag{2.7}$$

If the background magnetic field is in the z direction and the cold plasma approximation is used, then the solution to Equation 2.7 is (where the particle subscript has been suppressed):

$$V_x = j\frac{\varepsilon\omega_c}{\omega B_0}\frac{(E_x + j\frac{\varepsilon\omega_c}{\omega}E_y)}{(1 - \omega_c^2/\omega^2)} \tag{2.8}$$

$$V_y = j\frac{\varepsilon\omega_c}{\omega B_0}\frac{(E_y - j\frac{\varepsilon\omega_c}{\omega}E_x)}{(1 - \omega_c^2/\omega^2)} \tag{2.9}$$

$$V_z = j\frac{\varepsilon\omega_c}{B_0\omega}E_z \quad \text{where} \quad \omega_c = \frac{ZeB_0}{M} \tag{2.10}$$

With these solutions, the plasma current $\bar{J}$ can be expressed as a function of the electric field rather than of the particle velocity. The total displacement $\bar{D}$ and the dielectric coefficient $\bar{\bar{K}}$ are defined as:

$$\bar{D} = \varepsilon_0\bar{\bar{K}} \cdot \bar{E} = \varepsilon_0\bar{E} + \frac{\bar{J}}{j\omega} \tag{2.11}$$

Equation 2.4 now takes the form $\nabla \times \bar{H} = j\omega\varepsilon_0\bar{\bar{K}} \cdot \bar{E}$. By substituting equations 2.5, 2.8, 2.9 and 2.10 into 2.11, the dielectric tensor $\bar{\bar{K}}$ may be written as follows [1]:

$$\varepsilon_0 \bar{\bar{K}} \cdot \bar{E} = \begin{bmatrix} K_\perp & -K_x & 0 \\ K_x & K_\perp & 0 \\ 0 & 0 & K_\parallel \end{bmatrix} \begin{bmatrix} E_x \\ E_y \\ E_z \end{bmatrix} \tag{2.12}$$

$$K_\perp = \frac{R + L}{2}$$

$$-jK_x = \frac{R - L}{2}$$

$$R = 1 - \sum_{\ell} \frac{\omega_{p\ell}^2}{\omega^2} \left(\frac{\omega}{\omega + \varepsilon_\ell \omega_{c\ell}} \right)$$

$$L = 1 - \sum_{\ell} \frac{\omega_{p\ell}^2}{\omega^2} \left(\frac{\omega}{\omega - \varepsilon_\ell \omega_{c\ell}} \right)$$

$$K_\parallel = 1 - \sum \frac{\omega_{p\ell}}{\omega^2}$$

where ℓ is the sum over all particle species.

In order to rewrite Equation 2.1 in terms of the electric field the continuity equation is used.

$$\frac{\partial \rho}{\partial t} + \nabla \cdot J = 0$$

$$\rho = \frac{1}{j\omega} \nabla \cdot J$$

Substituting this into Equation 2.1 and using Equation 2.11 yields:

$$\nabla \cdot (\varepsilon_0 \bar{\bar{K}} \cdot \bar{E}) = 0 \tag{2.13}$$

Wave propagation in a plasma is now summarized by Equations 2.2, 2.3, 2.4 and 2.13.

The dispersion relationship for wave propagation is found by taking the curl of Equation 2.2 and substituting the result into Equation 2.4.

$$\nabla \times (\nabla \times \bar{E}) = k_0^2 \bar{\bar{K}} \cdot \bar{E} \qquad \text{where } k_0 = \frac{\omega}{c} \tag{2.14}$$

Defining a refractive index $\bar{n} = \bar{k}c/\omega$ and assuming $n_y = 0$, Equation 2.14 can be written as:

$$\begin{bmatrix} K_\perp - n_\parallel^2 & -K_x & n_x n_\parallel \\ K_x & K_\perp - (n_x^2 + n_\parallel^2) & 0 \\ n_x n_\parallel & 0 & K_\parallel - n_x^2 \end{bmatrix} \begin{bmatrix} E_x \\ E_y \\ E_z \end{bmatrix} = 0 \tag{2.15}$$

The general dispersion relation is obtained by setting the determinant of equation 2.15 equal to zero. Using the quadratic equation to solve for $k_\parallel^2$ the dispersion relationship becomes:

$$k_\parallel^2 = k_0^2 K_\perp - \tfrac{1}{2} k_\perp^2 \left(\frac{K_\perp}{K_\parallel} + 1 \right) \pm \sqrt{\frac{k_\perp^4}{4} \left(\frac{K_\perp}{K_\parallel} - 1 \right)^2 - k_0^4 K_x^2 \left(1 - \frac{k_\perp^2}{k_0^2 K_\parallel} \right)} \tag{2.16}$$

where $k_\parallel = \frac{\omega}{c} n_\parallel$ and $k_\perp = \frac{\omega}{c} n_x$

For a two component plasma in the regime where $\omega \sim \omega_{ci}$ and $\omega_{pi}^2 >> \omega_{ci}$ the dielectric tensor elements from Equation 2.12 simplifies to:

$$k_\perp \cong \frac{\omega_{pi}^2}{\omega_{ci}^2} \left(\frac{1}{1 - \Omega^2} \right) \tag{2.17}$$

$$jK_x \cong \frac{\omega_{pi}^2}{\omega_{ci}^2} \left(\frac{\Omega}{1 - \Omega^2} \right) \tag{2.18}$$

$$K_\parallel \cong - \frac{\omega_{pe}^2}{\omega^2} \qquad \text{where } \Omega = \frac{\omega}{\omega_{ci}} \text{ and } \frac{\omega_{pe}^2}{\omega_{ce}} = \frac{\omega_{pi}^2}{\omega_{ci}} \tag{2.19}$$

Since $\omega_{pe}^2 >> \omega^2$ it is reasonable to assume $K_{\parallel} \to \infty$. Using this approximation and Equations 2.17 and 2.18 the dispersion relationship 2.16 simplifies to:

$$k_{\parallel}^2 = \frac{k_{\perp}^2}{2(1 - \Omega^2)} \left[2\left(\frac{k_A}{k_{\perp}}\right)^2 - (1 - \Omega^2) \pm \sqrt{(1 - \Omega^2)^2 + 4\Omega^2\left(\frac{k_A}{k_{\perp}}\right)^4} \right] \quad (2.20)$$

where $k_A = \frac{\omega}{V_A}$ and $V_A^2 = \frac{B^2}{4\pi n_i m_i}$

In this equation the positive root represents the fast compressional Alfven wave or sometimes referred to as the fast magnetosonic wave. The negative root is generally evanescent in the bulk of the plasma and therefore of little interest in this class of problems.

For typical experimental conditions the following approximation is reasonable:

$$(1 - \Omega^2)^2 << 4\Omega^2\left(\frac{k_A}{K_{\perp}}\right)^4$$

In light of this statement, Equation 2.20 further reduces to:

$$k_{\parallel}^2 + \tfrac{1}{2}k_{\perp}^2 = \frac{k_A^2}{1 \pm \Omega} \quad (2.21)$$

3. GUIDED ELECTROMAGNETIC WAVES

3.1 General Solution

A guided electromagnetic wave usually implies that the direction of energy flow is primarily determined by a physical boundary. This requires an intimate connection between the fields of the wave and the currents and charges in the boundary. In comparison, the direction of energy flow for unguided waves is determined by the local group velocity of the wave and not by the physical boundaries. For most damping parameters in this experiment a wave launched by the antenna radially traverses the plasma with little absorption and is reflected off the opposing wall. This signifies that a guided wave approach is more useful than ray tracing for determining the complete field structure in the system.

The wave guide system that we are interested in solving is illustrated below.

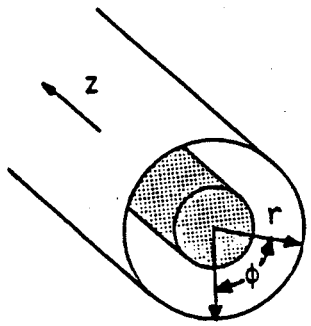

It consists of a cylindrical plasma enclosed by a perfectly conducting wall and a constant magnetic field in the z-direction. The plasma parameters are assumed to be independent of r, ϕ, and z. In the mathmatical analysis of

the problem we are required to find solutions of the wave equation which fit the boundary conditions of the wall. In the RF community it is common to classify wave propagation into 3 basic categories.

1) TEM: Transverse electromagnetic waves contain neither electric nor magnetic fields in the direction of propagation.

2) TM: Transverse magnetic waves contain electric fields but not magnetic fields in the direction of propagation ($H_z = 0$).

3) TE: Transverse electric waves contain magnetic fields but not electric fields in the direction of propagation ($E_z = 0$).

Typically solutions are more complex and will contain a mixture of these modes. The best methodology in solving such a problem is to formulate Maxwell's equations in terms of the field quantities E_z and H_z. In this way for suitable approximations the solutions break up into TEM, TM and TE modes which give physical insight to complex mode structure.

In the previous chapter we have eliminated $\bar{J}$ and ρ from Maxwell's equations and the only unknown functions are the fields $\bar{E}$ and $\bar{H}$. Maxwell's equations can now be written as:

$$\nabla \times \bar{E} = -j\omega\mu_0\bar{H} \tag{3.1}$$

$$\nabla \times \bar{H} = j\omega\varepsilon_0\bar{\bar{K}} \cdot \bar{E} \tag{3.2}$$

$$\nabla \cdot (\varepsilon_0\bar{\bar{K}} \cdot \bar{E}) = 0 \tag{3.3}$$

$$\nabla \cdot (\mu_0\bar{H}) = 0 \tag{3.4}$$

For the class of boundary conditions in this problem it is convenient to separate all fields into tangential and longitudinal terms. Assuming a "z" dependence of the form $\exp(-\gamma z)$ and $K_\perp$, K_x, $K_\parallel$ are radially independent, we proceed as follows[2] :

$$\bar{E} = \bar{E}_T + \hat{i}_z E_z \tag{3.5}$$

$$\bar{H} = \bar{H}_T + \hat{i}_z H_z \tag{3.6}$$

$$\nabla = \nabla_T - \hat{i}_z \gamma \tag{3.7}$$

$$\bar{\bar{K}} \cdot \bar{E} = \bar{\bar{K}}_T \cdot \bar{E}_T + \hat{i}_z K_{\parallel} E_z = K_{\perp} \bar{E}_T + K_x \hat{i}_z \times E_T + \hat{i}_z K_{\parallel} E_z \tag{3.8}$$

In the equations above a subscript T indicates that a vector lies in a plane perpendicular to the z direction. In order to facilitate problem solving later on, it is convenient to write Maxwell's equations in terms of the field quantities E_z and H_z as noted before. First to find the H_z component dot-multiply $\hat{i}_z$ with Equation 3.1 and substitute in Equations 3.5, 3.6 and 3.7:

$$\hat{i}_z \cdot \nabla \times \bar{E} = -\omega \mu_0 \hat{i}_z \cdot \bar{H}$$

$$\hat{i}_z \cdot (\nabla_T - \hat{i}_z \gamma) \times (\bar{E}_T + \hat{i}_z E_z) = -j\omega \mu_0 \hat{i}_z \cdot (\bar{H}_T + \hat{i}_z H_z)$$

$$\hat{i}_z \cdot \nabla_T \times \bar{E}_T = -j\omega \mu_0 H_z \tag{3.9}$$

In a similar manner the E_z component is found by dot-multiplying $\hat{i}_z$ with Eq. 3.2 and substituting in Equations 3.6, 3.7 and 3.8:

$$\hat{i}_z \cdot \nabla \times \bar{H} = j\omega \varepsilon_0 \hat{i}_z \cdot \bar{\bar{K}} \cdot \bar{E}$$

$$\hat{i}_z \cdot (\nabla_T - \hat{i}_z \gamma) \times (\bar{H}_T + \hat{i}_z H_z) = j\omega \varepsilon_0 \hat{i}_z \cdot (K_{\perp} \bar{E}_T + K_x \hat{i}_z \times \bar{E}_T + \hat{i}_z K_{\parallel} E_z)$$

This simplifies to:

$$\hat{i}_z \cdot \nabla_T \times \bar{H}_T = j\omega \varepsilon_0 K_{\parallel} \bar{E}_z \tag{3.10}$$

The general wave equation can be written as two second-order differential equations in H_z and E_z. These equations are coupled through first order differential terms and to find the E_z equation, cross-multiply $\hat{i}_z$ with Equation 3.1. Then

substitute in Equations 3.5, 3.6, and 3.7:

$$\hat{i}_z \times (\nabla \times \bar{E}) = -j\omega\mu_0 \hat{i}_z \times \bar{H}$$

$$\hat{i}_z \times [(\nabla_T - \hat{i}_z\gamma) \times (\bar{E}_T + \hat{i}_z E_z)] = -j\omega\mu_0 \hat{i}_z \times (\bar{H}_T + \hat{i}_z H_z)$$

Note: $\hat{i}_z \times (\nabla_T \times \hat{i}_z E_z) = \nabla_T E_z$

$$\nabla_T E_z + \gamma \bar{E}_T = -j\omega\mu_0 \hat{i}_z \times \bar{H}_T \tag{3.11}$$

Dot multiply ∇_T with Equation 3.11:

$$\nabla_T^2 E_z + \gamma \nabla_T \cdot \bar{E}_T = -j\omega\mu_0 \nabla_T \cdot (\hat{i}_z \times \bar{H}_T)$$

Note: $\nabla_T \cdot (\hat{i}_z \times \bar{H}_T) = -i_z \cdot \nabla_T \times \bar{H}_T$

$$\nabla_T^2 E_z + \gamma \nabla_T \cdot \bar{E}_T = j\omega\mu_0 \hat{i}_z \cdot \nabla_T \times \bar{H}_T$$

Substitution of Equation 3.10 yields:

$$\nabla_T^2 E_z + \gamma \nabla_T \cdot \bar{E}_T = -\omega^2 \varepsilon_0 \mu_0 K_{\shortparallel} E_z = -k_0^2 K_{\shortparallel} E_z \tag{3.12}$$

where $k_0^2 = \omega^2 \varepsilon_0 \mu_0$. Using Equation 3.3 along with Equations 3.5, 3.7, 3.8 and 3.9 provides an expression for the term $\gamma \nabla_T \cdot \bar{E}_T$:

$$\nabla \cdot (\varepsilon_0 \bar{\bar{K}} \cdot \bar{E}) = 0$$

$$(\nabla_T - \hat{i}_z\gamma) \cdot \varepsilon_0 (K_{\perp} \bar{E}_T + K_x \hat{i}_z \times \bar{E}_T + \hat{i}_z K_{\shortparallel} E_z) = 0$$

Note: $\nabla_T \cdot (\hat{i}_z \times \bar{E}_T) = -\hat{i}_z \cdot \nabla_T \times \bar{E}_T$

$$K_{\perp} \nabla_T \cdot \bar{E}_T = \gamma K_{\shortparallel} E_z + K_x \hat{i}_z \cdot \nabla_T \times \bar{E}_T = \gamma K_{\shortparallel} E_z - j\omega\mu_0 K_x H_z \tag{3.13}$$

Combining Equations 3.12 and 3.13 provides the first differential equation that we set out to derive:

$$\nabla_T^2 E_z + \frac{K_{\parallel}}{K_{\perp}} (k_0^2 K_{\perp} + \gamma^2) E_z - j\frac{K_x}{K_{\perp}} \omega \mu_0 \gamma H_z = 0$$

The remaining differential equation is found by cross-multiplying $\hat{i}_z$ with Equation 3.2 and substituting in Equations 3.6, 3.7 and 3.8:

$$\hat{i}_z \times (\nabla \times \bar{H}) = j\omega\varepsilon_0 \hat{i}_z \times (\bar{\bar{K}} \cdot \bar{E})$$

Note: $\hat{i}_z \times (\nabla_T \times \hat{i}_z H_z) = \nabla_T H_z$

$$\hat{i}_z \times [(\nabla_T - \hat{i}_z \gamma) \times (\bar{H}_T + \hat{i}_z H_z)] = j\omega\varepsilon_0 \hat{i}_z \times [K_{\perp} \bar{E}_T + K_x \hat{i}_z \times \bar{E}_T + \hat{i}_z K_{\parallel} E_z]$$

$$\nabla_T H_z + \gamma \bar{H}_T = j\omega\varepsilon_0 K_{\perp} \hat{i}_z \times \bar{E}_T - j\omega\varepsilon_0 K_x \bar{E}_T \qquad (3.15)$$

Dot multiply ∇_T with Equation 3.15:

$$\nabla_T^2 H_z + \gamma \nabla_T \cdot \bar{H}_T = j\omega\varepsilon_0 K_{\perp} \nabla_T \cdot (\hat{i}_z \times \bar{E}_T) - j\omega\varepsilon_0 K_x \nabla_T \cdot \bar{E}_T$$

Note: $\nabla_T \cdot (\hat{i}_z \times \bar{E}_T) = -\hat{i}_z \cdot \nabla_T \times \bar{E}_T$

$$\nabla_T^2 H_z + \gamma \nabla_T \cdot \bar{H}_T = -j\omega\varepsilon_0 K_{\perp} \hat{i}_z \cdot \nabla_T \times \bar{E}_T - j\omega\varepsilon_0 K_x \ \nabla_T \cdot \bar{E}_T$$

Substitution of Equations 3.9 and 3.13:

$$\nabla_T^2 H_z + \gamma \nabla_T \cdot \bar{H}_T = - k_0^2 K_{\perp} H_z - j\gamma\omega\varepsilon_0 \frac{K_x}{K_{\perp}} K_{\parallel} E_z - k_0^2 \frac{K_x^2}{K_{\perp}} H_z \qquad (3.16)$$

Combining Equations 3.4 and 3.6 expresses $\nabla_T \cdot \bar{H}_T$ in terms of H_z:

$$\nabla \cdot (\mu_0 \bar{H}) = 0$$

$$\mu_0(\nabla_T - \hat{i}_z\gamma) \cdot (\bar{H}_T + \hat{i}_z H_z) = 0$$

$$\nabla \cdot \bar{H}_T = \gamma H_z \tag{3.17}$$

Substitution of Equation 3.17 into 3.16 produces the final differential equation:

$$\nabla_T^2 H_z + H_z\left(\gamma^2 + k_0^2 K_\perp + k_0^2 \frac{K_x^2}{K_\perp}\right) + j\omega\varepsilon_0\gamma \frac{K_x K_{\shortparallel}}{K_\perp} E_z = 0 \tag{3.18}$$

In order to complete the solution the tangential fields must be expressed in terms of E_z and H_z. It is useful to write Equations 3.11, 3.15, and i_z cross-multiplied with Equations 3.11 and 3.15 in matrix form as follows:

$$M \begin{bmatrix} \bar{E}_T \\ \bar{H}_T \\ \hat{i}_z \times \bar{E}_T \\ \hat{i}_z \times \bar{H}_T \end{bmatrix} = \begin{bmatrix} \nabla_T E_z \\ \nabla_T H_z \\ \hat{i}_z \times \nabla_T E_z \\ \hat{i}_z \times \nabla_T H_z \end{bmatrix} \tag{3.19}$$

$$M = \begin{bmatrix} -\gamma & 0 & 0 & -j\omega\mu_0 \\ -j\omega\varepsilon_0 K_x & -\gamma & j\omega\varepsilon_0 K_\perp & 0 \\ 0 & -j\omega\mu_0 & -\gamma & 0 \\ -j\omega\varepsilon_0 K_\perp & 0 & -j\omega\varepsilon_0 K_x & -\gamma \end{bmatrix} \tag{3.20}$$

It is possible to solve for $\bar{E}_T$, $\bar{H}_T$, $\hat{i}_z \times \bar{E}_T$, $\hat{i}_z \times \bar{H}_T$. Multiply Equation 3.19 by M^{-1} where $MM^{-1} = I$:

$$\begin{bmatrix} \bar{E}_T \\ \bar{H}_T \\ \hat{i}_z \times \bar{E}_T \\ \hat{i}_z \times \bar{H}_T \end{bmatrix} = M^{-1} \begin{bmatrix} \nabla_T E_z \\ \nabla_T H_z \\ \hat{i}_z \times \nabla_T E_z \\ \hat{i}_z \times \nabla_T H_z \end{bmatrix} \tag{3.21}$$

$$M^{-1} = \begin{bmatrix} P & R & Q & S \\ T & P & U & Q \\ -Q & -S & P & R \\ -U & -Q & T & P \end{bmatrix} \tag{3.22}$$

$$P = \frac{-\gamma(\gamma^2 + k_0^2 K_\perp)}{D}$$

$$R = \frac{j\omega\mu_0 k_0^2 K_X}{D}$$

$$Q = \frac{\gamma k_0^2 K_X}{D}$$

$$S = \frac{j\omega\mu_0(\gamma^2 + k_0^2 K_\perp)}{D}$$

$$T = \frac{\gamma^2 j\omega\varepsilon_0 K_X}{D}$$

$$U = \frac{-j\omega\varepsilon_0(\gamma^2 K_\perp + k_0^2)}{D}$$

$$D = (\gamma^2 + k_0^2 K_\perp)^2 + (k_0^2 K_X)^2$$

In summary, Maxwell's equations can be expressed in terms of E_z and H_z as follows:

$\gamma = j\beta$ where β is the propagation constant in the z direction.

$$\nabla_T^2 H_z + H_z \left[k_0^2 \left(K_\perp + \frac{K_x^2}{K_\perp} \right) - \beta^2 \right] + \beta \omega \varepsilon_0 \frac{K_x K_\parallel}{K_\perp} E_z = 0 \qquad (3.23)$$

$$\nabla_T^2 E_z + E_z \left(k_0^2 K_\parallel - \frac{K_\parallel}{K_\perp} \beta^2 \right) - \beta \frac{K_x}{K_\perp} \omega \mu_0 H_z = 0 \qquad (3.24)$$

The tangential fields are given by Equations 3.21 and 3.22.

3.2 Free-space Waveguide

This simple case demonstrates the usefulness of writing Maxwell's equation in terms of the z component of the fields. If the wave guide system contains no plasma then $K_x = 0$ and $K_\perp = K_\parallel = 1$. In this situation one obtains from Equations 3.23 and 3.24 two uncoupled wave equations for E_z and H_z. The tangential fields are obtained from Equation 3.21.

TE Waves

$$E_z = 0$$

$$\nabla_T^2 H_z + (k_0^2 - \beta^2) H_z = 0$$

$$\bar{H}_T = \frac{-j\beta}{(k_0^2 - \beta^2)} \nabla_T H_z$$

$$\bar{E}_T = \frac{j\omega\mu_0}{(k_0^2 - \beta^2)} i_z \times \nabla_T H_z$$

TM Waves

$$H_z = 0$$

$$\nabla_T^2 E_z + (k_0^2 - \beta^2) E_z = 0$$

$$\bar{E}_T = \frac{-j\beta}{(k_0^2 - \beta^2)} \nabla_T E_z$$

$$\bar{H}_T = \frac{-j\omega\varepsilon_0}{(k_0^2 - \beta^2)} i_z \times \nabla_T E_z$$

For cylindrical geometry $H_z \sim J_m(\rho r)$ for TE waves. The boundary condition at the wall implies $E_\phi = 0$ and $H_r = 0$ which means $dJ_m(\rho r)/dr = 0$ at $r = a$. For TM waves $E_z \sim J_m(\rho r)$ and the boundary conditions are $E_z = 0$, $E_\phi = 0$ and $H_r = 0$ which means $J_m(\rho r) = 0$ at $r = a$. These relations determine the cutoff wavelengths for the TE and TM modes. The table[3] below shows the cutoff wavelengths and frequency for a cavity the size of the Alcator A vacuum vessel ($a = 10$ cm). Since the lowest frequency that can propagate is the TE_{11} mode at 879 MHz, one would infer that no cavity excitation will occur in the absence of plasma for the frequencies employed in this experiment.

TE Mode	λ_c	f_c(MHz)	TM Mode	λ_c	f_c(MHz)
TE_{01}	1.64 a	1,829	TM_{01}	2.61 a	1,149
TE_{02}	0.89 a	3,371	TM_{02}	1.14 a	2,632
TE_{11}	3.41 a	879	TM_{11}	1.64 a	1,829
TE_{12}	1.18 a	2,542	TM_{12}	0.89 a	3,371
TE_{21}	2.06 a	1,456	TM_{21}	1.22 a	2,459
TE_{31}	1.49 a	2,013	TM_{31}	0.98 a	3,061
TE_{41}	1.18 a	2,542	TM_{41}	0.83 a	3,614

3.3 Plasma-Filled Waveguide

If the waveguide contains a homogeneous plasma and a magnetic field in the z direction, then Field Equations 3.23 and 3.24 are coupled. The formal solution to this problem is quite tedious but fortunately reasonable approximations do exist. For the major portion of an Alcator A plasma the approximation $K_{\parallel} \to \infty$ is reasonable. For $K_{\parallel} \to \infty$ and realistic values of ρ^2, Equation 3.24 implies:

$$\nabla_T^2 E_z << E_z\left(k_0^2 K_{\parallel} - \frac{K_{\parallel}}{K_{\perp}}\beta^2\right)$$

E_z can therefore be expressed as:

$$K_{\parallel} E_z \approx \frac{\beta K_x \omega \mu_0}{(k_0^2 K_{\perp} - \beta^2)} H_z \qquad (3.25)$$

The field equation governing wave propagation under these conditions is:

$$\nabla_T^2 H_z + H_z\left[k_0^2 K_{\perp} + k_0^2 \frac{K_x^2}{K_{\perp}} - \beta^2 + \frac{\beta^2 k_0^2 \frac{K_x^2}{K_{\perp}}}{k_0^2 K_{\perp} - \beta^2}\right] = 0 \qquad (3.26)$$

The solution to this equation in cylindrical coordinates is simply of the form:

$$H_z = \hat{H} J_m(\rho r) e^{jm\phi} \qquad (3.27)$$

where $\rho^2 = k_0^2 K_{\perp} + k_0^2 \frac{K_x}{K_{\perp}} - \beta^2 + \frac{\beta^2 k_0^2 \frac{K_x^2}{K_{\perp}}}{k_0^2 K_{\perp} - \beta^2}$

The remaining field quantities are derived from Equation 3.21 with E_z set to zero:

$$H_r = \left(P\rho \frac{J_m'(\rho r)}{J_m(\rho r)} - \frac{jmQ}{r} \right) H_z \tag{3.28}$$

$$H_\phi = \left(\frac{jmP}{r} + Q\rho \frac{J_m'(\rho r)}{J_m(\rho r)} \right) H_z \tag{3.29}$$

$$E_r = \left(R\rho \frac{J_m'(\rho r)}{J_m(\rho r)} - \frac{jmS}{r} \right) H_z \tag{3.30}$$

$$E_\phi = \left(\frac{jRm}{r} + S\rho \frac{J_m'(\rho r)}{J_m(\rho r)} \right) H_z \tag{3.31}$$

$$E_z = 0 \tag{3.32}$$

These solutions must also conform to the boundary conditions at the wall. At the wall $E_\phi(r = a) = 0$ and Equation 3.31 results in the following boundary value equation:

$$\frac{J_m'(\rho a)}{J_m(\rho a)} = \frac{-jm}{\rho a} \frac{k_0^2 K_x}{(k_0^2 K_\perp - \beta^2)} \tag{3.33}$$

This equation in conjunction with the dispersion relationship completely discribes the wave propagation in infinite waveguide system. For $\beta = 0$, Equation 3.33 provides the cutoff relation for propagation:

$$\frac{J_m'(\rho a)}{J_m(\rho a)} = \frac{-jm}{a} \frac{K_x}{K_\perp} \tag{3.34}$$

For a single ion species plasma this becomes:

$$\frac{J_m'(\rho a)}{J_m(\rho a)} = \frac{-m}{\rho a} \frac{\omega}{\omega_{ci}}$$

Figure 3.1 shows the solution for Equation 2.20 and 3.34 in a pure hydrogen plasma with $\omega = 2\omega_{ci}$ when "ρ" is constant after mode onset. $k_{\parallel}$ or β is shown as a function of density in this plot and for increasing densities higher order radial and poloidal modes can propagate.

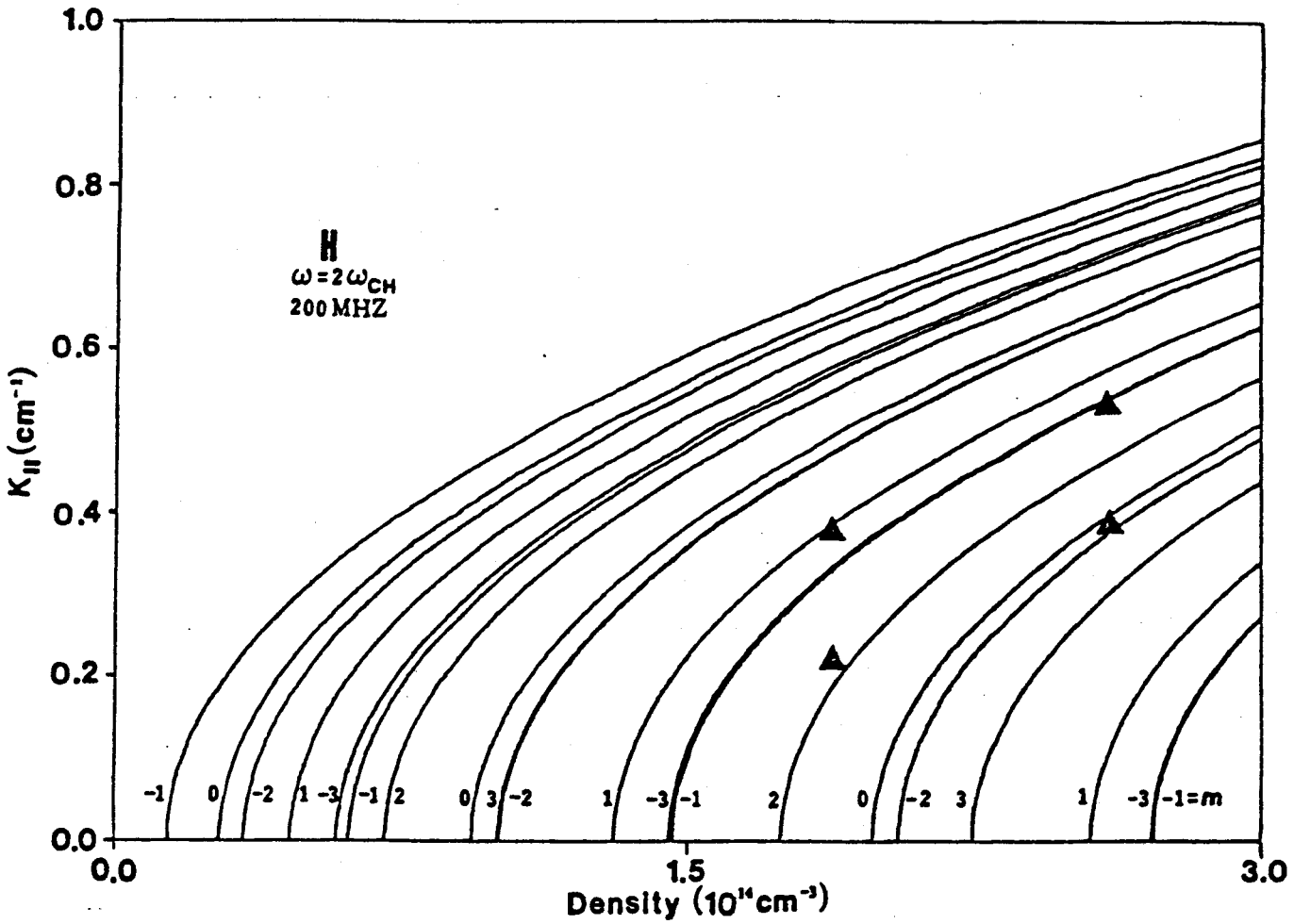

Figure 3.1. Dispersion relationship for the fast compressional Alfven wave in a hydrogen plasma with a 10 cm radius. Triangles are experimental data points that are obtained in Chapter 7.

4. CALCULATION OF ANTENNA IMPEDANCE

By solving Maxwell's equations for a plasma filled waveguide we have generated a set of solutions containing a discrete spectrum of radial and poloidal modes. The problem that has to be solved now is how an aperature or loop antenna couples to the modes of the undriven system. In aperature coupling, the fields set up in the openings of a waveguide or resonant slot are responsible for the excitation of the plasma waves. In Alcator A this scheme was not feasible because of the small port size. In loop coupling the inductive fields from currents flowing along the antenna structure produce wave propagation. In this experiment loop coupling was chosen because of mechanical constraints and the excellent coupling of the loop to the fast compressional Alfven-wave.

4.1 Infinte Waveguide

In analyzing the problem for loop coupling,* it is useful to write Maxwell's equations in terms of the perpendicular electric fields. We must also include a source term $\bar{J}_s$ which will represent the Fourier analyzed antenna current and ultimately excite the modes.

$$\nabla \times \bar{E} = -j\omega\mu_0\bar{H} \tag{4.1}$$

$$\nabla \times \bar{H} = j\omega\varepsilon_0\bar{\bar{K}} \cdot \bar{E} + \bar{J}_s \tag{4.2}$$

$$\nabla \cdot (\varepsilon_0\bar{\bar{K}} \cdot \bar{E}) = 0 \tag{4.3}$$

Taking the curl of Equation 4.1 and substituting Equation 4.2 yields:

$$\nabla \times (\nabla \times \bar{E}) = k_0^2\bar{\bar{K}} \cdot \bar{E} - j\omega\mu_0\bar{J}_s$$

* Derivation follows reference 4.

Again, it is convenient to separate all quantities into longitudinal and tangential parts:

$$(\nabla_T - j\beta\,\hat{i}_z) \times (\nabla_T - j\beta\hat{i}_z) \times (\bar{E}_T + \hat{i}_z E_z) = k_0^2(\bar{\bar{K}}_T \cdot \bar{E}_T + \hat{i}_z K_{\shortparallel} E_z) - j\omega\mu_0 J_s$$

$$\nabla_T \times \nabla_T \times \bar{E}_T + \nabla_T \times \nabla_T \times \hat{i}_z E_z - j\beta\nabla_T \times \hat{i}_z \times \bar{E}_T - j\beta\hat{i}_z \times \nabla_T \times \hat{i}_z E_z + \beta^2 \bar{E}_T$$

$$= k_0^2(\bar{\bar{K}}_T \cdot \bar{E}_T + \hat{i}_z K_{\shortparallel} E_z) - j\omega\mu_0 \bar{J}_s$$

By substituting Equations 3.10 and 3.11 of the previous section, this equation simplifies to:

$$\nabla_T \times \nabla_T \times \bar{E}_T + \beta^2 \bar{E}_T - j\beta\nabla_T E_z = k_0^2 \bar{\bar{K}}_T \cdot \bar{E}_T - j\omega\mu_0 \bar{J}_s \qquad (4.4)$$

From Equation 4.3 we find an equation for E_z in terms of $\bar{E}_T$:

$$\nabla \cdot (\bar{\bar{K}} \cdot \bar{E}) = (\nabla_T - j\beta\hat{i}_z) \cdot (\bar{\bar{K}}_T \cdot \bar{E}_T + \hat{i}_z K_{\shortparallel} E_z) = 0$$

$$E_z = -\frac{j}{\beta K_{\shortparallel}} \nabla_T \cdot (\bar{\bar{K}}_T \cdot \bar{E}_T)$$

Equation 4.4 becomes:

$$\nabla_T \times \nabla_T \times \bar{E}_T - \nabla_T \frac{1}{K_{\shortparallel}} \nabla_T \cdot (\bar{\bar{K}}_T \cdot \bar{E}_T) - k_0^2 \bar{\bar{K}}_T \cdot \bar{E}_T + \beta^2 \bar{E}_T = -j\omega\mu_0 \bar{J}_s \qquad (4.5)$$

Equation 4.5 may be written more compactly in terms of an operator L as follows:

$$L \cdot \bar{E}_T + \beta^2 \bar{E}_T = -j\omega\mu_0 \bar{J}_s \qquad (4.6)$$

where

$$L = \nabla_T \times \nabla_T \times \mathbf{1} - \nabla_T \frac{\mathbf{1}}{TK_{\parallel}} \nabla_T \cdot K_{\perp} - k_0^2 K_{\perp} \qquad \mathbf{1} \text{ is the unit dyadic.}$$

It should be noted that the homogeneous wave equation is obtained by setting $J_s = 0$ in Equation 4.6:

$$L \cdot \bar{\varepsilon}_{Ti} + \beta_i^2 \bar{\varepsilon}_{Ti} = 0 \tag{4.7}$$

Equation 4.7 constitutes an eigenvalue problem of the operator L where $\bar{\varepsilon}_{Ti}$ represents the eigenvectors and β_i the eigenvalues of the i^{th} mode. If $\bar{E}_T$ and $\bar{J}_s$ can be expanded in terms of $\bar{\varepsilon}_{Ti}$ then a formal solution to Equation 4.6 can be found. For the expansion to be valid, $\bar{E}_{Ti}$ must be represented by a complete orthogonal set of $\bar{\varepsilon}_{Ti}$. However, in general the set of $\bar{\varepsilon}_{Ti}$ are not orthogonal for an arbitrary operator L. For example, when two modes are present the total electric field at one point is $\bar{E} = \bar{E}_1 + \bar{E}_2$ and the total magnetic field is $\bar{H} = \bar{H}_1 + \bar{H}_2$. The Poynting flux in this case is:

$$S = \frac{1}{2} \mathrm{Re} \oint_s \bar{E} \times \bar{H}^* d\bar{s} = \frac{1}{2} \mathrm{Re} \oint_s (\bar{E}_1 \times \bar{H}_1^* + \bar{E}_2 \times \bar{H}_2^* + \bar{E}_1 \times \bar{H}_2^* + \bar{E}_2 \times \bar{H}_1^*) d\bar{s}$$

The first two terms represent the individual energy of each wave while the last two terms couple the waves together. For a set of modes to be orthogonal the last terms must sum to zero which is a property of the operator L. In order to find a general procedure for determining the conditions for mode orthogonality[5,6] it is useful to consider the adjoint of Equation 4.7.

$$L^{\dagger} \cdot \bar{e}_{Tj} + \beta_j^2 \bar{e}_{Tj} = 0. \qquad L^{\dagger} \text{ is the adjoint of L and } \bar{e}_{Tj} = \bar{\varepsilon}_{Tj}^{\dagger} \tag{4.8}$$

Multiply Equation 4.8 by $\bar{\varepsilon}_{Ti}$ and Equation 4.7 by e_{Tj}. The difference of these

two new equations yield:

$$\bar{\varepsilon}_{Ti} \cdot L^{\dagger} \cdot \bar{e}_{Tj} - \bar{e}_{Tj} \cdot L \cdot \bar{\varepsilon}_{Ti} + (\beta_j^2 - \beta_i^2)\bar{e}_{Tj} \cdot \bar{\varepsilon}_{Ti} = 0$$

If $L^{\dagger} = L$ then L is said to self-adjoint and has the following property:

$$\int \bar{e}_{Tj} \cdot L \cdot \bar{\varepsilon}_{Ti} d\bar{r} = \int \bar{\varepsilon}_{Ti} \cdot L^{\dagger} \bar{e}_{Tj} d\bar{r}$$

This leads to the following orthogonality relation:

$$(\beta_j^2 - \beta_i^2) \int \bar{e}_{Tj} \cdot \bar{\varepsilon}_{Ti} d\bar{r} = 0 \qquad (4.9)$$

If we assume the $K_{\parallel}$ infinite approximation then

$$L = \nabla_T \times \nabla_T \times 1 - k_0^2 K_{\perp} = L^{\dagger}$$

In this approximation L is self adjoint and the adjoint wave solution is identical with the original solution. This means $\bar{\varepsilon}_{Ti} = \bar{e}_{Tj}$ and we have an orthogonal representation necessary for expansions of the following forms:

$$\bar{E}_T = \sum_i a_i \bar{\varepsilon}_{Ti} \qquad (4.10)$$

$$\bar{J}_s = \sum_i b_i \bar{\varepsilon}_{Ti} \qquad (4.11)$$

where

$$b_i = \frac{\int \bar{J}_s \cdot \bar{\varepsilon}_{Ti}^* dr_{\perp}}{\int \bar{\varepsilon}_{Ti} \cdot \bar{\varepsilon}_{Ti}^* dr_{\perp}} \qquad (4.12)$$

Substitution of Equations 4.10, 4.11 and 4.12 into Equation 4.6 and use of the homogeneous wave Equation 4.7 yields the following:

$$L \cdot \sum_i a_i \bar{\varepsilon}_{Ti} + \beta^2 \sum_i a_i \bar{\varepsilon}_{Ti} = -j\omega\mu_c \sum_i b_i \bar{\varepsilon}_{Ti}$$

$$-\sum_i a_i \beta_i^2 \bar{\varepsilon}_{Ti} + \sum_i a_i \beta^2 \bar{\varepsilon}_{Ti} = -j\omega\mu_c \sum_i b_i \bar{\varepsilon}_{Ti}$$

Solving for a_i and substituting in b_i results in:

$$a_i = \frac{-j\omega\mu_0 b_i}{(\beta^2 - \beta_i^2)} = \frac{-j\omega\mu_0}{(\beta^2 - \beta_i^2)} \frac{\int \bar{J}_s \bar{\varepsilon}_{Ti}^* dr_\perp}{\int \bar{\varepsilon}_{Ti} \cdot \bar{\varepsilon}_{Ti}^* dr_\perp}$$

$$\bar{E}_T = \sum_i \frac{j\omega\mu_0}{(\beta^2 - \beta_i^2)} \frac{\int \bar{J}_s \cdot \bar{\varepsilon}_{Ti} dr_\perp}{\int \bar{\varepsilon}_{Ti} \cdot \bar{\varepsilon}_{Ti} dr_\perp} \bar{\varepsilon}_{Ti}$$

Inverse Fourier transforming $\bar{E}_T$ and $\bar{J}_s$ expresses E_T as a function of z.

$$\bar{E}_T(z) = \frac{1}{2\pi} \int_{-\infty}^{\infty} d\beta \; \bar{E}_T e^{j\beta z}$$

$$E_T(z) = \sum_i \frac{j\omega\mu_0}{2\pi} \int_{\infty} \frac{e^{j\beta z}}{(\beta^2 - \beta_i^2)} \frac{\int \bar{J}_s \cdot \bar{\varepsilon}_{Ti}^* dr_\perp}{\int \bar{\varepsilon}_{Ti} \cdot \bar{\varepsilon}_{Ti}^* dr_\perp} \bar{\varepsilon}_{Ti} d\beta \qquad (4.13)$$

Replace β_i with $\beta_i - j\varepsilon$ and after the integraton in the complex plane has been performed let $\varepsilon \to 0$. The poles of the integrand in complex β-plane are shown in the following diagram.

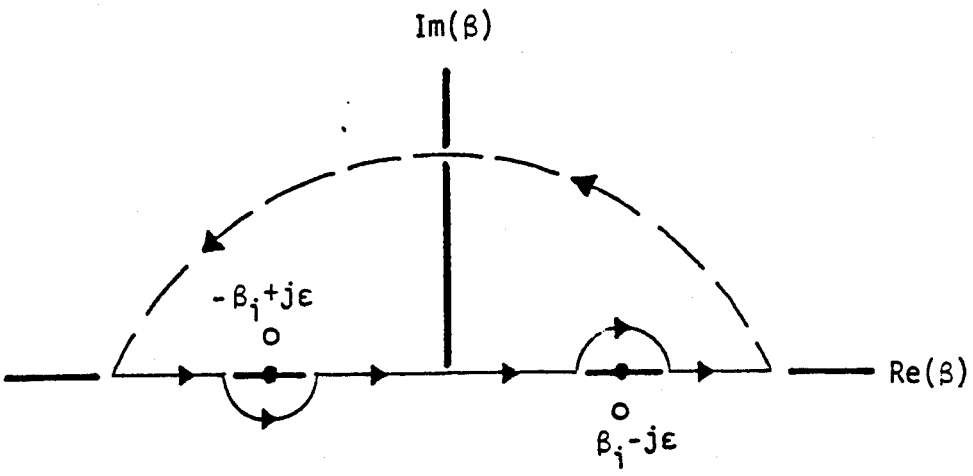

The path of integration leads along the real axis from $-\infty$ to $+\infty$ and a closed contour exists if we complete the path in the upper half plane. With the use of the residue at $\beta_i = \beta$ we have the solution to the integral and $\bar{E}_T$ becomes:

$$\bar{E}_T(z) = -\sum_i \frac{\omega\mu_0 \int \bar{J}_s \cdot \bar{\varepsilon}_{Ti}^* dr_\perp}{2\beta_i \int \bar{\varepsilon}_{Ti} \cdot \bar{\varepsilon}_{Ti}^* dr_\perp} \bar{\varepsilon}_{Ti} e^{-j\beta_i z} \tag{4.14}$$

Once the tangential fields are known we can calculate the loading impedance of a simple loop antenna for the following current distribution:

$$\bar{J}_s(r, \phi, z) = I(\phi)\ \delta(r - a)\delta(a)\hat{i}_\phi$$

Fourier analysis in the z directions yields:

$$\bar{J}_s = I(\phi)\delta(r - a)\hat{i}_\phi \tag{4.15}$$

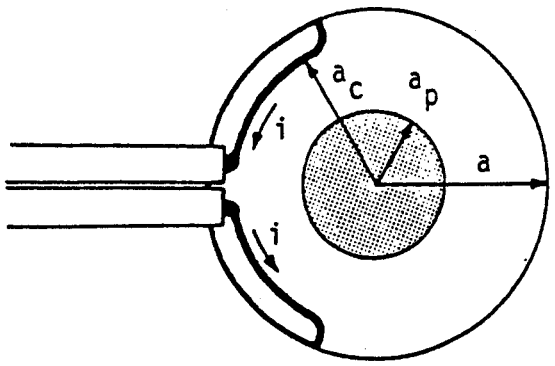

The integration of $\bar{E}_T \cdot \hat{\phi}$ along the antennae is simply the back EMF induced by the wave on the coil:

$$V = - a_c \int \bar{E}_T \cdot \hat{i}_\phi d\phi \tag{4.16}$$

The terminal impedance or antenna impedance is :

$$Z = V/I_t \tag{4.17}$$

Combining Equations 4.14, 4.15, 4.16 and 4.17 provides the antenna impedance once the tangential electric fields are found:

$$Z = a_c^2 \sum_i \frac{(\omega\mu_0/2\beta_i) \int d\phi[I(\phi)/I_t]\hat{i}_\phi \cdot \bar{\varepsilon}^*_{Ti} \int d\phi \hat{i}_\phi \cdot \bar{\varepsilon}^*_{Ti}}{\int dr_\perp \bar{\varepsilon}_{Ti} \cdot \bar{\varepsilon}^*_{Ti}} \tag{4.18}$$

The Re(z) represents the radiation resistance while the Im(z) results from the reactive wave field. In addition to the wave contribution to the antenna

impedance there is also an additional Re(z) due to ohmic resistive losses and $I_m(z)$ due to a nonpropagating near field. These effects will be discussed later on.

4.2 Toroidal Cavities

So far we have considered a waveguide system which is linear and infinite in extent. The problem of wave propagation in a toroidal shaped device is more complicated but the methods are similar. In this geometry a wave can travel a number of times around the torus and therefore produce toroidal eigenmodes. This problem can be reduced back to a linear infinite system by using the following "image" equivalent representation.

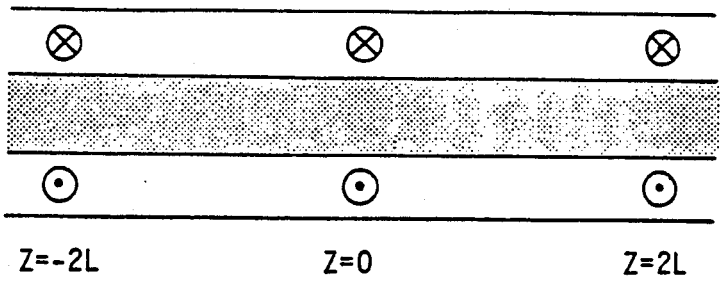

Now the source term is composed of an infinite number of sources located at $z = 2nL$ $(n = 0, \pm 1, \pm 2, \ldots)$

$$\bar{J}_s(r,\phi,z) = I(\phi)\delta(r - a)\sum_{n=-\infty}^{\infty}\delta(z - 2nL)\,\hat{i}_\phi \qquad (4.19)$$

Fourier transforming in the z direction yields

$$J_s = I(\phi)\delta(r - a)\sum_{n=-\infty}^{\infty}e^{-j2n\beta L}\,\hat{i}_\phi$$

Using the similar integration methods as before, Equation 4.18 can be re-written for the new geometry as follows:

$$Z = a_c^2 \sum_i \frac{(\omega\mu_0/2) \int d\phi [I(\phi)/I_t] \hat{i}_\phi \cdot \bar{\varepsilon}_{Ti}^* \int d\phi \hat{i}_\phi \cdot \bar{\varepsilon}_{Ti}}{\int dr_\perp \bar{\varepsilon}_{Ti} \cdot \bar{\varepsilon}_{Ti}^*} \left[\frac{\cos\beta_i L}{\beta_i \sin\beta_i L} \right] \qquad (4.20)$$

From Equation 3.21 and for $E_z = 0$, the tangential electric fields are:

$$\bar{\varepsilon}_T = \hat{r}\left(- \frac{jmS}{r} J_m + \rho R J_m' \right) \hat{H}_1 e^{jm\phi} + \hat{\phi} \left(\frac{jmR}{r} J_m + \rho S J_m' \right) \hat{H}_1 e^{jm\phi}$$

Note:

$$\int \left[x(J_m')^2 + \frac{m^2}{x^2} J_m^2 \right] dx = \frac{x^2}{2} \left[J_m^2 + J_{m+1}^2 - 2\frac{(m+1)}{x} J_{m+1} J_m \right] + m J_m^2$$

The antenna impedance for arbitrary poloidal mode number can be written as:

$$Z_i = (2\pi\omega\mu_0) \frac{\left[mgJ_m(a_c\rho) + a_c\rho J_m'(a_c\rho) \right]^2 f_\phi X_{\beta i}}{(a\rho)^2(1+g^2) \left[J_m^2 + J_{m+1}^2 - [2(m+1)/a\rho] J_m J_{m+1} \right] + 2(1+g)^2 m J_m^2}$$

where $f_\phi = \frac{1}{4\pi^2} \int_{\phi_c} e^{jm\phi} d\phi \int_{\phi_c} e^{-jm\phi} \frac{I(\phi)}{I_t} d\phi$

$$X_{\beta i} = \frac{1}{\beta_i} \frac{\cos\beta_i L}{\sin\beta_i L}$$

$$g = - \frac{R}{js}$$

For m = 0 and the boundary condition $J_0'(a\rho) = 0$ the antenna impedance becomes:

$$Z_i = \frac{(2\pi\omega\mu_0)[a_c J_0'(a_c\rho)/aJ_0(a\rho)]^2 X_{Bi}}{1 - k_0^2 K_x^2/(k_0^2 K_\perp - \beta^2)^2}$$

Note that for m = 0, $J_1(a\rho) = 0$ and $A_\phi = 1$. Important aspects of the impedance equation will be discussed in conjunction with experimental results in Chapter 7.

5. DAMPING MECHANISMS

There are several different mechanisms through which RF energy can heat a fusion-grade plasma. Without careful selections of certain key parameters, RF absorption may occur at the plasma surface or at other undesirable locations. It is also necessary to understand how the power couples to the electrons, ions, minority-species ions and impurity ions in order to evaluate the efficiency of a particular heating scheme. In addition to this it is desirable to know how the energy distribution function is modified by particle-wave interaction. The waves that are excited can be absorbed by collisional and collisionfree processes by the plasma. The important collisionfree processes are cyclotron damping for the ions (fundamental and second harmonic), and for the electrons transit-time damping and Landau damping.

5.1 Ion Cyclotron Damping

Collisionless ion cyclotron damping can occur when some multiple of the particle's cyclotron frequency equals the doppler shifted wave frequency $\omega - k_{\parallel}V_{\parallel} = n\omega_{ci}$. For typical tokamak parameters this approximately occurs on a surface where $n\omega_{ci}(R) = \omega$. Each time an ion traverses this surface as shown in Figure 5.1, it acquires an incremental increase in perpendicular energy provided the particle has sufficient time to acquire the proper phase with respect to the electric field of the wave.

Particle absorption via collisionless processes is calculated from $\bar{J}$ and $\bar{E}$ by:

$$P_{abs} = \langle Re(\bar{J}\cdot\bar{E})\rangle$$

This expression is dependent on the anti-Hermetian part of the dielectric tensor and is therefore zero for a cold plasma. Employing the warm plasma dispersion relation and suitable approximations Stix[7] has shown that the

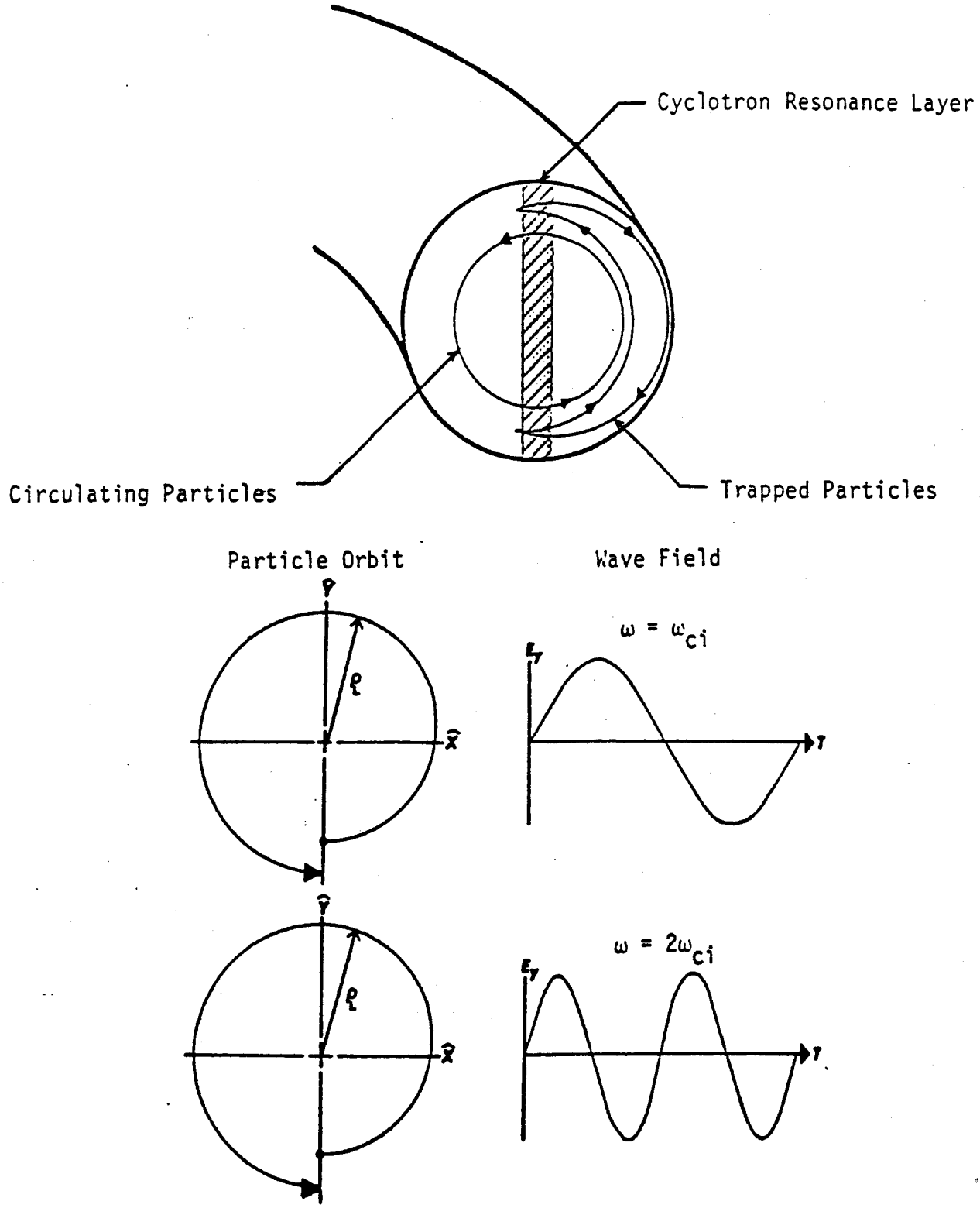

Figure 5.1. An ion is continuously accelerated by wave field when $\omega = \omega_{ci}$. However for $\omega = 2\,\omega_{ci}$ there must be a gradient in the electric field or the toroidal magnetic field in order for ions to gain net energy.

average power absorbed per unit volume by the ions is:

$$P/\text{unit volume} = \frac{\varepsilon_o \sqrt{\pi}\omega_{ci}^2}{k_{\parallel} V_t}\left(\frac{k_\perp^2 V_t^2}{2\omega_{ci}^2}\right)^{n-1} \exp\left[-\left(\frac{\omega - n\omega_{ci}}{k_{\parallel} V_t}\right)^2\right] |E_L|^2$$

where n = ion cyclotron number and

$$V_T = \left(\frac{2kT_i}{m_i}\right)^{1/2}$$

Since ω_{ci} is proportional to 1/R, the exponential function is appreciable only over small distances on the order of:

$$\Delta x = \frac{2k_{\parallel} V_t R}{n\omega_{ci}}$$

Assuming that $|E_L|^2$, ω_{pi}, $k_{\parallel}$, and V_T are constant over the resonant zone Δx, then the following integral represents the total average power absorbed:

$$P_T = \Delta x \; 2\pi R \int_{-a}^{a} \left(\frac{P}{\text{unit volume}}\right) dr$$

where "R" is the major radius and "a" the minor radius.

For concepts dealt with in this thesis, the dimensionless figure of merit Q is or more use than the specific formula for power asorption. For second harmonic resonant heating Paoloni [8] has derived the following equation for the value of Q:

$$Q_{2\omega_c} = \frac{2\sqrt{\pi}}{\lambda_i}\left(\frac{c}{V_p}\right)^2\left(\frac{\omega_{ci}}{\omega_{pi}}\right)^2\left(\frac{a}{R}\right)\left(\frac{k_\perp}{k_\parallel}\right)^2 \frac{\left[\frac{1}{2k_\perp^2}\left(\frac{k_A^2}{(1+\Omega)^2} + k_\parallel^2\right)\left(\frac{1}{k_\parallel A} + 1\right) + 1\right]^2}{\left[\frac{1}{k_\parallel A} - 1\right]} \qquad (5.1)$$

where: $\lambda_i = 1/2\,(k_\perp r_L)^2 = \frac{k_\perp^2 V_T^2}{2\omega_{ci}^2}$

$$V_p = \frac{\omega}{k_\parallel}$$

$$\frac{1}{k_\parallel A} = \frac{(k_\parallel^2 + k_\perp^2)\Omega}{k_A^2 - k_\parallel^2}$$

This procedure is also valid for plasmas containing a minority ion species. In this case the properties of the fast wave (wave energy and E_L) are approximately determined by the majority component and the minority only effects the power absorption. When the minority fundamental resonance layer is in the center of the plasma, Paoloni [8] expresses the Q as:

$$Q_{MIN} = \frac{\sqrt{\pi}}{2}\left(\frac{c}{V_p}\right)^2\left(\frac{\omega_{ci}}{\omega_{pi}}\right)^2_{MIN}\left(\frac{a}{R}\right)\left(\frac{k_\perp}{k_\parallel}\right)^2 \frac{\left[\frac{1}{2k_\perp^2}\left(\frac{k_A^2}{(1+\Omega)^2} \quad k_\parallel^2\right)\left(\frac{1}{k_\parallel A} + 1\right)^2 + 1\right]}{\left[\frac{1}{k_\parallel A} - 1\right]^2} \qquad (5.2)$$

where ω_{pi} and ω_{ci} are evaluated for the minority component in

$$\left(\frac{\omega_{pi}}{\omega_{pi}}\right)_{MIN}$$

It is also important to know whether the power is deposited in the bulk or the tail of the ion distribution. For typical tokamak parameters, coulomb collisions during poloidal circumnavigation times will cause random phase delays among particles leaving the resonant zone. This implies that each transit through the resonant zone is independent of past history with respect to phase. Once this is justified it is valid to derive a Fokker-Planck equation which will govern the quasilinear evolution of the ion velocity distribution. This is essential since most quasilinear calculations demand randomly-phased modes to justify the concept of true particle diffusion resulting from a number of incoherent velocity displacements. Although this thesis deals primarily with the concepts of absorption mechanisms, it is important to grasp this major point in the evolution of the distribution function.

5.2 Ion-Ion Hybrid Resonance Damping

Energy of the fast magnetosonic wave can also be absorbed via the ion-ion hybrid resonance provided a minority ion species is present. The dispersion relationship for the $K_{\parallel} \to \infty$ approximation can be factorized in the following form:

$$n_{\perp}^2(K_{\perp} - n_{\parallel}^2) = (n_{\parallel}^2 - R)(n_{\parallel}^2 - L)$$

The ion-ion hybrid resonance will occur at the surface where $K_{\perp} - n_{\parallel}^2 = 0$ which implies $n_{\perp} \to \infty$. In reality $n_{\perp} \neq \infty$ and a sequence of mode conversions will result. This class of problems has a closely spaced resonance and cut-off layer which is approximately described by Budden's equation. Perkins[9] and Swanson[10] have obtained absorption, reflection and tunneling coefficients for this process. When deuterium is the majority component and hydrogen is the

minority component, the hybrid layer is located on the high field side of the fundamental layer. On the major axis, the approximate position is given by:

$$R_{ION\text{-}ION} = R\left[1 + \frac{A_2N_2}{A_1N_1}\right]^{1/2}\left[1+\frac{Z_2^2A_1N_2}{Z_1^2A_2N_2}\right]^{-1/2} \qquad (5.3)$$

R is the major radius, A_i, Z_i, N_i for i = 1,2 are respectively the mass number, the charge number, and the density (i = 2 is the minority component). This layer is sensitive to the relative concentration of species and, for 95% deuterium and 5% hydrogen, it lies about 1.8 cm from the cyclotron resonance.

Since $k_{\parallel}$ for the fast wave is very large near the resonance layer, the mode-converted wave must have a comparable $k_{\parallel}$ for good coupling efficiency. The converted wave is believed to be a class of Ion Bernstein waves. Because this wave propagates away from the narrow hybrid layer and it has a relatively large $k_{\parallel}$, electron Landau damping is important. For small proton concentration the hybrid layer lies close enough to the cyclotron layer implying that the Ion Bernstein wave can also undergo cyclotron damping before the wave is completely Landau damped. This means that both ion and electron heating could occur for this process. Perkins[9] computes the damping for this process as:

$$Im(k_{\parallel})_{II} = \frac{\pi}{4R^2k_{\parallel}}\left(\frac{R\omega_{pD}}{c}\right)^2\frac{R}{a}\left(\frac{2Z_2}{A_2}n_p\right)\frac{(\omega_{cD} - \omega_{cH})^2}{(\omega_{cD}^2 - \omega_{cH}^2)} \qquad (5.4)$$

where n_p is the proton concentration.

Since it is possible for the ion-ion hybrid layer to lie close to the cyclotron layer, their effects cannot always be separated in a practical experiment. It should be noted that the presence of the ion-ion hybrid resonance also effects the absorption at the ion cyclotron layer. The hybrid layer alters the wave field polarization in the vicinity of the cyclotron layer by increasing the left-hand component of the field. This enhances the cyclotron absorption,[11] but this effect becomes insignificant for densities above 0.35×10^{14} cm^{-3}.

5.3 Electron Landau and Transit-Time Damping

Electrons can absorb a considerable amount of energy from the wave when the phase velocity is near the electron thermal speed. Particles for which $\omega - k_{\parallel} V_e = 0$ undergo Landau damping and transit-time magnetic pumping. In transit-time damping the wave acts on the particle through the force $-\mu\nabla B$ and for Landau damping the particle force is $q\bar{E}$. These mechanisms are related through the phase of $\bar{B}$ and $\bar{E}$, and therefore not independent. Stix[7] has shown that the average power absorbed per unit volume by the electrons to be:

$$\text{P/unit volume} = \sqrt{\pi}\varepsilon_0 \frac{V_{Te}}{k_{\parallel}} \omega^2 \left(\frac{\omega_{pe}}{\omega_{ce}}\right)^2 e^{-(V_p/V_{Te})^2} |B_z|^2$$

Integrating the equation over the plasma volume and using the total wave energy Paoloni[8] has determined the Q to be:

$$Q_E = \frac{1}{4\sqrt{\pi}} \left(\frac{c}{V_p}\right)^2 \left(\frac{V_p}{V_{Te}}\right) \left(\frac{\omega_{ce}}{\omega_{pe}}\right)^2 e^{(V_p/V_{Te})^2} \left[\frac{1}{2k_{\perp}^2}\left(\frac{k_A^2}{(1+\Omega)^2} + k_{\parallel}^2\right)\left(\frac{1}{k_{\parallel}A} + 1\right)^2 + 1\right] \quad (5.5)$$

5.4 Ohmic Collisional Damping

In low temperature plasmas ohmic collisions can absorb power from the wave. The average power lost per unit volume for collisions is:

$$\text{P/unit volume} = \frac{1}{2} R_e(\bar{J}\cdot\bar{E}) = \frac{1}{2} R_e[(\bar{\bar{\sigma}}\cdot\bar{E})\cdot\bar{E}]$$

For the fast wave, Paoloni[8] has found the Q to be:

$$Q_{col} = \frac{\omega\mu_0}{\eta_{\parallel}} \frac{1}{k_{\parallel}^2}\left[\frac{1}{2k_{\perp}^2}\left(\frac{k_A^2}{(1+\Omega)^2} + k_{\parallel}^2\right)\left(\frac{1}{k_{\parallel}A} + 1\right)^2 + 1\right] \qquad (5.6)$$

where $\eta_{\parallel} = 0.5 \times 10^{-4}\ \ln\Lambda/T_e^{3/2}$ (T_e in eV). When the temperature is above 10 eV, collisional effects are unimportant compared to other damping mechanisms. Basically, the high conductivity of the plasma forces E_z to be extremely small, preventing energy transfer through collisions. Despite the low temperatures at the plasma edge, collisional effects still remain insignificant because for typical density profiles E_z is still small in the edge region.

5.5 Wall Loading

Since we are dealing with guided waves, some power will be lost in the finite conductivity of the vacuum chamber walls. Jackson[12] uses a simple approximation method in order to solve this problem. Using the fields obtained from the ideal boundary conditions, one finds the fields within the conductor by using Maxwell's equations. Ignoring the displacement current, the electric field in the conductor is:

$$\bar{E}_c = \frac{1}{\mu_0\sigma}(\nabla \times \bar{B})$$

This small tangential component of $\bar{E}$ in association with the tangential component of $\bar{H}$ implies that there is a net power flow into the conductor:

$$P/\text{unit area} = \frac{1}{2} \text{Re} \left(\bar{E} \times \bar{H}^* \cdot \hat{r}\right)_{r=a}$$

Paoloni[8] calculates the value of Q for wall loading as:

$$Q_w = \frac{1}{2}\left(\frac{a}{\delta_s}\right)\left(\frac{\ell_T}{\ell_s}\right)\left[\frac{1}{2k_\perp^2}\left(\frac{k_A^2}{(1+\Omega)^2} + k_\parallel^2\right)\left(\frac{1}{k_\parallel A} + 1\right)^2 + 1\right] e^{2k_\parallel \delta} \qquad (5.7)$$

where $\delta_s = (\pi f \mu_0 \sigma)^{-1/2}$

δ = distance between plasma and wall

$\ell_T = 2\pi R$

ℓ_s = surface length of the torus

For the Alcator A experiment $\ell_T/\ell_s \approx 0.5$. This geometrical factor is based upon wall corrigation and port size.

5.6 Fundamental Single Species Ion Cyclotron Damping

It turns out that heating ions via the fundamental cyclotron resonance in a single species plasma is a poor choice. Despite the strong coupling between the electric field and the ions, the left-hand component of the electric field is quite small because it is shorted out by the large number of resonant ions. The overall absorption is weak and Perkins[9] estimates the Q to be:

$$Q_{\omega_c} = \frac{a}{R}\left(\frac{\omega_p^2}{k_\parallel^2 c^2}\right)\frac{1}{B_i} \quad \text{where} \quad B_i = \frac{nkT}{B^2/2\mu_0} \qquad (5.8)$$

In competition with fundamental cyclotron absorption layer is the ion-cyclotron mode conversion layer near the surface of the plasma. As stated previously, the dispersion relation can be expressed as:

$$n_\perp^2(k_\perp - n_\parallel^2) = (n_\parallel^2 - R)(n_\parallel^2 - L)$$

Mode-conversion will occur at the surface where $k_\perp - n_\parallel^2 = 0$. For $n = 1.5 \times 10^{14}$ and typical experimental parameters at 90 MHz, this surface is about 1 cm from the plasma edge. The conversion occurs on the high field side of the fundamental layer. Perkins [9] develops a simple slab mode and dispersion relationship for estimating the effects of ion-cyclotron mode coversion. The estimated Q for the process is:

$$Q_{IC} = \frac{1}{2\pi}\frac{R}{a}\left(\frac{\omega_p^2}{k_\parallel^2 c^2}\right)^2 \qquad (5.9)$$

For Alcator A parameters the power absorbed by this process is larger than fundamental absorbtion. This means the wave can easily tunnel through the center of the machine and be absorbed near the plasma edge when launched from the low field side. It should also be noted that ion-cyclotron mode conversion doesn't occur for second harmonic heating experiments in a single species plasma since $k_\perp - n_\parallel^2 \neq 0$.

6. EXPERIMENTAL APPARATUS

The equipment used in this experiment falls into two distinct groups. The first group deals with wave generation and consists of the transmitter chain, matching network and the antenna structure. The second group uses RF diagnostics to analyze wave propagation and covers the measurement of radiation resistance, probe signals and $k_{\parallel}$.

6.1 Antenna System

Designing an antenna structure for Alcator A is a very difficult task because of the compact nature of the machine. The vacuum ports in Alcator A are very small as a result of the Bitter magnet design, large compressional forces on the flange, and the need for small ripple in the toroidal magnetic field. The largest single hole is 1.25" by 3.4" which introduces stringent mechanical constraints on the antenna design. It was necessary to develop an antenna which could be slid in horizontally and then rotated vertically. With the aid of various insertion jigs, an antenna which subtended a poloidal angle of 130° could be installed on the low-field side of the torus. In the course of this experiment, three different antennae were developed. All three antennae[13] were center fed one-half turn magnetic loops as shown in Figure 6.1. The first antenna (A_1) was machined out of a solid block of 304 stainless steel. Structural integrity was a main issue in this design because of the proximity of the plasma and the antenna. The sides of this steel block were slotted, and narrow clips were E-beam welded across the front face, which resulted in a simple faraday shield. The purpose of the faraday shield was to short out the E_z component of the near field and prevent coupling to undesirable parasitic modes. The faraday shield also reduced the plasma density near the center conductor. At each

end of all three antennae, small probes were used to monitor RF antenna currents for radiation resistance measurements. These probes were inserted through vertical access ports after the antenna was installed.

The A_1 antenna was finally abandoned because of insufficient radiation resistance which resulted from a poorly designed faraday shield. The A_2 antenna had about three times more radiation resistance than the A_1 configuration, and therefore more power could be coupled to the plasma. The antenna had a loop area two and a half times larger than the previous design, which increased the radiation resistance significantly. The loop area was increased by reducing the plasma radius from 10 cm to 9 cm enabling the distance between the wall and the center conductor to be increased. It also had a wider center conductor which lowered the antenna terminal impedance and helped prevent arcing. In favor of higher radiation resistance, it was decided that a faraday shield would not be incorporated in the deisgn. However, in order to reduce the plasma density in the vicinity of the antenna, two slotted limits were positioned adjacent to the antenna. Figure 6.2 shows the orientation of the limits with respect to the antenna. Although this antenna coupled more power to the plasma, there was no strong evidence of plasma heating, alluding to the fact that parasitics were indeed a problem. The third and final antenna tested was A_4. Basically, we removed the faraday clips on A_1 and moved the center conductor three times farther out. New curved faraday clips were welded on and the side limiters from the A_2 configuration were also installed. With these modifications the A_4 antenna had twice the radiation resistance of the A_1 antenna. See Figure 6.3 for a picture of the design. Although it is not visible in any of the photographs, the center conductors and the inside surfaces of the black planes of all three antennae were silver-plated by standard electroplating techniques in order to improve electrical conductivity.

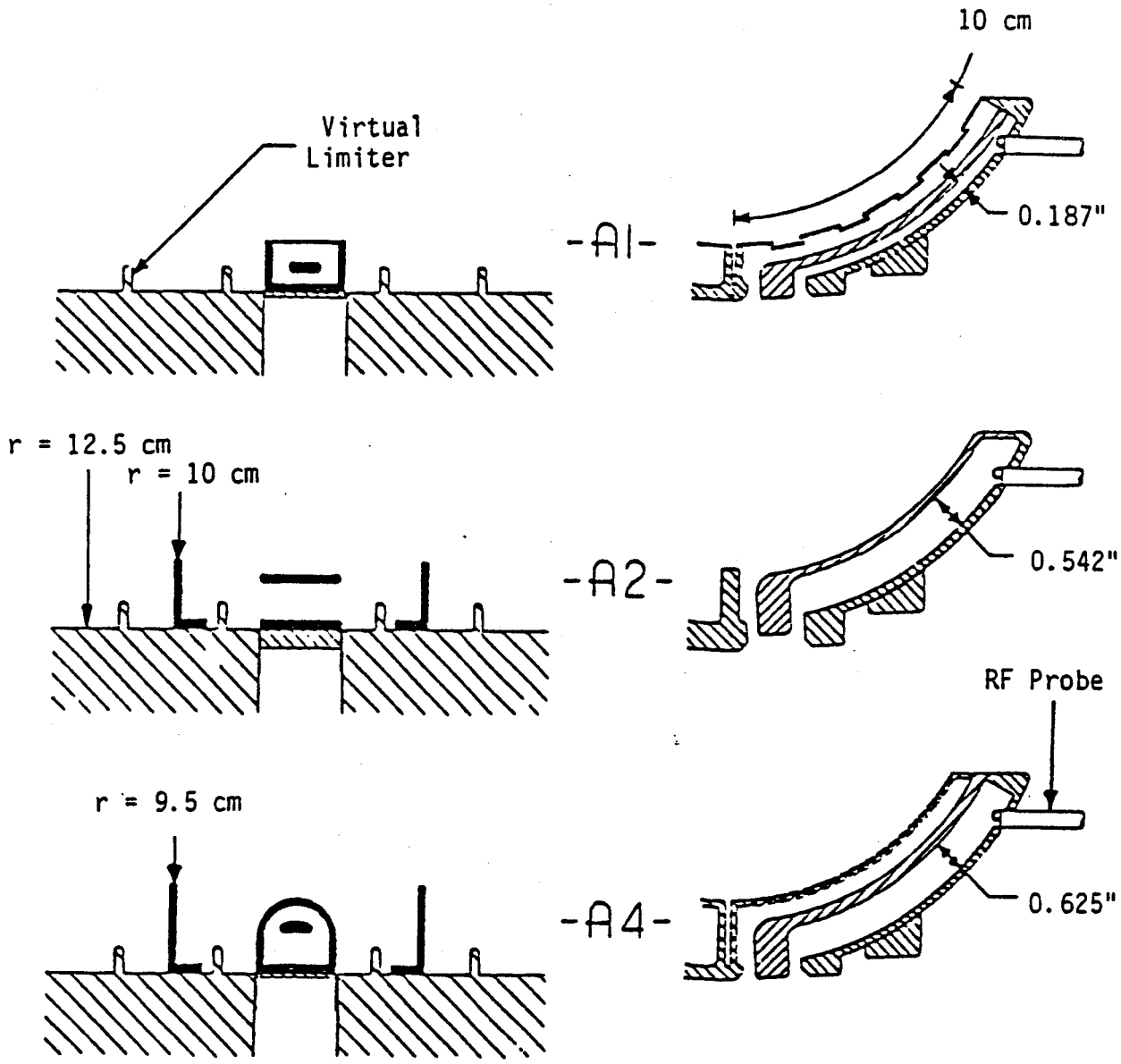

Figure 6.1. Front and side sectional views of the three antenna configurations tested in Alcator A. Only A_1 and A_4 were equipped with a faraday shield. Note RF probe used to monitor antenna current for radiation resistance measurement.

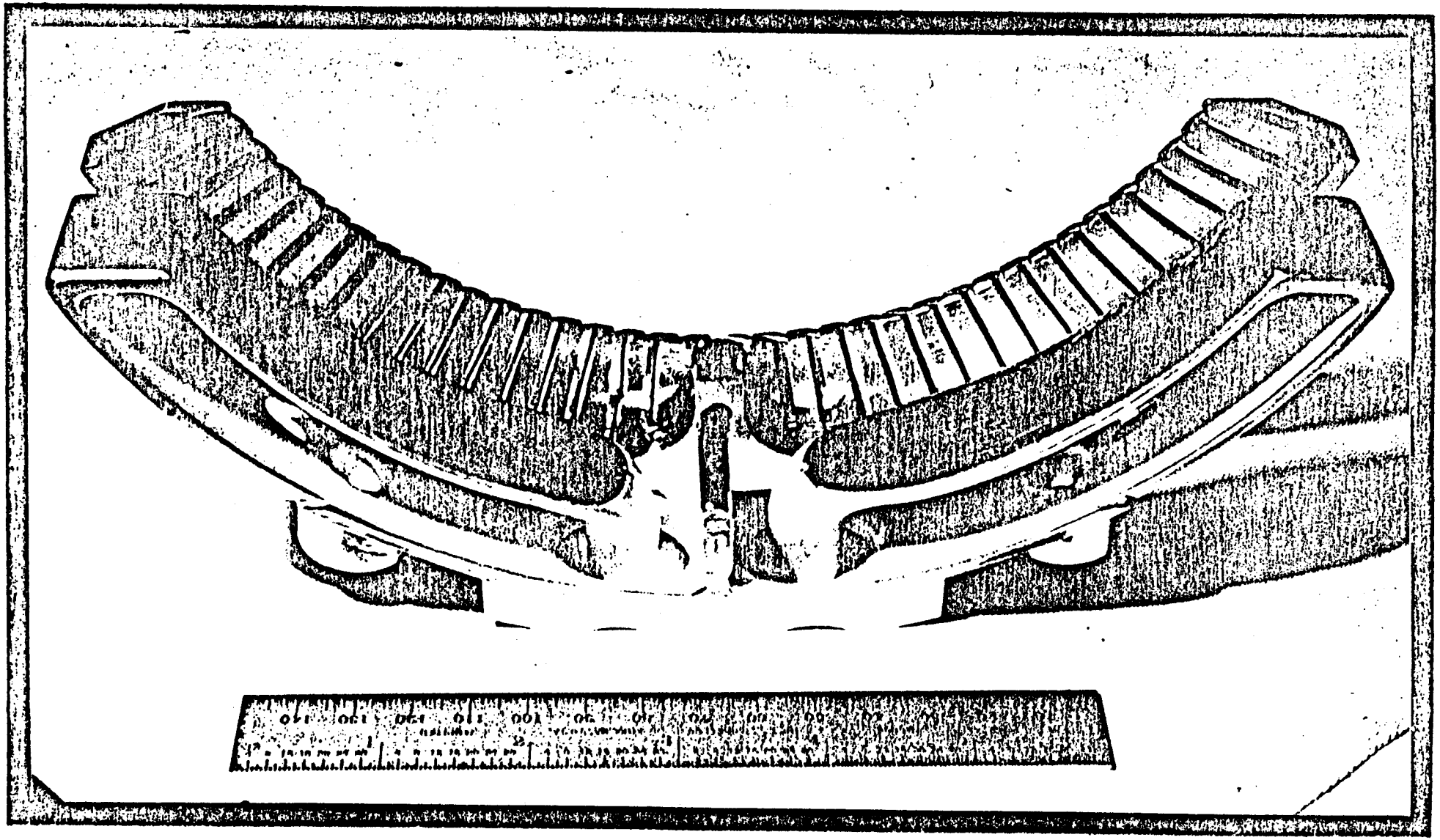

Figure 6.2. View of the A_2 antenna configuration with one of its two side limiters in position.

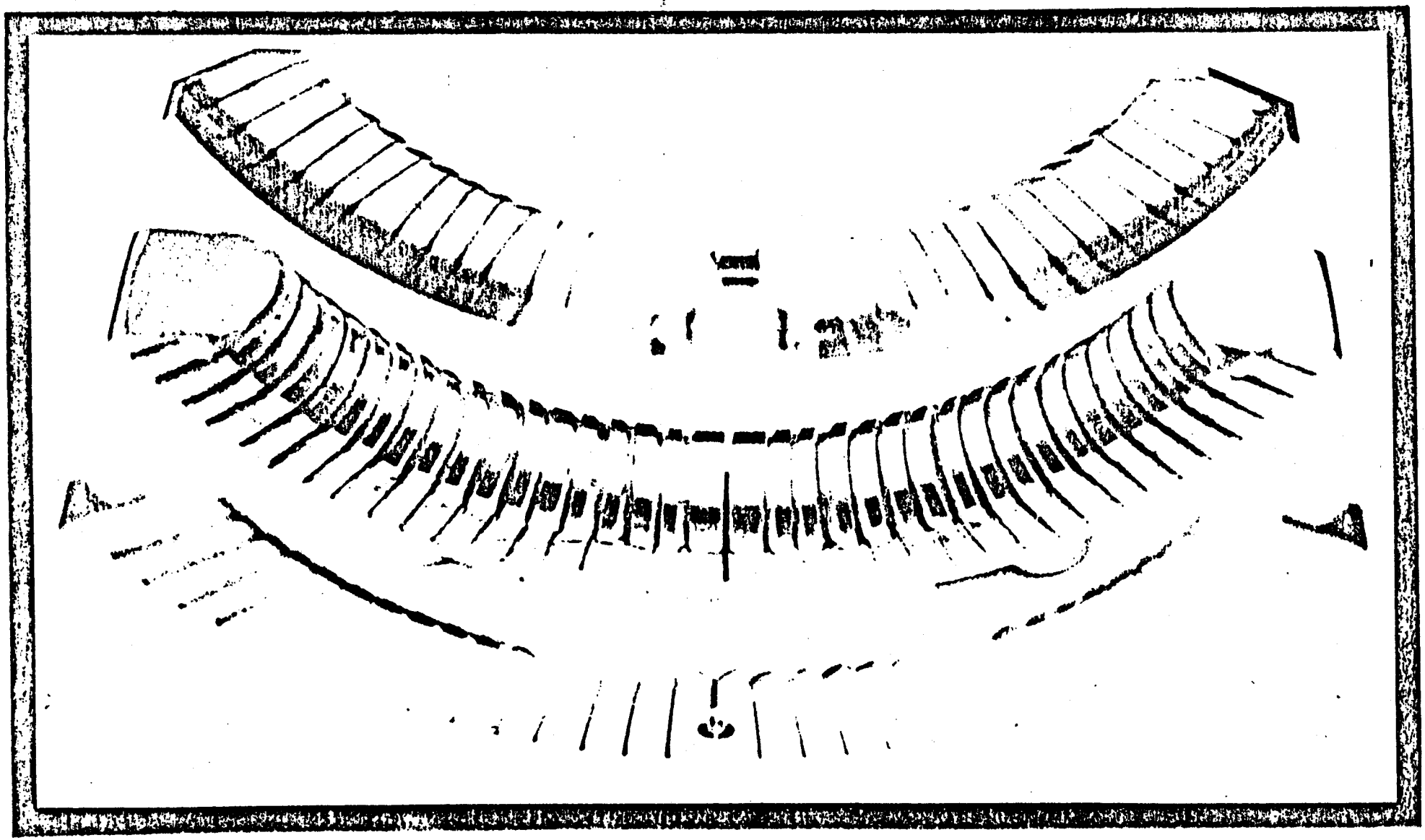

Figure 6.3. View of the A_4 antenna configuration with both side limiters in position.

6.2 Matching Network

In order to ensure low VSWR on the transmission line between the transmitter and antenna, a matching network was constructed. The matching system was designed for a 1 MW experiment and as a result it is quite large. Figure 6.4 shows the 9" coaxial transmission line which couples the matching cavity to the transmitter chain. The cavity length and tap angle of the 9" input coax are tunable in order to match the antenna impedance to the 50Ω transmission line. At 200 MHz the cavity is tuned to one and one half wavelengths and for 90 MHZ operation, set to three-quarter wavelengths with the lower shorting plate removed.

The resonator is connected to the antenna by means of two 1" vacuum coaxial lines. Due to the poor conductance between the Alcator A vacuum vessel and the coaxial lines a 30 liter/sec high-Q ion pump was installed which maintained low pressure in these lines. Figure 6.5 shows a detailed view of the antenna and coaxial feeders. All these components are connected directly to the tokamak and voltage isolation from the resonator to the coax center conductors is provided inherently by the magnetic coupling loop. On the other hand the outer conductor of the coax feeders are connected to the resonator through a teflon by-pass capacitor. In this way there exist complete DC isolation between the tokamak and all RF components except for the coaxial feeder assembly. The antenna and 1" coax feeders are made from 304 stainless steel that was silver plated 0.001" to reduce resistive losses. All the RF current flows in the silver plating since at 200 MHz the skin depth is 2×10^{-4} inches. Most of the system loss occurs in the two coaxial feeders, and the resistance is calculated from the following equation:

$$R = \frac{\ell}{2\pi r \sigma \delta} \qquad (6.1)$$

where, for silver, $\sigma = 6.1 \times 10^{7}$ mho/meter, $\ell = 1$ meter/line, and $\delta = (2/\omega\mu_0\sigma)^{\frac{1}{2}}$. The theoretical resistance of both coaxial feeders at 200 MHz is R = .3Ω, while the measured resistance for the system was R = 0.5Ω.

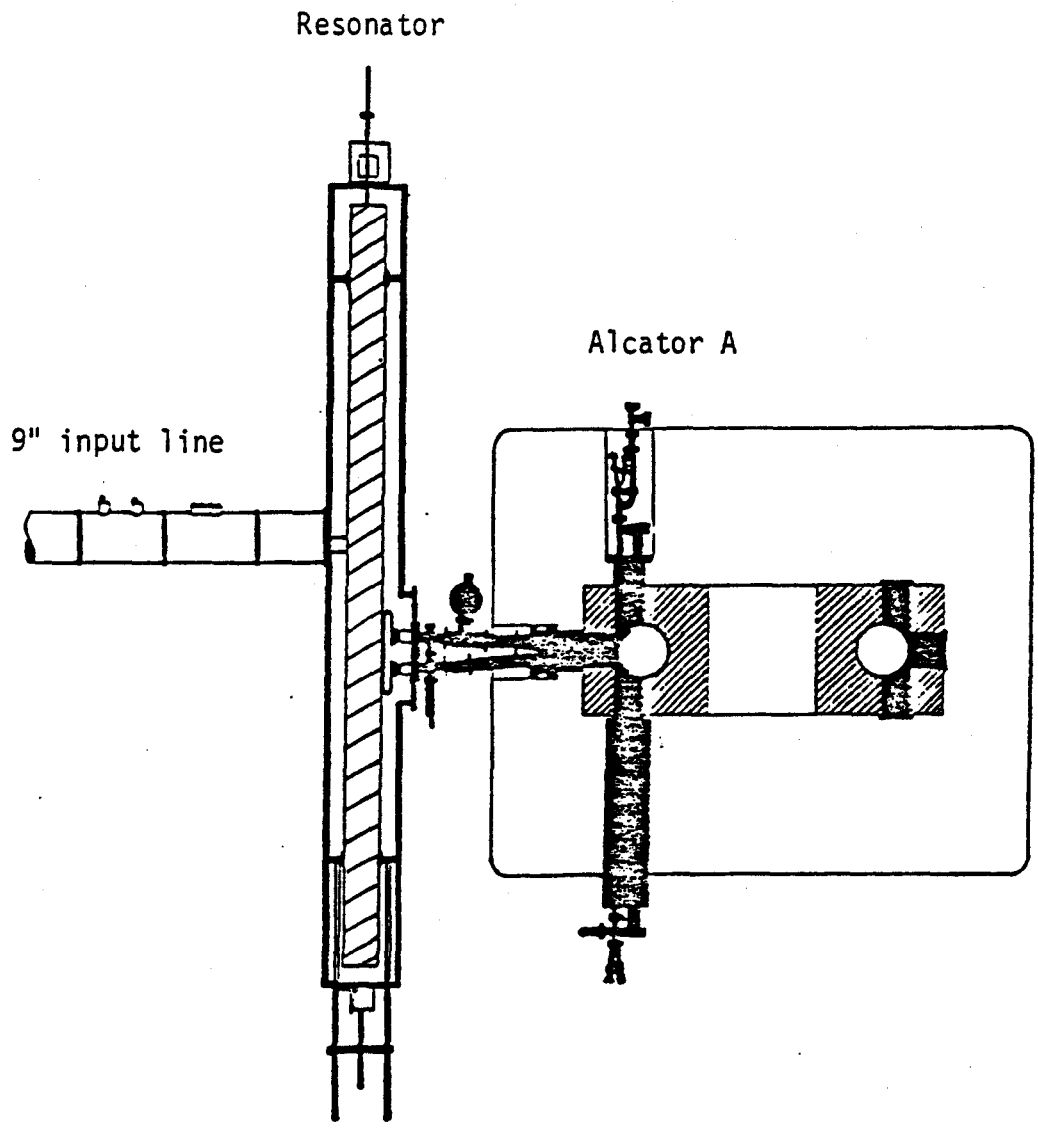

Figure 6.4. Location of the coaxial resonator with respect to Alcator A. This system was used to match the antenna impednace to 50Ω transmission line. In order to tune the system a servo mechanism was used to adjust the position of the upper plate, lower plate and tap angle.

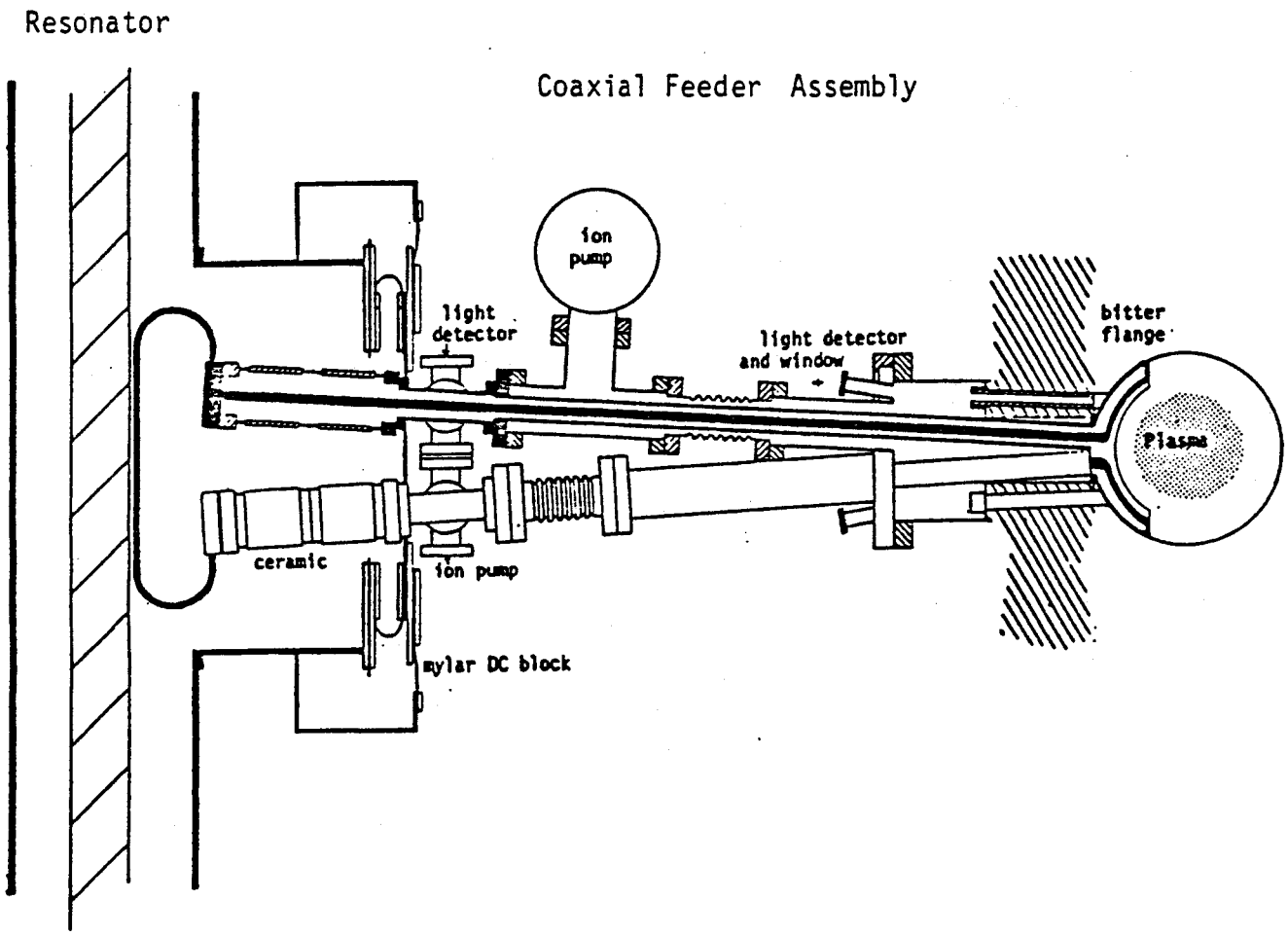

Figure 6.5. Detailed view of the coaxial vacuum lines used to drive the antenna. Ion pumps were used to maintain high vacuum in the lines as a result of the poor conductance to the main vacuum chamber. Note the ceramic RF vacuum breaks located inside the resonator.

6.3 Transmitter System

A 1,000-watt broadband amplifier was used for all measurements of antenna resistance and $k_{\parallel}$. The versatility of this amplifier enabled us to change the frequency from 90 MHz to 200 MHz without tuning the transmitter. The transmitter is based upon a distributed amplifier configuration and has 10 Eimac tubes which are separated by an equal number of electrical degrees. The grid line and plate line are equivalent to a terminated lumped-element transmission line where the electrode capacitance and external inductors are the key elements. When an RF signal is applied to the grid input, a wave travels along the grid line, and the various tubes are gated into sequential conduction. For any tube gated into conduction, one half of the plate current travels toward the load end of the plate line while the other half travels toward a termination resistor. Because of the phase tracking in the plate and grid lines, the phasor sum of the individual tube currents add and the signal is amplified by a factor of 0.5 N (N being the total number of tubes). The broadband nature results from the fact that the plate and grid circuits behave like terminated transmission lines and therefore the impedance is independent of frequency. This configuration also has the advantage that the power output is constant even with poorly matched loads.

For the high-power heating experiments on Alcator A, the 1 KW amplifier was used as an excitor for a 100 KW pulsed Class C amplifier. The Class C amplifier used an RCA 2041 tetrode in a half-wavelength transmission line cavity. This tetrode in turn drives a grid pulsed RCA 6550 triode and can be tuned from 170 MHz to 220 MHz. The 6950 is a double-ended coaxial

super-power, shielded-grid beam triode mounted in a 30 Ω coaxial cavity and delivers 1 MW. Through suitable RF switch gear it was easy to switch from 1 KW to 1 MW.

6.4 RF Probes

In order to study key features associated with the propagation of the fast compressional Alfven wave, a number of RF probes were positioned near the plasma edge. Specifically the probes were located near the antenna, one-quarter and half way around the torus. Although these probes were located in the evanescent fields associated with the vacuum layer, a great deal of information can still be obtained. The typical probe consisted of a one-turn magnetic loop connected directly to a coax cable. All RF diagnostics used double-shielded RG55 coax in order to minimize pickup and, for typical lengths of 50 ft., the losses were 3.5 dB at 200 MHz. A Tektronix 7834 storage mainframe was used for acquisition of the probe data. The 7834 oscilloscope has a stored writing speed of 2,500 cm/μs, enabling one to display single-trace rise times of 1.4ns. The pre-amp used with the mainframe was a 7A24 which is a high-performance, wide-band, dual-trace amplifier from DC to 400 MHz with 5 MV sensitivity. Both inputs are 50Ω terminated with a VSWR of 1.25:1. With the 7834 and two 7A24 plug-ins, four RF traces could be stored at a time.

6.5 $K_{\parallel}$ Array

An important parameter in this experiment is the value of $k_{\parallel}$ since magnetude of wave damping and even the type of damping are strongly affected by it. In order to measure $k_{\parallel}$ we developed an eleven-probe array which monitors the phase and amplitude of the wave in the toroidal direction.

The length of the array which was determined by insertion criteria was 17 cm. See Figures 6.6 and 6.7 for physical details of the $k_{\parallel}$ array. The main body of the array is a hollow block of stainless steel with eleven ceramic feedthroughs. The center conductors of the feedthroughs were bent to form one-turn RF loops. The other ends of the feedthroughs located inside the body of the array were soldered to a piece of 1/16 hardline coax cable which then runs up the insertion boom. The inside of the array and boom are at atmospheric pressure while the outside is at machine vacuum. There is also a bellows between the insertion boom and the array block which allows the array to be folded in order to fit through the keyhole in the flange during installation. At the end of the insertion boom the coax is connected to a DC isolation block and after a 60-foot run of RG55, the signal is processed by quadrature phase detection or heterodyne detection.

In the heterodyne phase detection configuration, eleven ZAD-1 Mini-Circuit mixers were used to beat the RF probe signal with a stable local oscillator. The output of the detector consisted of a 100 KHz signal whose amplitude and phase are proportional to the RF probe signal. The eleven 100 KHz signals were stored on three Tektronix scopes, each with four-trace capacity. See Figure 6.8 for a block diagram of this system. Although it was possible to obtain phase and amplitude in this manner, only a small time interval could be stored. It was decided to use quadrature phase detection so that the entire shot could be digitally stored but at reduced bandwidth.

In the quadrature phase detection system twenty-two Mini-Circuit ZAD-1 mixers were arranged to produce $B_1\cos\theta$ and $B_1\sin\theta$ terms for each of the RF probes (where θ is the relative phase and B_1 the RF amplitude). The block diagram of the circuit is shown in Figure 6.9, and for further details of phase detection

circuits refer to Appendix A. The output of each mixer is low-passed filtered and, after a preamp, the information is digitally stored. Data manipulation and storage uses a number of Lecroy 8800/12 memory modules and a 8212 data logger. The dynamic RAM in the memory module is 8,000 words per channel and uses a 40 KHz sample rate. Maximum frequency response is limited to 10 KHz in the preamp filters. Data from each plasma shot is initially stored on disk but is transferred to a large computer system for data analysis.

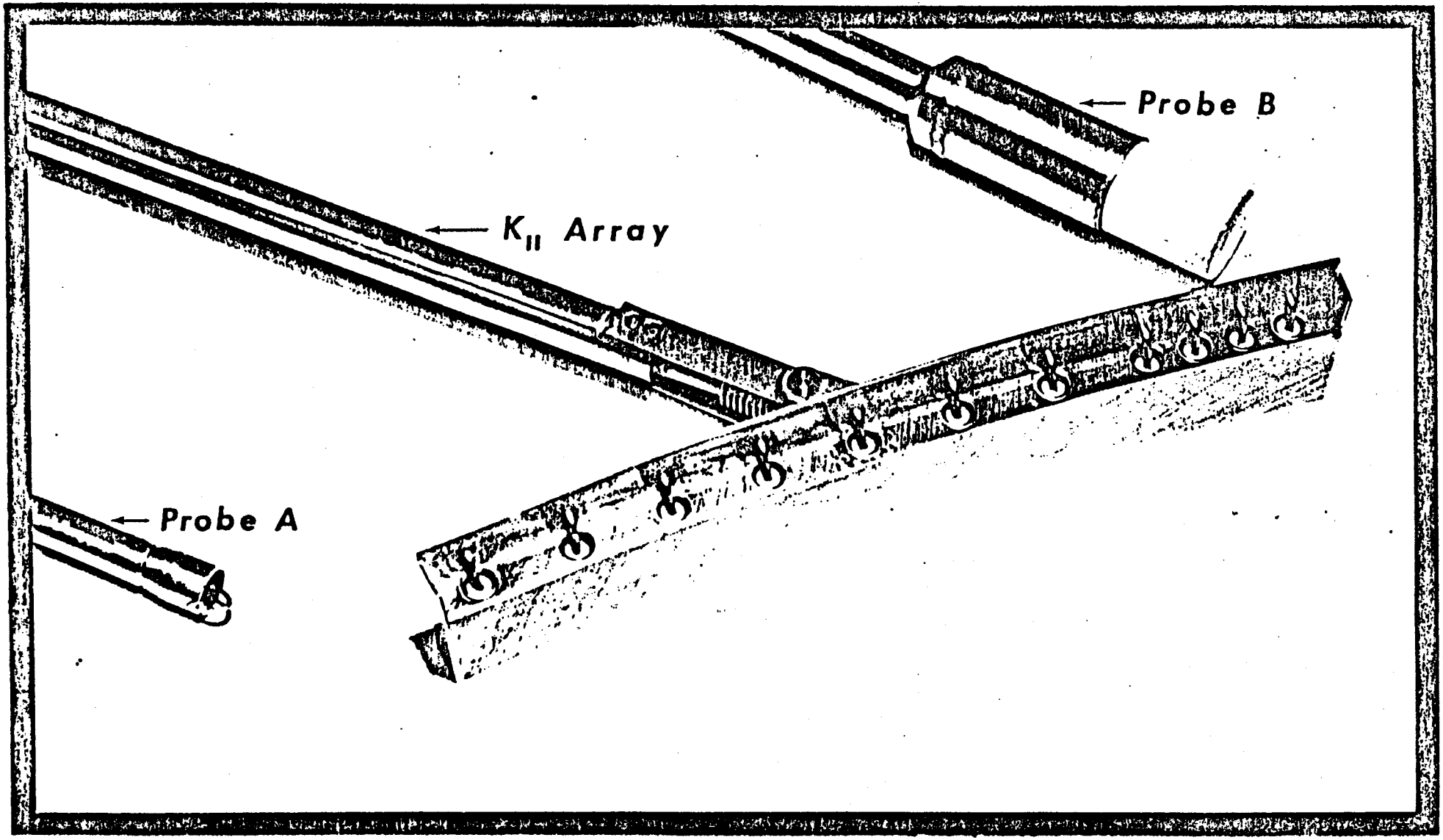

Figure 6.6. Front view of the $k_{\parallel}$ array. Note that the bellows and piot joint allows the probe to be folded during insertion. Probe A is a typical RF loop used to measure the magnetic fields of the fast compressional Alfven wave in the vacuum layer. Probe B is a hollow ceramic thimble in which experimental probes are inserted.

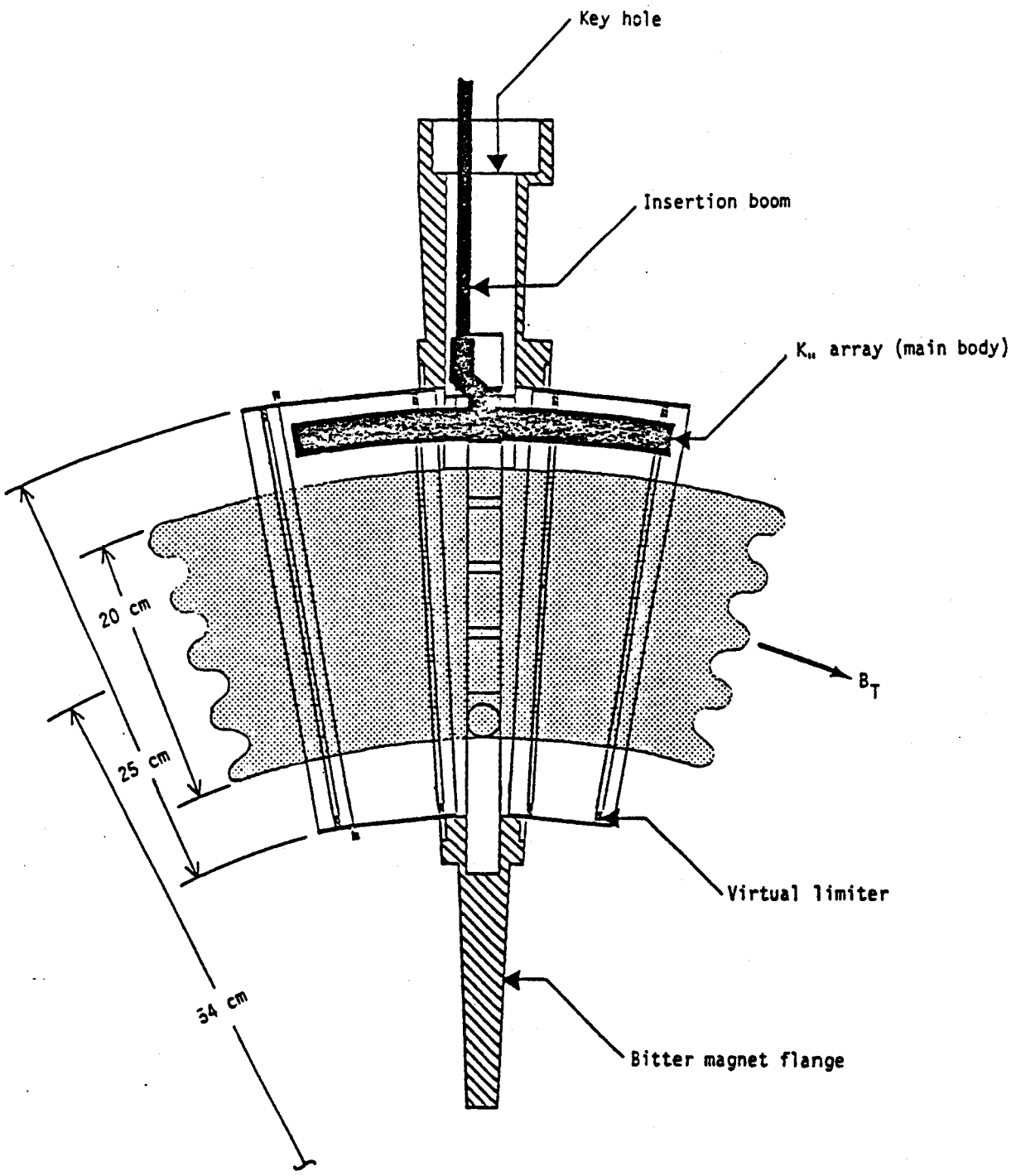

Figure 6.7. Location of $k_{\parallel}$ array in the Alcator A vacuum chamber. The array is inserted through the key hole and is held in place by the insertion boom.

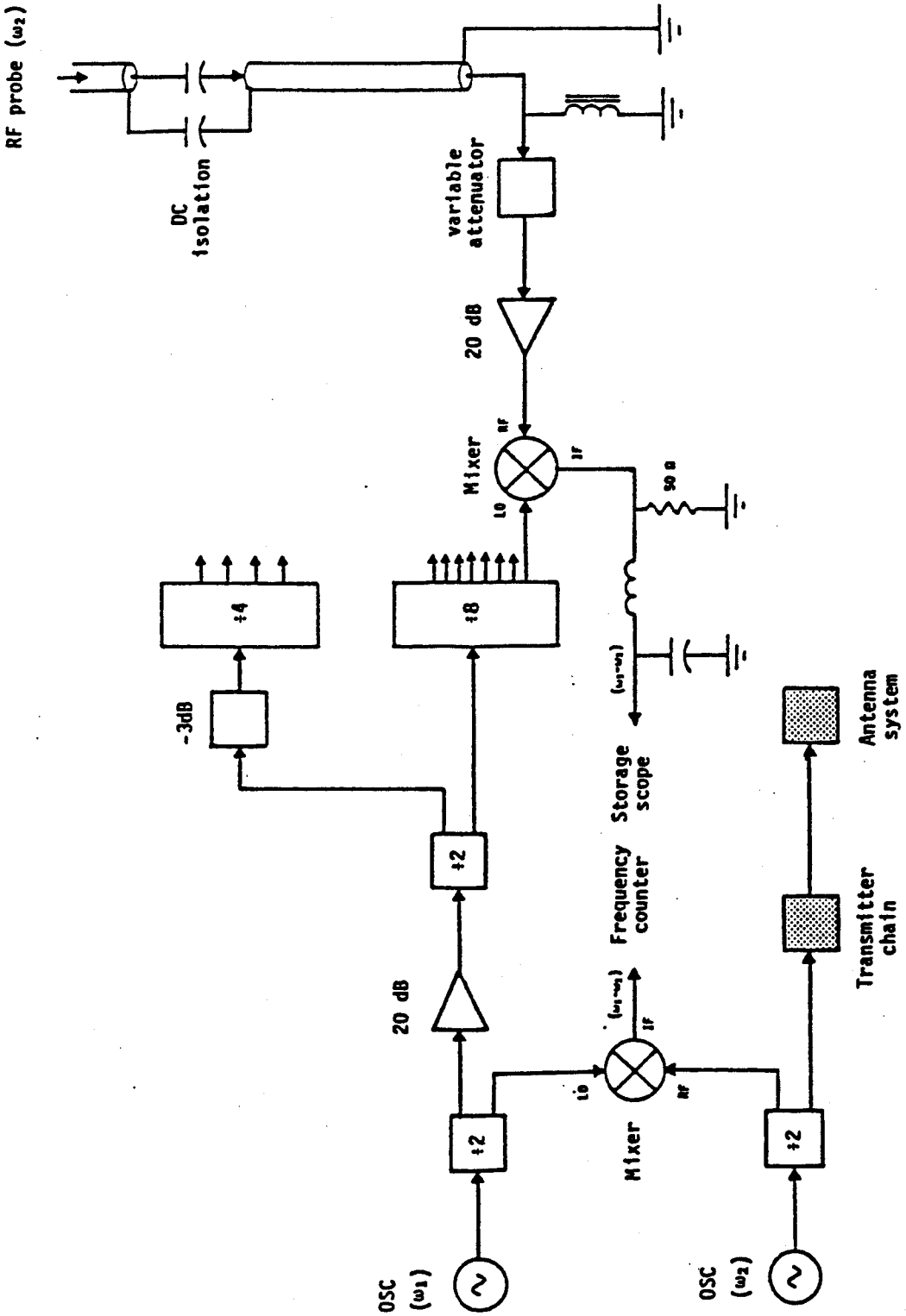

Figure 6.8. Block diagram of a heterodyne phase detection system. Note that only one complete input channel is shown.

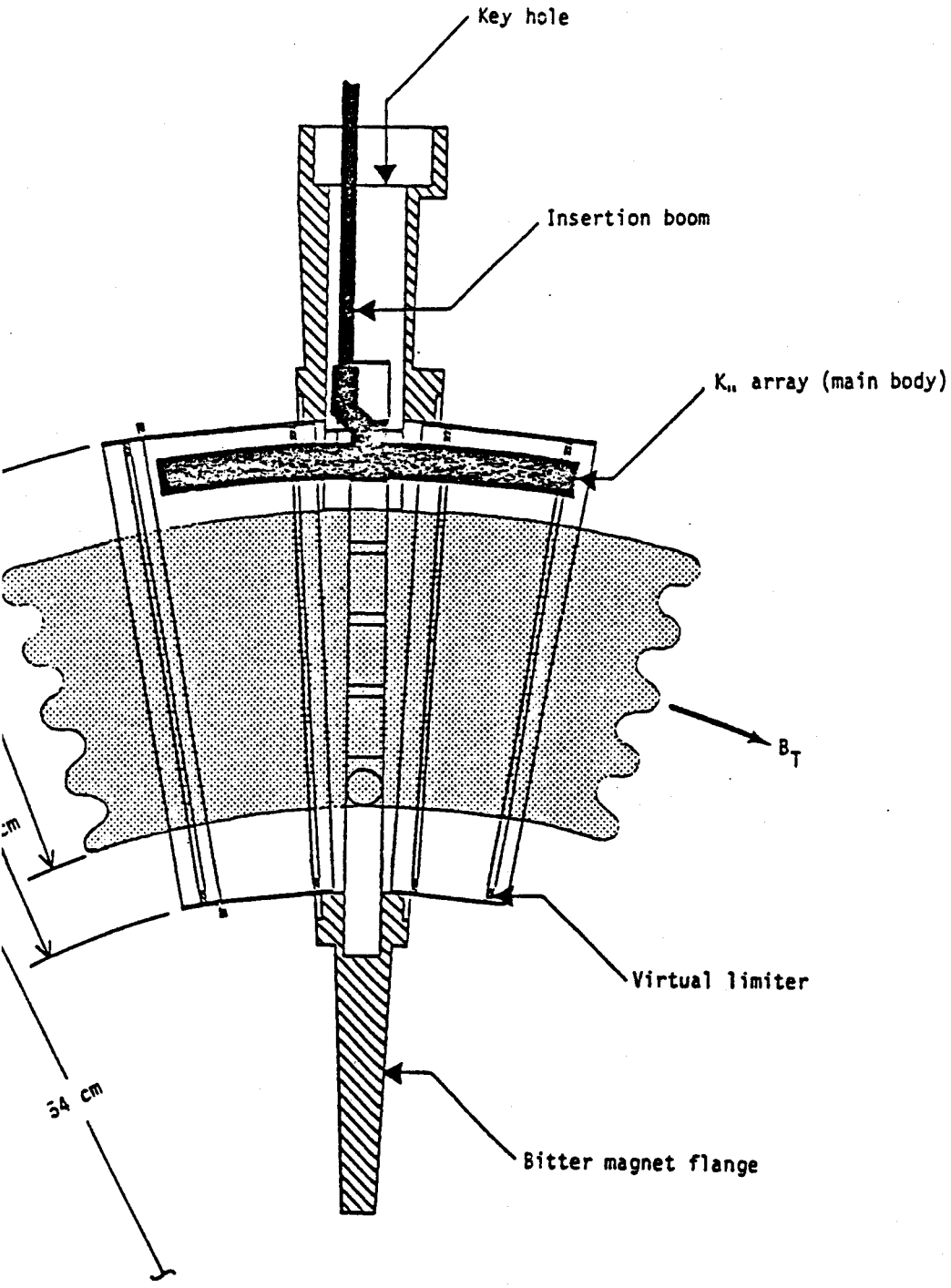

channel is shown.

Location of $k_{\parallel}$ array in the Alcator A vacuum chamber. The array is inserted through the key hole and is held in place by the insertion boom.

6.6 Radiation Resistance Computer

The radiation resistance is an important parameter in RF experiments of this nature. Figure 6.10 shows a simplified electrical model of an antenna which is inductively coupled to a plasma. In this model L_A represents the inductance of the antenna resulting from the near field, L_p is the inductance due to the wave field, R_p is the loading of the wave field, and R_R is resistive dissipation in the antenna. In general, $R_R \lesssim R_p \lesssim \omega L_p \lesssim \omega L_A$. Since resistive losses in the resonator are small compared to the coax feeders and since the resonator currents are on the same order as the antenna currents, it is safe to assume R_R and R_p account for the majority of the power dissipation. Therefore, R_p can be calculated as follows:

$$P = P_f - P_R = I_A^2(R_p + R_R)$$

$$R_p = \frac{P_F - P_R}{I_A^2} - R_R = \frac{V_f^2 - V_R^2}{50\ I_A^2} - R_R \qquad (6.2)$$

The solution to Equation 6.2 was accomplished in real time by a simple analog computer. Refer to Figure 6.11 for design details of this circuit. The forward and reflected powers for this calculation were measured by two 9" directional couplers located before the resonator, while the current I_A is obtained from the RF probe located near the end of the antenna. The signals V_F, V_R and I_A were detected by a 8471A Hewlett Packard diode. The 8471A is a broadband, half-wave detector exhibiting flat frequency response and low SWR. Depending on the power applied, this detector can operate as a square-law or linear device. The square law region exists from approximately -15 dBm

to -45 dBm and the linear operations occur when the input level is above +7 dBm. The square law region is very useful since the quantities needed are V_F^2, V_R^2, and I_A^2. In order to improve the square-law accuracy for a dynamic range of 20 dB, a diode-resistor compensating network was used. The rectified output of the 8471A diode first drives a buffer amplifier and, after the compensating networks, the signal is again buffered. The three stages for V_F, V_R and I_A are identical. In order to subtract V_R^2 from V_F^2, V_R^2 is first inverted, then summed with V_F^2. The output of this summing amplifier is proportional to the power dissipation. To divide by I_A^2 an operational amplifier, model 435 made by Analog Devices, was used. This device has wide bandwidth and excellent linearity which allows it to achieve very high performance in divider application from dc to 250 KHz. It uses a precision transconductance multiplier in the feedback loop of a typical op-amp, as shown in the figure below.

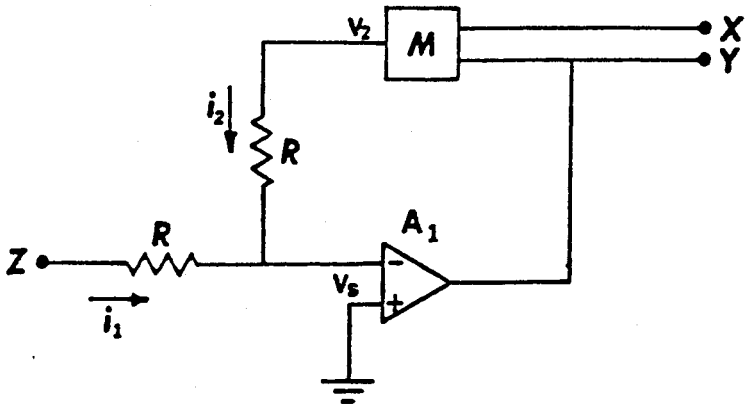

The transfer function of the multiplier "M" is $V_2 = -XY/10 - \varepsilon$ where ε represents error terms. Considering the input and feedback voltage loops, two equations can be formulated.

$$V_s + i_2 R + V_2 = 0$$

$$V_s + i_1 R + Z = 0$$

Since A_1 has very large gain, $V_s \approx 0$ and $i_1 = -i_2$ because of large input impedance. With these approximations:

$$-Z = V_2 = \frac{-XY}{10} - \epsilon$$

$$Y = \underbrace{\frac{10Z}{X}}_{\text{ideal division}} - \underbrace{\frac{10\epsilon}{X}}_{\text{error term}}$$

The error term includes: noise error, offset error, offset drift error, X nonlinearity error, and Y nonlinearity error. The signal-independent errors can be trimmed out and overall accuracy is less than 0.1% of full scale output. The output of this device gives the radiation resistance as a function of time and is displayed on a Tektronix storage scope. Figure 6.12 shows typical data for V_F, V_R, I_A and the analog calculation of R.

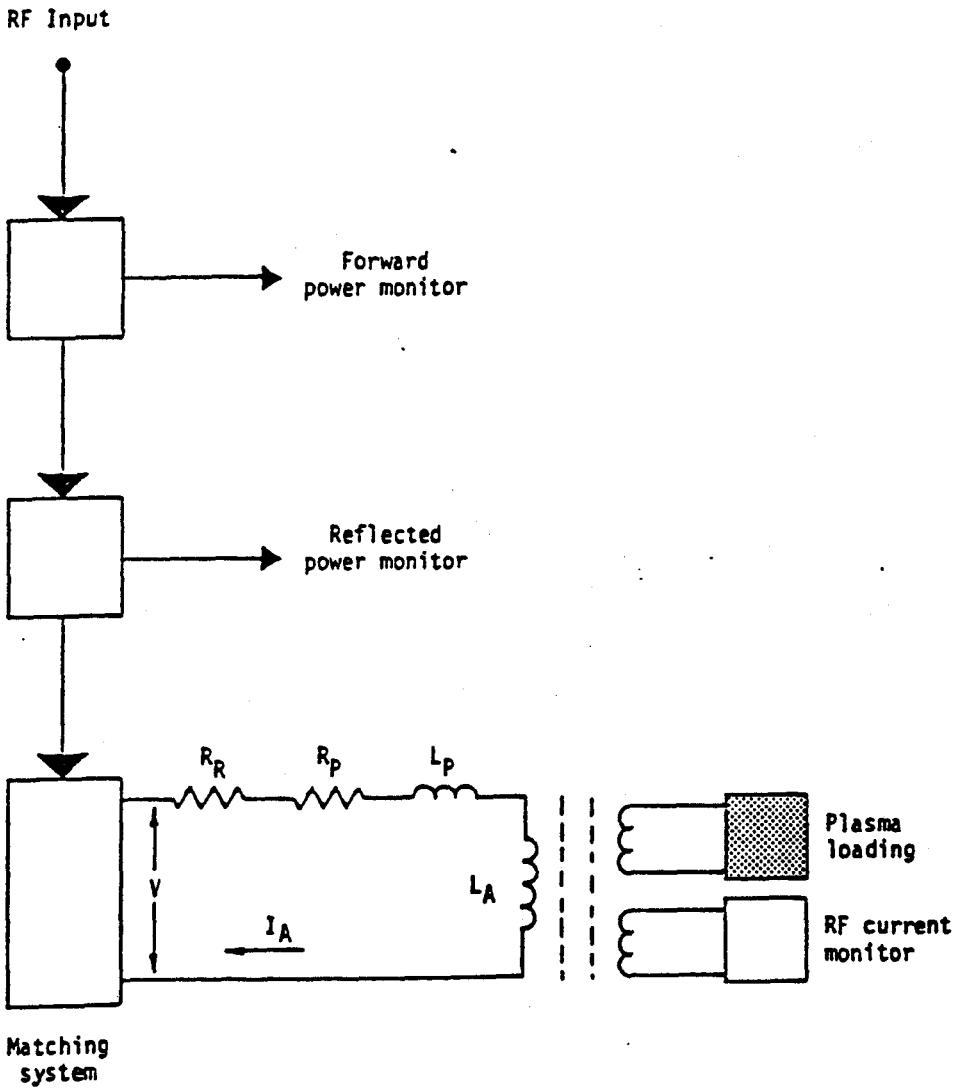

Figure 6.10. Equivalent circuit of the antenna system.

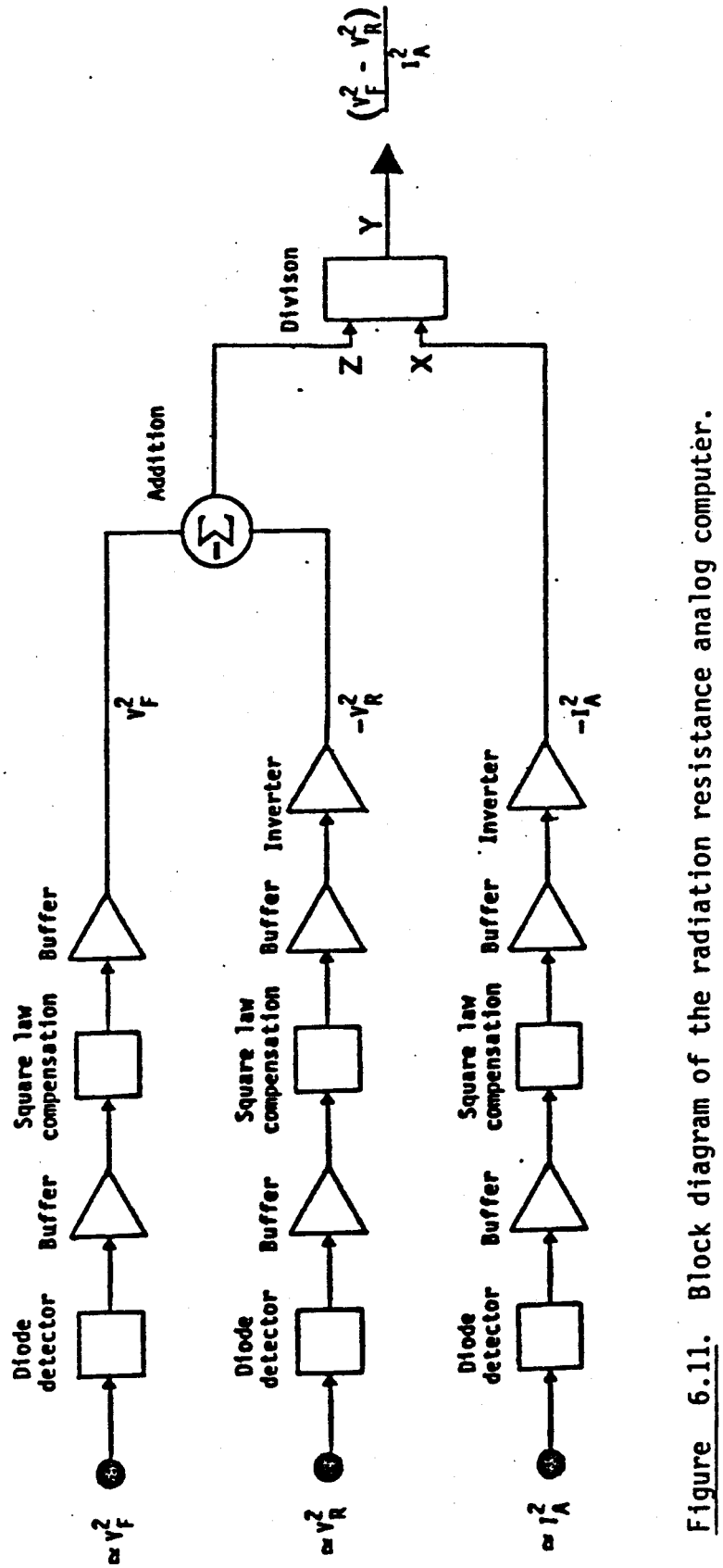

Figure 6.11. Block diagram of the radiation resistance analog computer.

A_2 Antenna (unshielded)

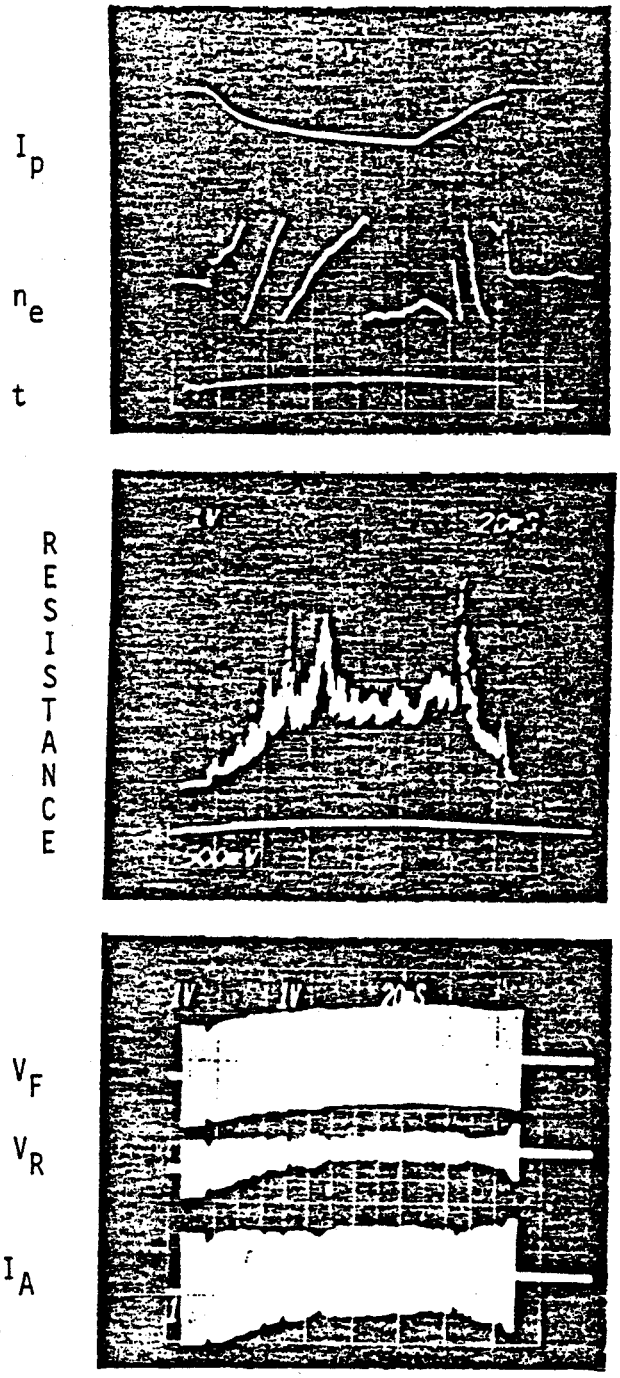

Figure 6.12. Radiation resistance as a function of time for 90 MHz, 95% D, 5% H and 49.5 KG. The signals V_F, V_R, and I_A are used to calculate R.

7. EXPERIMENTAL RESULTS

7.1 The Measurement of $k_{\parallel}$ and Q

The interpretation of the results from the $k_{\parallel}$ array requires a strong understanding of lossy resonant systems. In order to gain insight into this problem, consider a toroidal waveguide system of circumference 2L with an antenna located at z=0. The antenna launches waves in the +z and -z direction which travel around the torus a number of times, depending on how strongly they are damped. These waves interfere, and the following equation describes the field structure when the wave number is independent of propagation direction:

$$E(z) = \sum_i E_i \left[\sum_{n=0}^{\infty} e^{j\beta_i(nL+z)} + \sum_{n=1}^{\infty} e^{j\beta_i(nL-z)} \right] \qquad (7.1)$$

where i, n represent the sum over different modes and sum over toroidal passes, respectively.

This equation simplifies to:

$$E(z) = \sum_i E_i \frac{j\cos\beta_i(z-L)}{\sin\beta_i L} \qquad (7.2)$$

where $\beta_i = k_{\parallel} + jk_i$

The experimental reduced data from the $k_{\parallel}$ array provides the amplitude and phase of the wave at eleven discrete points in the toroidal direction. In a similar manner, one can plot the amplitude and phase of Equation 7.2 as a function of z for different values of $k_{\parallel}$ and k_i in order to gain insight into the experimental results.

When a wave is in toroidal resonance, the theoretical phase and amplitude is plotted from z=0 to z=L in Figure 7.1. One interesting feature is that the ratio of the mode amplitude at resonance to anti-resonance increases for

larger toroidal positions, with the largest ratio occurring halfway around the torus. At this point the +z wave and the -z wave have traveled equal distances and have therefore been damped by the same amount, which results in strong eigenmodes. At other toroidal locations either the +z wave or the -z wave will have a greater amplitude, and complete interference cannot occur.

Figures 7.2 and 7.3 show the theoretical results for one resonant value of $k_{\parallel}$, but for various damping lengths. The lightly damped case is characterized by large amplitude excursions and rapid phase changes. For these situations the maximum phase change occurs at the anti-resonance point, and the wavelength is equal to twice the distance between amplitude peaks. The wavelength is also equal to twice the distance between the points of greatest phase change.

On the other hand, for the highly damped waves the phase change is roughly linear as a function of toroidal position, and $k_{\parallel}$ is equal to the slope of the phase. All these methods were employed in finding $k_{\parallel}$ from the experimental probe data.

In many cases we observed rapid phase changes (indicating light damping) but only moderate amplitude excursions in the experimental data. This seems to contradict previous statements until one realizes that most of the data from the heterodyne detection system was taken when the modes were out of toroidal resonance. Figure 7.4 compares the situation when modes are in toroidal resonance and out of toroidal resonance. When $k_i = 2 \times 10^{-4}$ cm^{-1} the ratio of maximum amplitude for $k_{\parallel} = 0.19$ cm^{-1} to $k_{\parallel} = 0.12$ cm^{-1} is 30:1. Note that in these two cases the amplitude of the anti-resonance is close to zero and the shapes of the phase change are similar. When $k_i = 2 \times 10^{-3}$ cm^{-1} the ratio of maximum amplitude for $k_{\parallel} = 0.19$ cm^{-1} to $k_{\parallel} = 0.12$ cm^{-1} is only 3:1.

Finally, Figure 7.1 theoretically demonstrates the effects of phase and amplitude as a function of $k_{\parallel}$ when k_i is constant. Note that the largest slope of the phase change with respect to $k_{\parallel}$ occurs at toroidal resonance.

With the number of data points available from the $k_{\parallel}$ array, if more than one mode is present it becomes extremely difficult to analyze the situation. In most cases, when we computed $k_{\parallel}$ we looked for good mode separation and theoretical consistency between amplitude and phase signals. Figures 7.5, 7.7 and 7.9 show the amplitude and phase obtained from the heterodyne detection system for a hydrogen plasma at 200 MHz. The calculated $k_{\parallel}$ and k_i are listed in the figures. It should be noted that $k_{\parallel}$ not only determines the distance between the maximum and minimum amplitudes, but also affects their position with respect to the $k_{\parallel}$ array since the antenna always lies at an amplitude maximum. The shape and position of the computer plots in Figures 7.6, 7.8, and 7.11 for the chosen value of $k_{\parallel}$ and k_i seems to agree fairly well with the experimental data.

Figure 7.11 is a comparison of the experimental and theoretical results of the amplitude and phase signals obtained from the quadrature phase detection system. At first glance for t = 80 ms one would infer that there exists large damping since the phase change appears to be linear. However this is not the case since the predicted $k_{\parallel} = 0.07\ cm^{-1}$ and $k_i = 2 \times 10^{-3}\ cm^{-1}$. In this situation the wavelength is much longer than the length of the array and as a result you observe only a small portion of the complete phase and amplitude variations. As $k_{\parallel}$ changes from $0.07\ cm^{-1}$ to $0.09\ cm^{-1}$ an amplitude maximum at t = 80 ms changes into an amplitude minimum at t = 100 ms. Compare this to Figure 7.10 where the phase change near an amplitude peak is linear over a small toroidal region and there exists rapid phase changes near an amplitude minimum.

An important parameter in resonant systems is the quality factor, or Q value:

$$Q = \frac{\omega W}{P_{dis}} = \frac{\omega}{\Delta\omega}$$

For a given damping length, the value of Q is related to the parallel group velocity of the wave when radial eigenmodes exist by the following expression:

$$Q = \frac{\omega}{2k_i V_{g\parallel}} \tag{7.3}$$

From the dispersion relationship, one can calculate $V_{g\parallel}$:

$$k^2_{\parallel} + 1/2k^2_{\perp} = \frac{k^2 A}{(1 + \Omega)}$$

$$V_{g\parallel} = \frac{\partial\omega}{\partial k_{\parallel}} = \frac{\partial k_{\parallel}}{\partial\omega}^{-1}$$

$$\frac{V_{g\parallel}}{\omega} = (1 + \Omega)^2 \frac{k_{\parallel}}{k^2 A} \tag{7.4}$$

Equations 7.3 and 7.4 indicate that during mode onset a heavily damped wave can still have a large Q. This results because at $k_{\parallel} \approx 0$ the wave propagates mostly in the radial direction.

The value of Q can also be calculated from a single probe, provided good mode separation exists. During a monotonic density rise, a particular mode will alternately undergo toroidal resonance and anti-resonance as a result of the change of $k_{\parallel}$. By comparing the amplitude of the mode during resonance (A_{res}) to anti-resonance ($A_{ant\text{-}res}$), one can approximately obtain k_i by the following formula:

$$k_i = \frac{1}{2\pi r} \ln\left[\frac{Y+1}{Y-1}\right] \tag{7.5}$$

where $Y = \frac{A_{res}}{A_{ant\text{-}res}}$

Using this method in conjunction with Equation 7.3, we have identified Q = 1 to Q = 1,000 for various experimental conditions.

In summary, for hydrogen or deuterium plasmas from $n_e = 1.5 \times 10^{14}$ to 3×10^{14} at 90 MHz ($\omega = \omega_{CH}, 2\omega_{CD}$), the range of $k_{\parallel}$ is 0.15 cm^{-1} to 0.35 cm^{-1}. For hydrogen plasmas around 1.5×10^{14} to 3×10^{14} at 200 MH_z ($\omega = 2\omega_{ci}$), the range of $k_{\parallel}$ is 0.15 cm^{-1} to 0.5 cm^{-1}. Refer to Figure 3.1 for comparison of theory and experimental data.

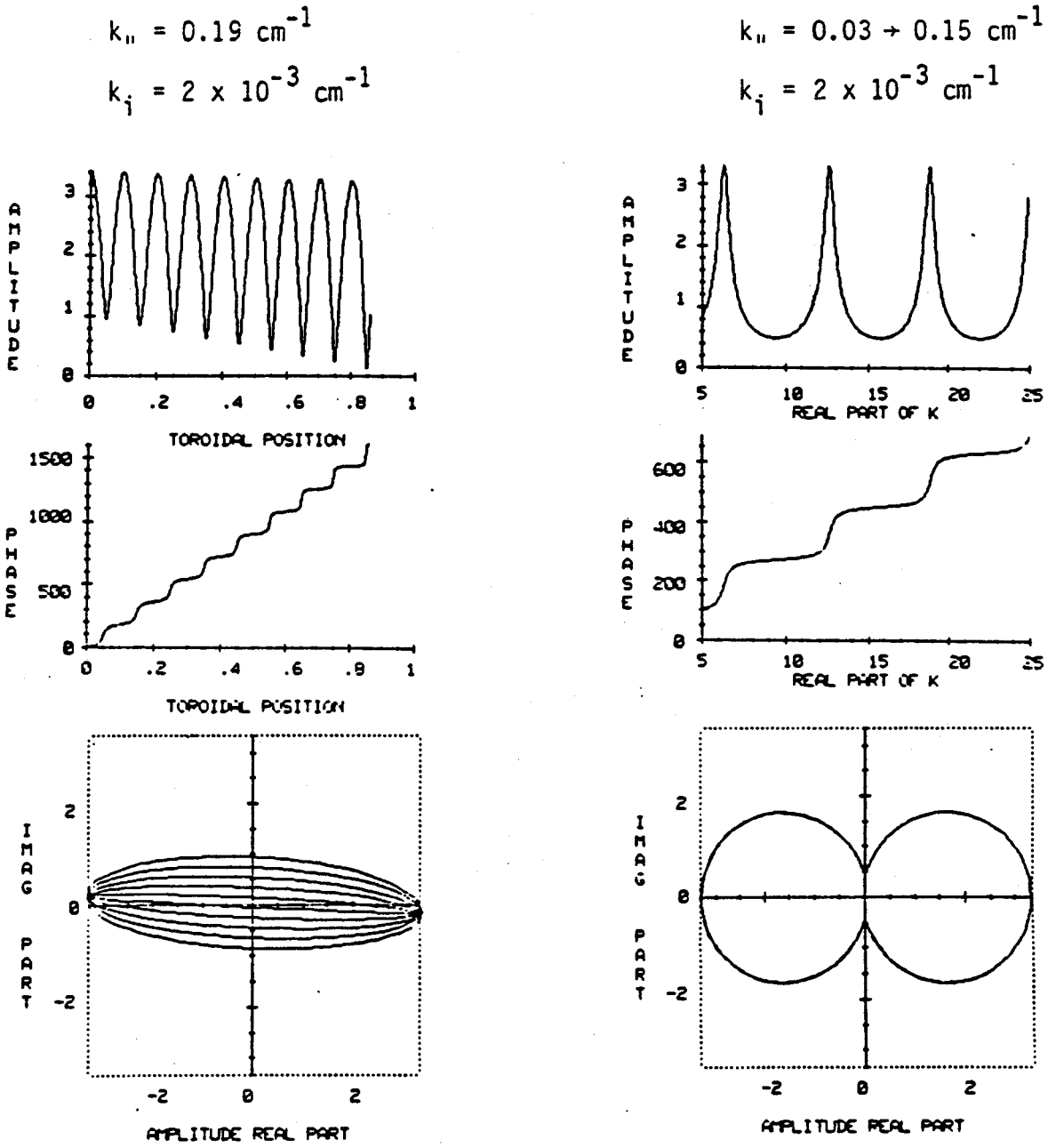

Figure 7.1. Solutions of Equation 7.2 for the indicated values of $k_{\parallel}$ and k_i where the abscissa is normalized by the parameter "L". (2L=torus circumference)

$k_{\parallel} = 0.19\ cm^{-1}$

$k_i = 2 \times 10^{-4}\ cm^{-1}$

$k_{\parallel} = 0.19\ cm^{-1}$

$k_i = 2 \times 10^{-3}\ cm^{-1}$

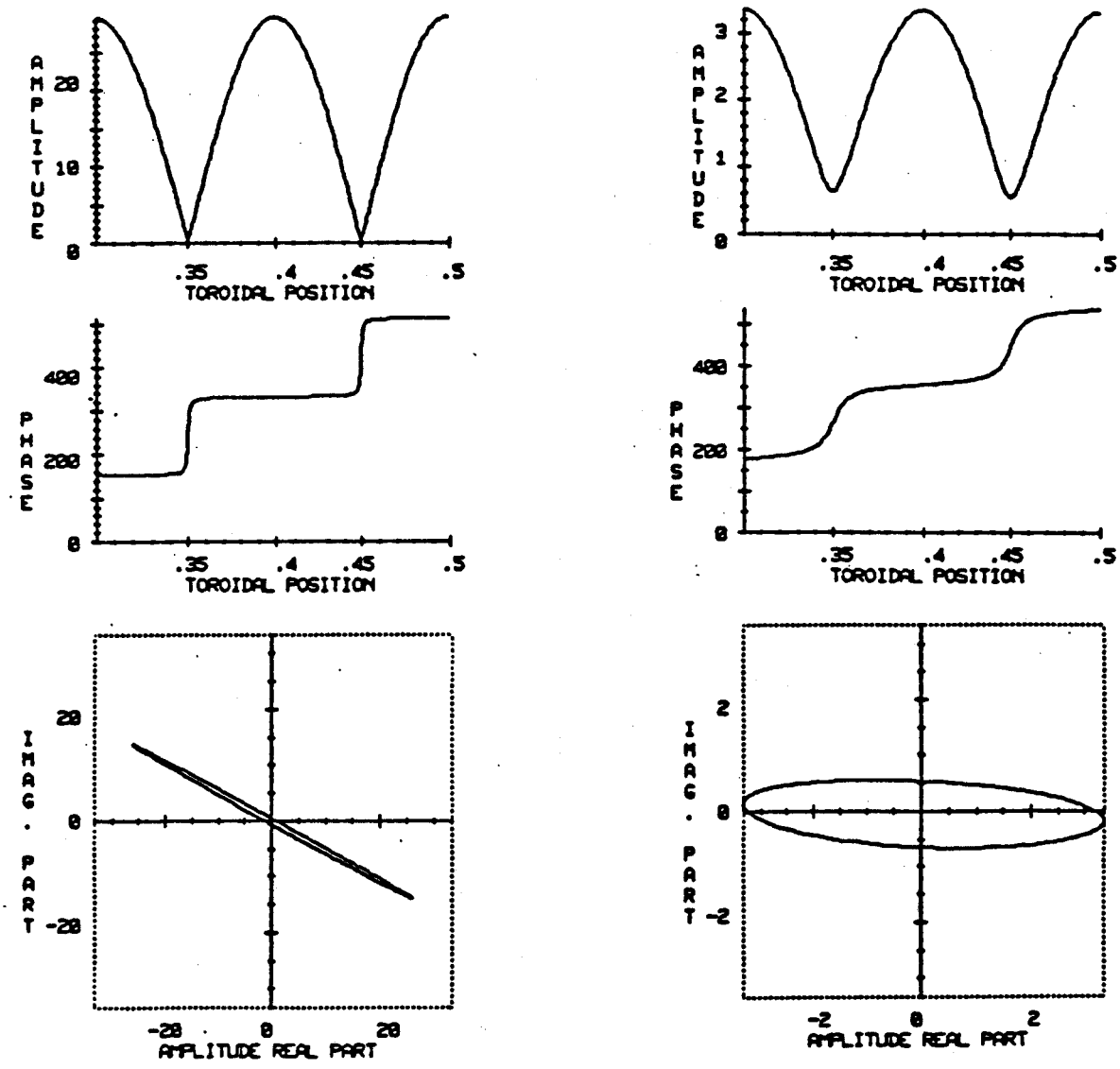

Figure 7.2. Solutions of Equation 7.2 for the indicated values of $k_{\parallel}$ and k_i where the abscissa is normalized by the parameter "L".

$k_{\parallel} = 0.19\ cm^{-1}$

$k_i = 6 \times 10^{-3}\ cm^{-1}$

$k_{\parallel} = 0.19\ cm^{-1}$

$k_i = 2 \times 10^{-2}\ cm^{-1}$

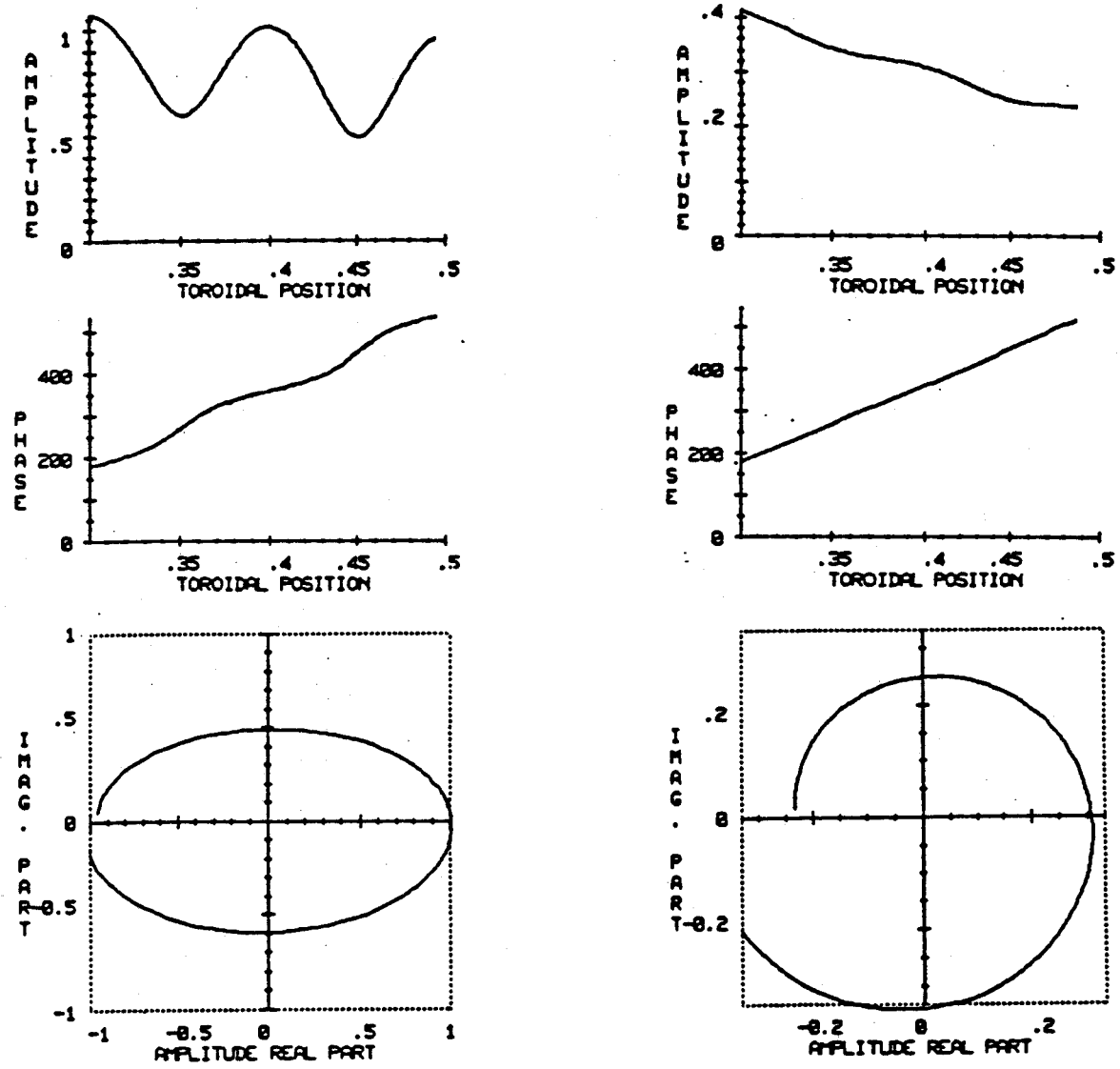

Figure 7.3. Solutions of Equation 7.2 for the indicated values of $k_{\parallel}$ and k_i where the abscissa is normalized by the parameter "L".

$k_{\parallel} = 0.19\ cm^{-1}$

$k_i = 2 \times 10^{-4}\ cm^{-1}$

In resonance

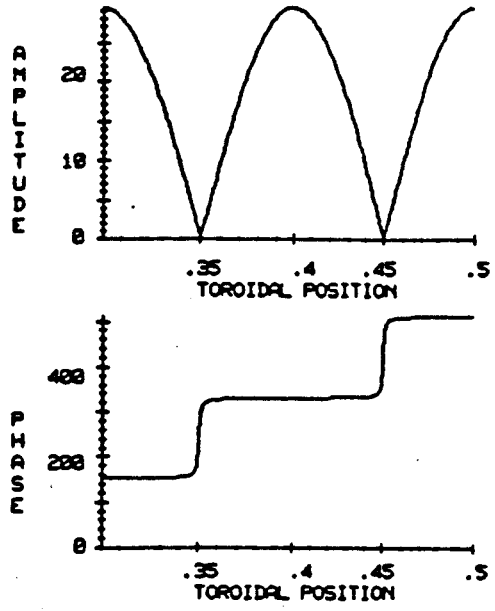

$k_{\parallel} = 0.12\ cm^{-1}$

$k_i = 2 \times 10^{-4}\ cm^{-1}$

Out of resonance

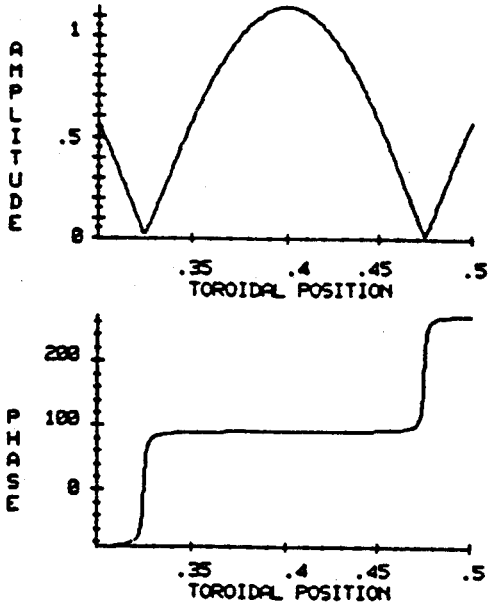

$k_{\parallel} = 0.19\ cm^{-1}$

$k_i = 2 \times 10^{-3}\ cm^{-1}$

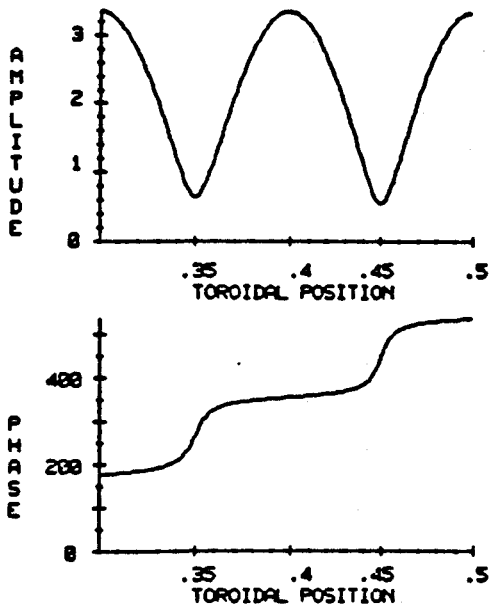

$k_{\parallel} = 0.12\ cm^{-1}$

$k_i = 2 \times 10^{-3}\ cm^{-1}$

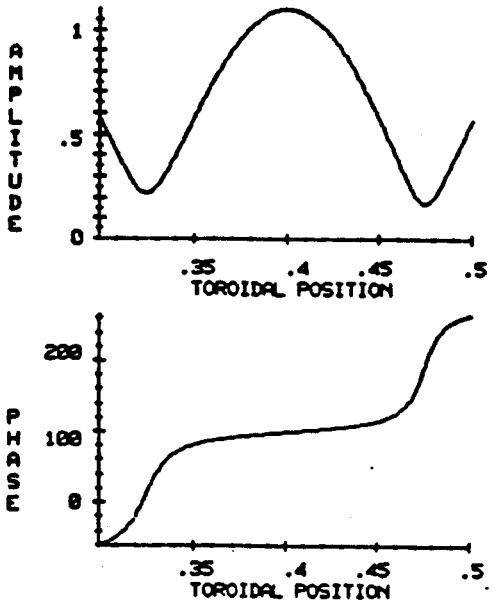

Figure 7.4 . Solutions of Equation 7.2 for the indicated values of $k_{\parallel}$ and k_i where the abscissa is normalized by the parameter "L".

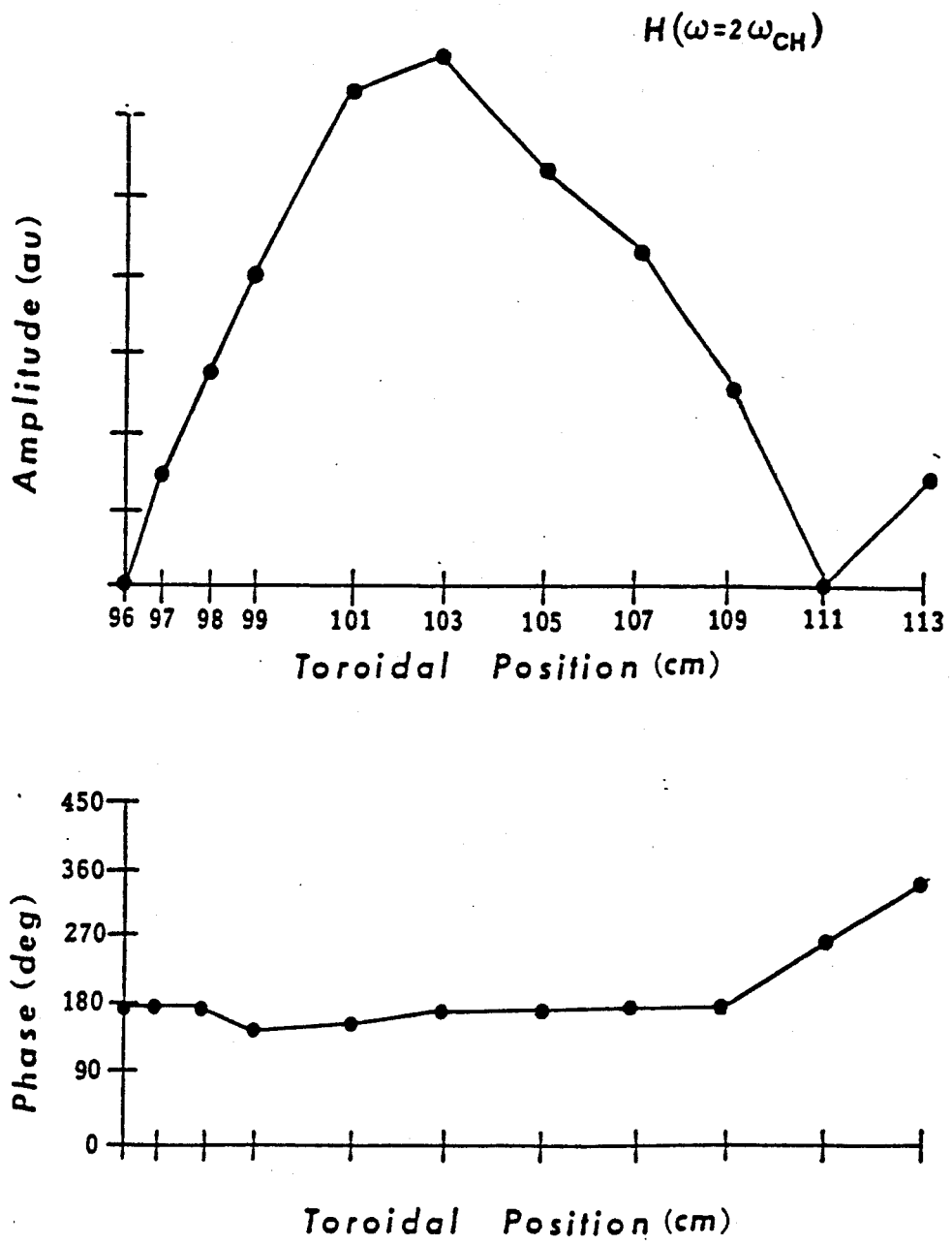

Figure 7.5 . Reduced probe data from the $k_{\parallel}$ array which was obtained from the heterodyne detection system. Computer modeling implies $k_{\parallel} \cong 0.23\ cm^{-1}$ and $k_i \cong 6 \times 10^{-4}\ cm^{-1}$.

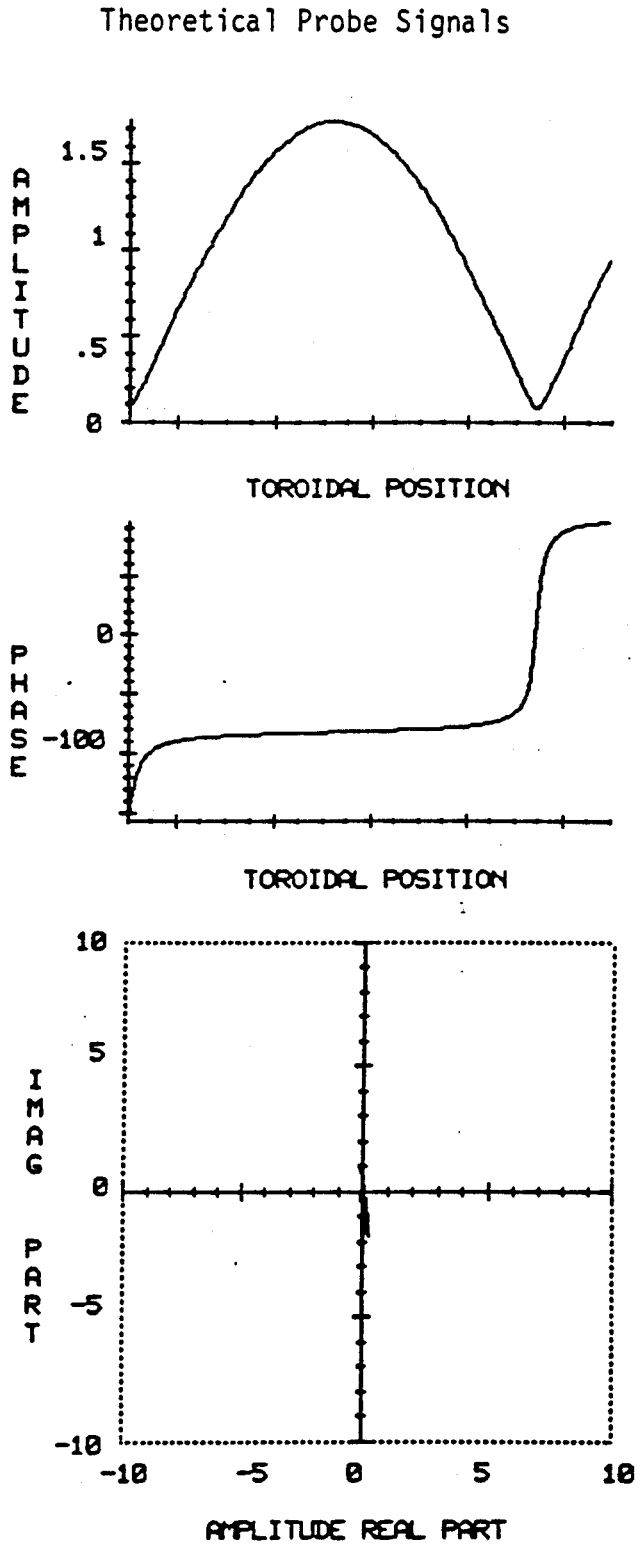

Figure 7.6. Computer modeling of experimental data in Figure 7.5 yield $k_{\parallel} \cong 0.23\ cm^{-1}$ and $k_i = 6 \times 10^{-4}\ cm^{-1}$.

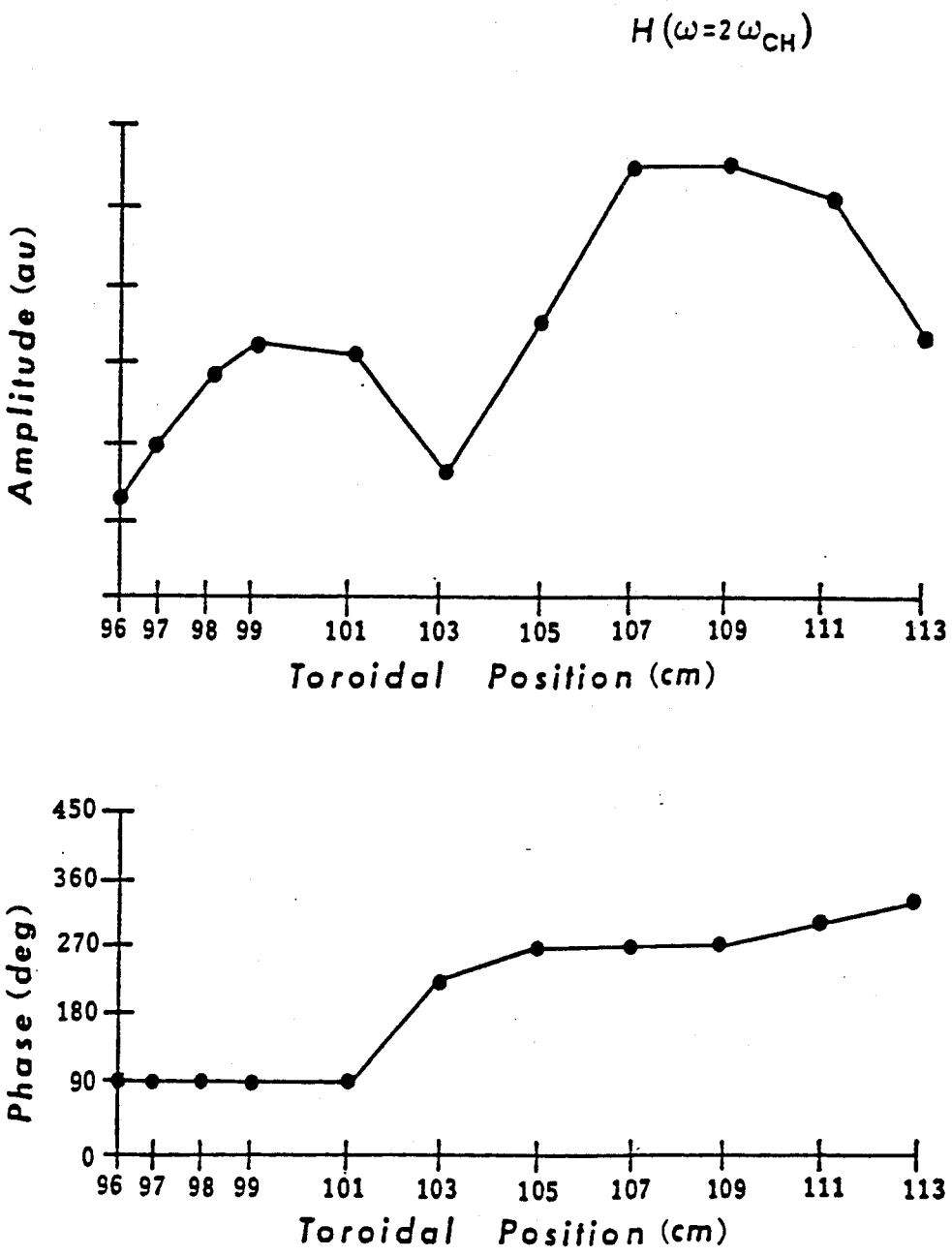

Figure 7.7. Reduced probe data from the $k_{\parallel}$ array which was obtained from the heterodyne detection system. Computer modeling implies $k_{\parallel} \cong 0.35\ cm^{-1}$ and $k_i \cong 2 \times 10^{-3}\ cm^{-1}$.

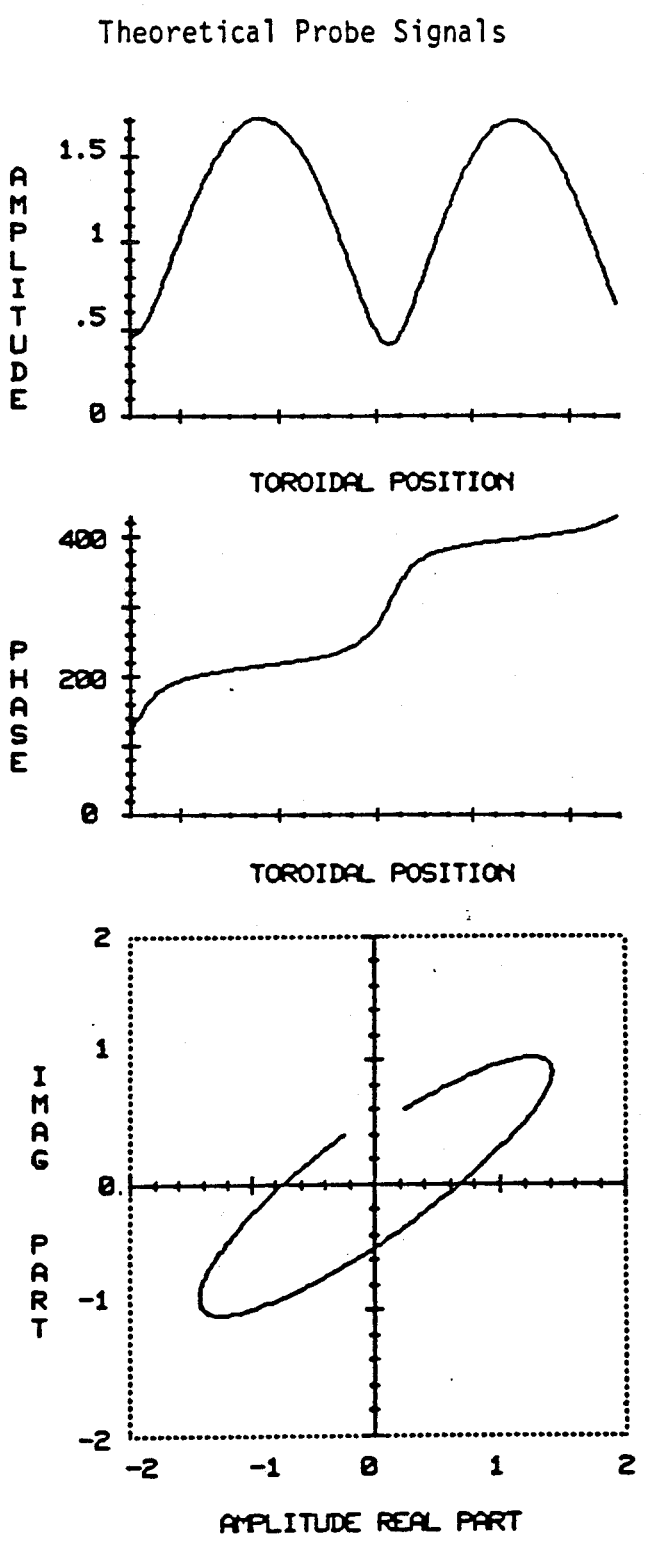

Figure 7.8. Computer modeling of experimental data in Figure 7.7 yield $k_{\parallel} = 0.35\ cm^{-1}$ and $k_i = 2 \times 10^{-3}\ cm^{-1}$.

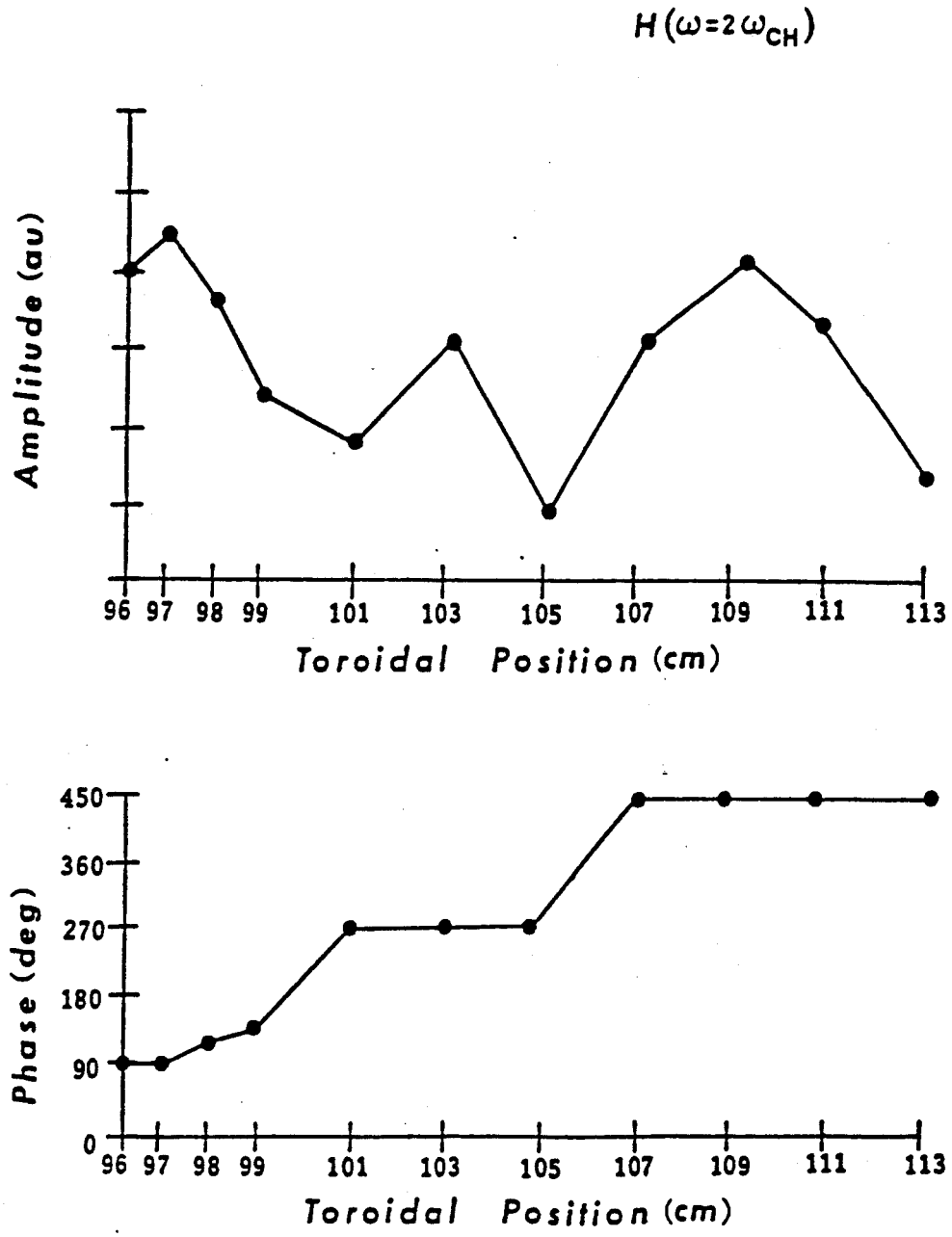

Figure 7.9. Reduced probe data from the $k_{\parallel}$ array which was obtained from the heterodyne detection system. Computers modeling implies $k_{\parallel} \cong 0.52\ cm^{-1}$ and $k_i \cong 6 \times 10^{-4}\ cm^{-1}$.

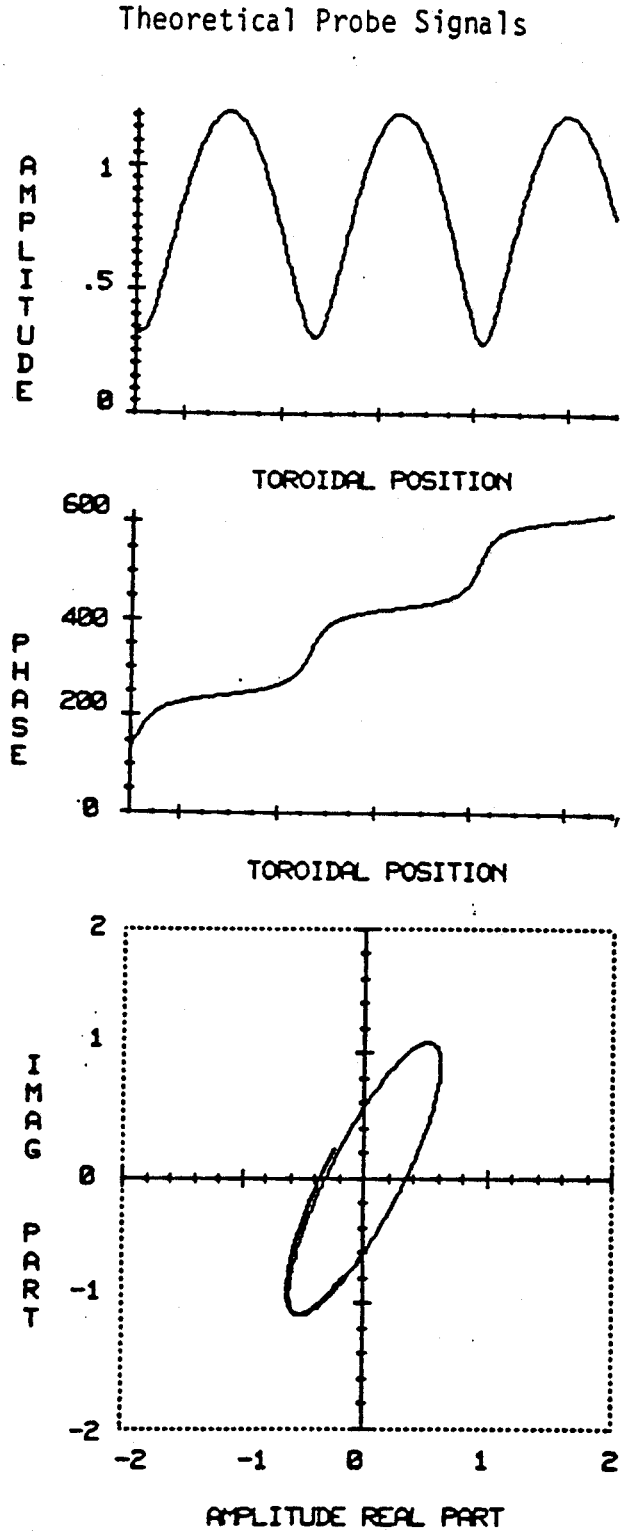

Figure 7.10. Computer modeling of experimental data in Figure 7.9 yield $k_{\parallel} = 0.52\ cm^{-1}$ and $k_{\perp} = 6 \times 10^{-4}\ cm^{-1}$.

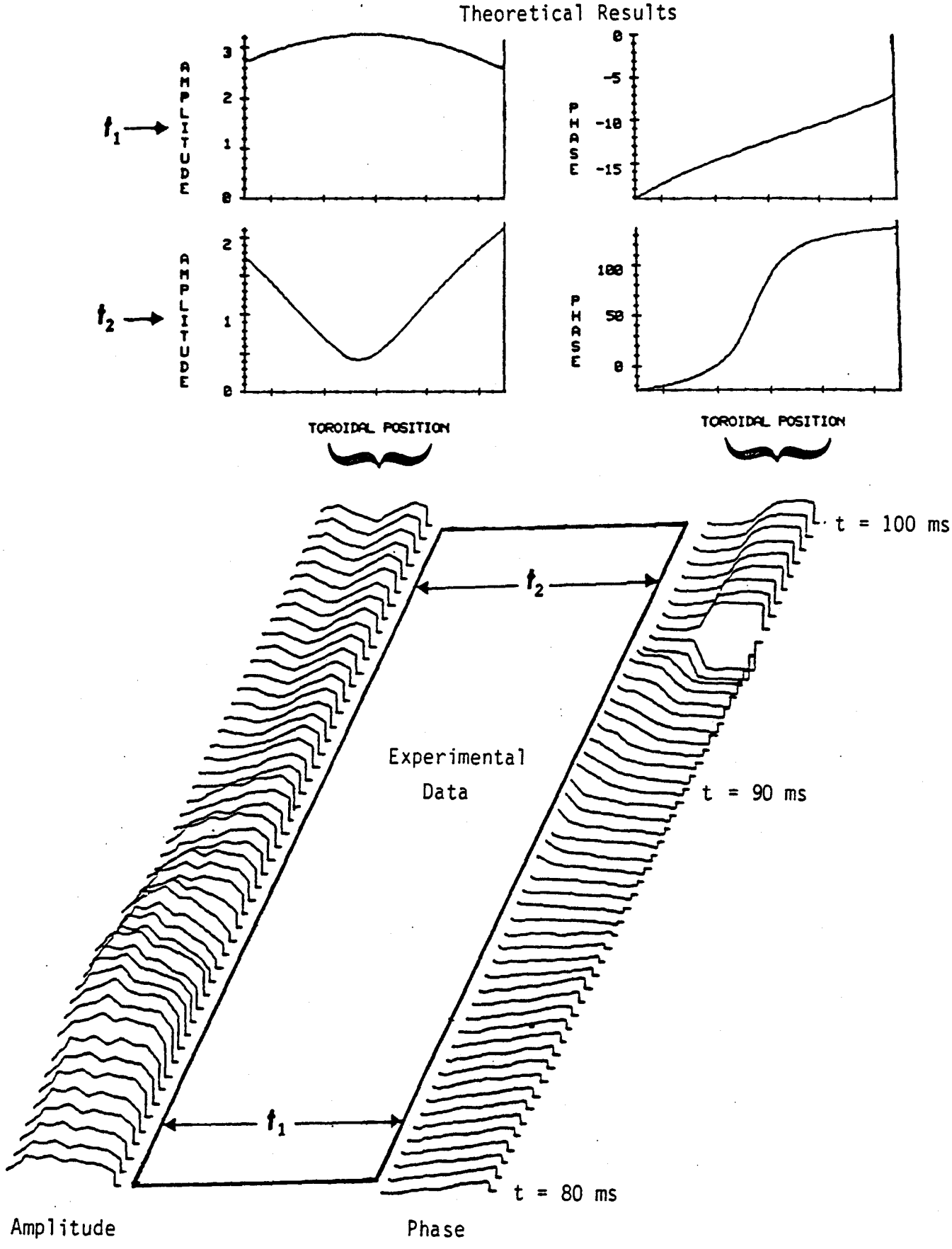

Figure 7.11. Comparison of experimental and theoretical results for the amplitude and phase signal obtained from the quadrature phase detection system during a monotonic density rise in time.

7.2 Experimental Damping Mechanisms

Using the experimental values of $k_{\parallel}$ obtained previously, one is able to qualitatively examine power balance from particle-wave interactions. By varying the toroidal magnetic field it is possible to partially isolate the effects of key damping mechanisms and gain insight into the absorption process. When applicable, pure second harmonic damping ($Q_{2\omega_c}$), minority absorption (Q_{Min}), Ion-ion hybrid resonance (Q_{II}), electron Landau damping (Q_E), wall loading (Q_W), pure fundamental absorption (Q_{ω_c}), and ion-cyclotron mode conversion (Q_{IC}) will be examined. The values of Q for these processes are determined by Equations 5.1, 5.2, 5.4, 5.5, 5.7, 5.8, and 5.9, respectively. It should be noted that the mechanisms with the largest value of Q will absorb the least energy from the wave. Therefore, the theories on damping can be examined by comparing the theoretical values of Q with the total Q_T obtained from the experiment, where Q_T is related to the individual Q_i by:

$$\frac{1}{Q_T} = \sum_i \frac{1}{Q_i}$$

7.2.1 Deuterium and Hydrogen Minority Plasma ($\omega = 2\omega_{CD}, \omega_{CH}$)

A plasma consisting mainly of deuterium with a minority component of hydrogen is one of the most promising candidates for tokamak heating. The transmitter frequency for this experiment was 90 MHz, and the plasma was 95% deuterium with a 5% hydrogen minority. The sole source of the minority component was hydrogen retention on the vacuum chamber walls from previous runs. The table on the next page represents the theoretical values of Q for the different dampin mechanisms and for various values of density, toroidal magnetic field, and $k_{\parallel}$.

Table 7.1 Theoretical values of Q for various damping mechanisms.

$N = 1.5 \times 10^{14}\ cm^{-3}$

B_T(KG)	$\frac{\omega}{\omega_{CH}}$	$k_{\parallel}(cm^{-1})$	Q_W	Q_E	Q_{Min}	$Q_{2\omega_c}$	Q_{II}	Q_T
49.5	1.20	0.15	1,990	2,620	--	--	--	1,130
		0.35	8,670	370				355
58.6	1	0.15	2,070	3,820	11	385	8	5
		0.35	11,800	706	40	3,092	6	5
71.4	0.83	0.15	2,210	6,140	--	--	--	1,630
		0.35	25,070	4,380				3,730

$N = 3 \times 10^{14}\ cm^{-3}$

B_T(KG)	$\frac{\omega}{\omega_{CH}}$	$k_{\parallel}(cm^{-1})$	Q_W	Q_E	Q_{Min}	$Q_{2\omega_c}$	Q_{II}	Q_T
49.5	1.20	0.15	2,230	1,252	--	--	--	802
		0.35	6,420	137				134
58.6	1	0.15	1,930	1,784	11	166	8	4
		0.35	7,200	214	17	352	7	5
71.4	0.83	0.15	2,000	2,760	--	--	--	1,160
		0.35	8,880	396				379

When $N_e = 3 \times 10^{14}$ cm^{-3} and $B_T = 71.4$ KG, the ratio of the mode amplitude during resonance to anti-resonance is about 8:1 for RF probe P_2 in Figure 7.12. From Equation 7.5 this ratio represents an experimental Q_{EX} = 1,150 if the mode's $k_{\parallel} = 0.15$ cm^{-1}, and $Q_{EX} = 428$ if $k_{\parallel} = 0.35$ cm^{-1}. The theoretical values of Q closely agree with these results, since $Q_T = 1,160$ for $k_{\parallel} = 0.15$ cm^{-1}, and $Q_T = 379$ for $k_{\parallel} = 0.35$ cm^{-1}. From the theoretical values of Q it should be noted that for $k_{\parallel} = 0.35$ cm^{-1} the electrons essentially receive all the power from the wave, and therefore limit the value of Q. However, for $k_{\parallel} = 0.15$ cm^{-1} both electron absorption and wall loading are important processes for wave damping. This indicates that the larger values of $k_{\parallel}$ could efficiently produce electron heating in this parameter range. The lower density results have similar trends, although the magnitudes of the Q's are larger. The radiation resistance and the probe signals demonstrate the increased toroidal eigenmodes resulting from the larger values of Q_T at lower densities.

When $N_e = 3 \times 10^{14}$ and $B_T = 58.6$ KG, the radiation resistance and RF probes indicate strong damping since toroidal eigenmodes do not exist. The theoretical value of Q_T also agrees with this statement since, for the minority concentrations present in this experiment the ion-ion hybrid dominates with a Q=3.

Therefore, most of the wave energy will be deposited into the Ion Bernstein branch,while a small portion will directly heat the protons via the fundamental resonance. The Ion Bernstein wave will heat electrons via Landau damping, and if this wave propagates back to the center of the machine proton and deuteron heating will occur. However, direct coupling to the electrons and deuterons from the original wave will be small.

When $N_e = 1.5 \times 10^{14}$ cm^{-3} and $B_T = 58.6$ KG, the fundamental resonant layer is centered in the machine, and the theoretical results do not agree with the experiment. According to the probe signal P_2 in Figure 7.13, during time t_1 to t_3, there exists only moderate damping, whereas theory predicts heavy damping and therefore an absence of toroidal eigenmodes. At this point in the discharge the density profile is quite flat or even inverted which might modify the mode conversion layer but certainly will not effect fundamental cyclotron absorption. It seems that neither mode conversion nor fundamental absorption is occurring during this time interval. This seems to suggest that hydrogen has not yet diffused into the center of the machine. Charge exchange data confirms that the ratio of hydrogen to deuterium remains constant at 5% throughout most of the discharge. However, no data exists for times earlier than 60 ms, as shown in Figure 7.15. Neutral gas injection experiments indicate that it does indeed take time for hydrogen to reach the center of the plasma. Figure 7.16 shows that when neutral H_2 is injected at 70 ms, it produces charge exchange neutrals with energies of 500 ev and 800 ev, but not 2,500 ev. This indicates that hydrogen has not yet reached the center because 2,500 ev particles basically originate in the plasma center. If it does take a finite amount of time for hydrogen to diffuse into the center of the machine than the important damping processes are second harmonic absorption for $k_{\parallel} = 0.15$ cm^{-1} ($Q_{2\omega_c} = 385$), and Landau damping for $k_{\parallel} = 0.35$ cm^{-1} ($Q_E = 706$). Also note that before time t_2, the plasma is far too cold for second harmonic absorption and Landau damping to occur. This implies that wall loading is probably the most important term, and this results in higher Q modes during the beginning of the plasma discharge.

When $B_T = 49.5$ KG and $N_e = 3 \times 10^{14}$, the ratio of the mode amplitude during resonance to anti-resonance is about 2:1 for the probe P_2 in Figure 7.14. This ratio represents a $Q_{EX} = 555$ for $k_{\parallel} = 0.15$ cm^{-1}, and $Q_{EX} = 223$ for

for $k_{\parallel} = 0.35\ cm^{-1}$. The theoretical values are $Q_T = 802$ for $k_{\parallel} = 0.15\ cm^{-1}$, and $Q_T = 134$ for $k_{\parallel} = 0.35\ cm^{-1}$. As for the high field case, electron damping dominates for large $k_{\parallel}$, but wall loading and electron absorption are comparable for the smaller $k_{\parallel}$. Again, the lower density regime results in similar trends, but with larger values of Q_T.

7.2.2 Hydrogen Plasma ($\omega = 2\omega_{CH}$)

Second harmonic heating of a hydrogen plasma is also receiving a considerable amount of attention in the fusion community. Usually this mode of operation has higher Q values than typical minority regimes; refer to the table below for details of 183.5 MHz operation.

Table 7.2 Theoretical values of Q for various damping mechanisms.
$N = 2.3 \times 10^{14}\ cm^{-3}$

B_T(KG)	$\frac{\omega}{\omega_{CH}}$	$k_{\parallel}(cm^{-1})$	Q_W	Q_E	$Q_{2\omega_c}$	Q_T
39.6	3	0.15	2,610	$>10^7$	--	2,610
		0.35	7,730	486		457
		0.5	18,400	576		559
58.8	2	0.15	2,670	$>10^7$	212	196
		0.35	8,810	1,214	327	250
		0.5	24,400	362	660	232
76.5	1.6	0.15	2,750	$>10^7$	--	2,750
		0.35	10,500	2,480		2,010
		0.5	40,200	1,018		993

For $B_T = 76.5$ KG, the electrons provide most of the damping for $k_{\parallel} = 0.35\ cm^{-1}$ and $k_{\parallel} = 0.5\ cm^{-1}$, while the wall limits the Q for $k_{\parallel} = 0.15\ cm^{-1}$. When $B_T =$ 58.8 KG the resonant layer is in the center of the machine, and for $k_{\parallel} = 0.15\ cm^{-1}$

and $k_{\parallel} = 0.35\ cm^{-1}$ second harmonic damping couples to the ions efficiently. However, for $k_{\parallel} = 0.5\ cm^{-1}$ one would expect more electron heating than ion heating. When $B_T = 39.6$ KG, electrons provide considerable damping for $k_{\parallel} = 0.35\ cm^{-1}$ and $k_{\parallel} = 0.5\ cm^{-1}$. Again, walls dominate the $k_{\parallel} = 0.15\ cm^{-1}$ situation.

7.2.3 Hydrogen Plasma ($\omega = \omega_{CH}$)

Although this particular scheme is not a prime candidate for tokamak heating, it nevertheless provides interesting physics. Consult the table below for details of 90 MHz operation.

Table 7.3 Theoretical values of Q for various damping mechanisms.
$N = 1.5 \times 10^{14}\ cm^{-1}$

B_T(KG)	$\frac{\omega}{\omega_{CH}}$	$k_{\parallel}$	Q_W	Q_E	Q_{ω_c}	Q_{IC}	Q_T
49.5	1.19	0.15	2,020	3,060	--	--	1,220
		0.35	11,800	486			467
58.7	1.00	0.15	2,150	4,080	710	35	33
		0.35	39,000	2,400	130	12	11

For $B_T = 49.5$ KG, the ratio of the mode amplitude during resonance to anti-resonance is typically 9:1 for probe P_2 in Figure 7.20. This ratio represents a $Q_{EX} = 1{,}000$ for $k_{\parallel} = 0.15\ cm^{-1}$, and $Q_{EX} = 388$ for $k_{\parallel} = 0.35\ cm^{-1}$. This agrees very well with the theoretical values, where $Q_T = 1{,}220$ for $k_{\parallel} = 0.15\ cm^{-1}$ and 467 for $k_{\parallel} = 0.35\ cm^{-1}$. Note that large toroidal resonances appear on the radiation resistance as well as on the probe signals. Again, the electrons provide damping for $k_{\parallel} = 0.35\ cm^{-1}$, and both wall losses and

electrons are important for $k_{\parallel} = 0.15\ cm^{-1}$. When $B_T = 58.7$ KG, the fundamental resonance layer lies in the center of the machine, and eigenmodes are not very pronounced on the probe signals or the radiation resistance in Figure 7.21. Some of the modes have a ratio of amplitude during resonance to anti-resonance of about 1.5:1. This corresponds to a $Q_{EX} = 95$ for $k_{\parallel} = 0.15\ cm^{-1}$ and $Q_{EX} = 33$ for $k_{\parallel} = 0.35\ cm^{-1}$. If the ion-ion cyclotron mode conversion is included as a possible absorption mechanism the theory fits reasonably well with the data, $Q_T = 33$ for $k_{\parallel} = 0.15\ cm^{-1}$ and $Q_T = 11$ for $k_{\parallel} = 0.35\ cm^{-1}$. Without the mode conversion, the theoretical Q values are far too large for the experimental data. This indicates that most of the wave energy is converted near the plasma edge, which is detrimental in a heating experiment.

A_2 Antenna (unshielded)

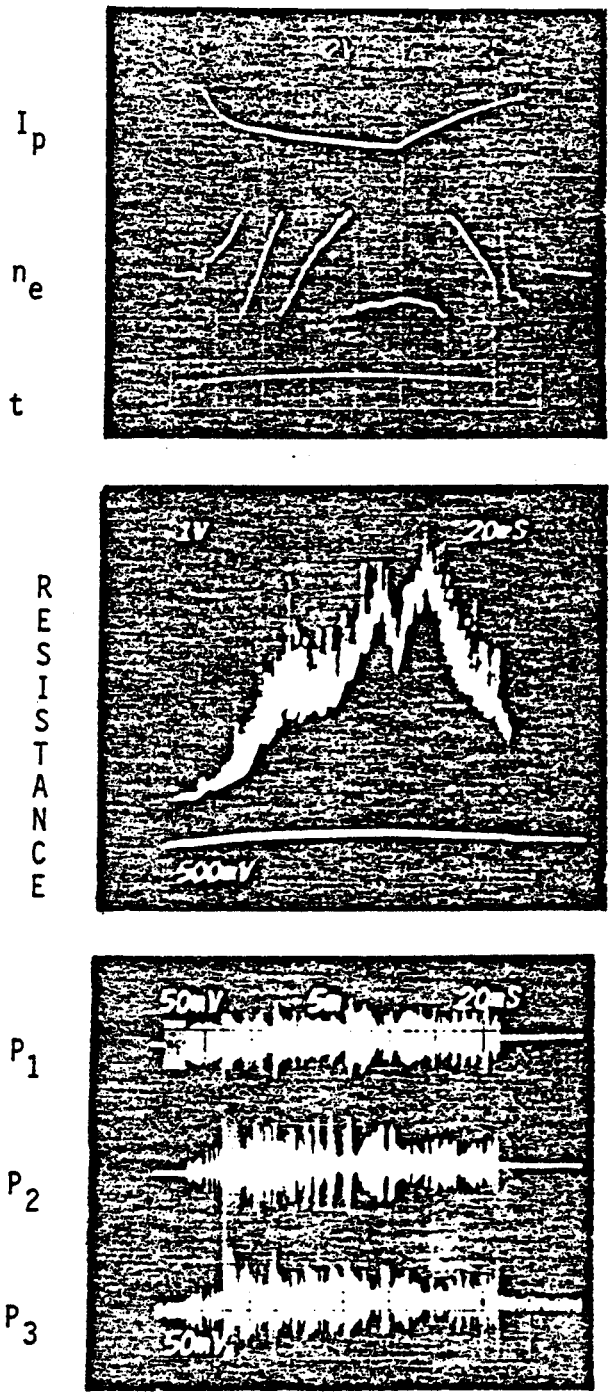

Figure 7.12. Radiation resistance as a function of time for 90 MHz 95%, 5% H and 71.4 KG. Probe P_1 monitors the antenna near zone while P_2 and P_3 monitors the radiation zone.

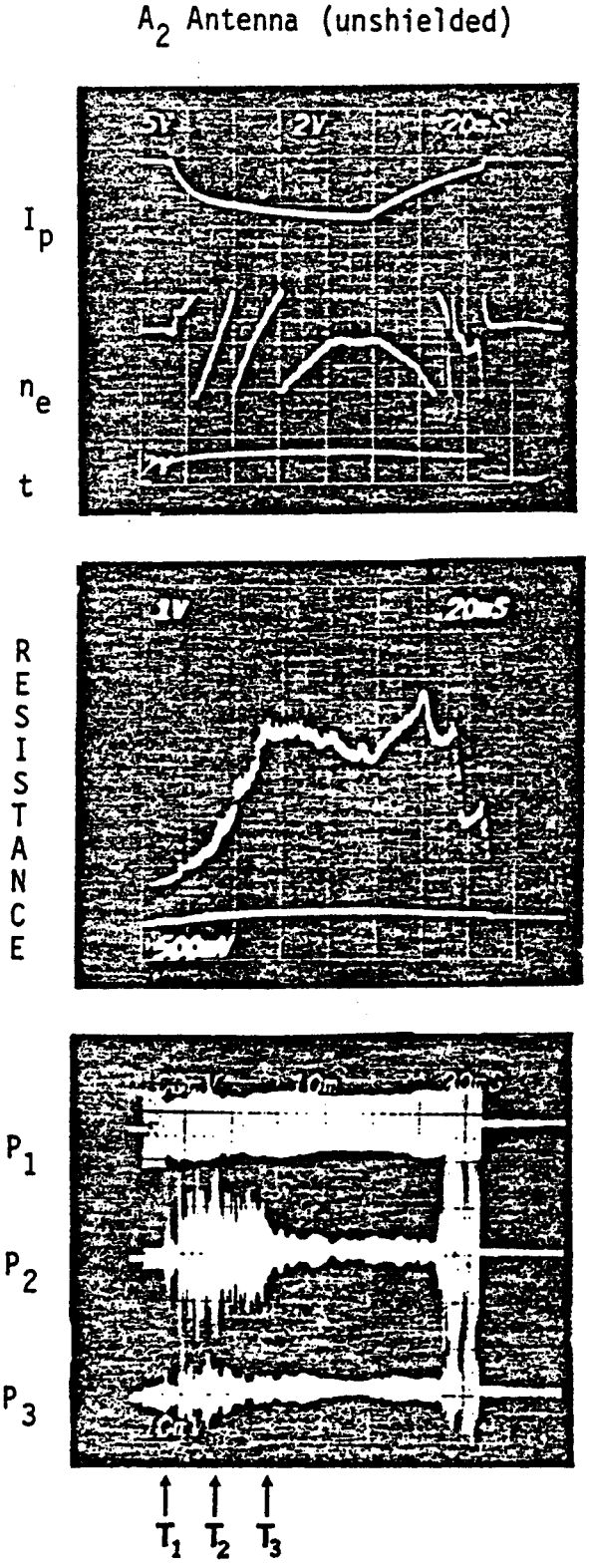

Figure 7.13. Radiation resistance as a function of time for 90 MHz, 95% D, 5% H and 58.6 KG. In this case the resonant layer is centered in the plasma.

A_2 Antenna (unshielded)

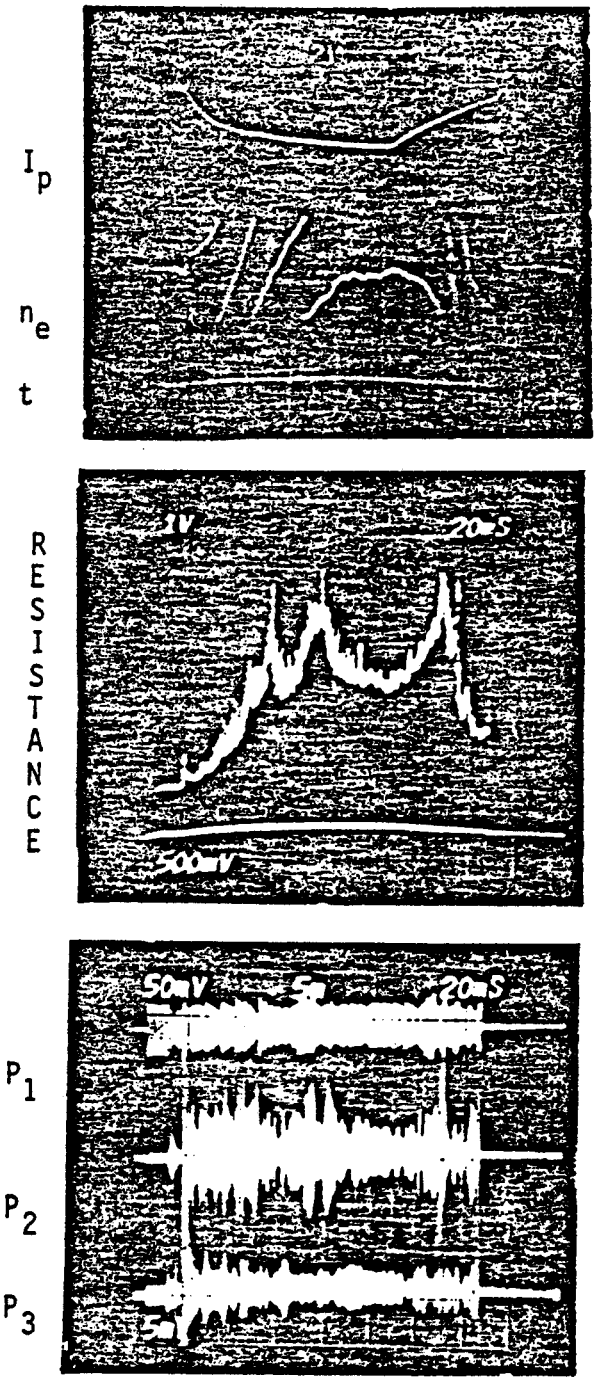

Figure 7.14. Radiation resistance as a function of time for 90 MHz, 95% D, 5% H and 49.5 KG.

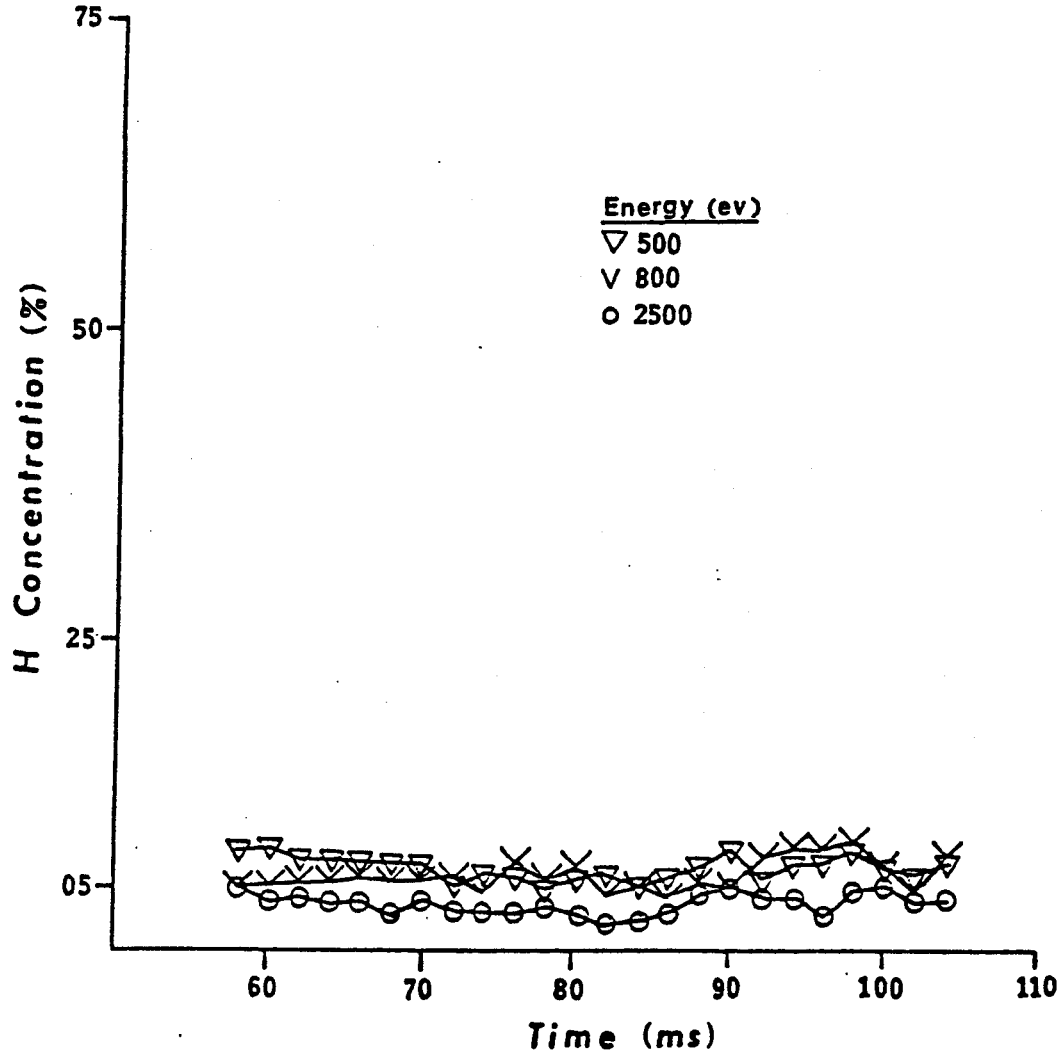

Figure 7.15. Typical charge exchange data of the hydrogen to deuterium concentration ratio when the sole source of the hydrogen is wall retention. [Data courtesy of M.Greenwald.]

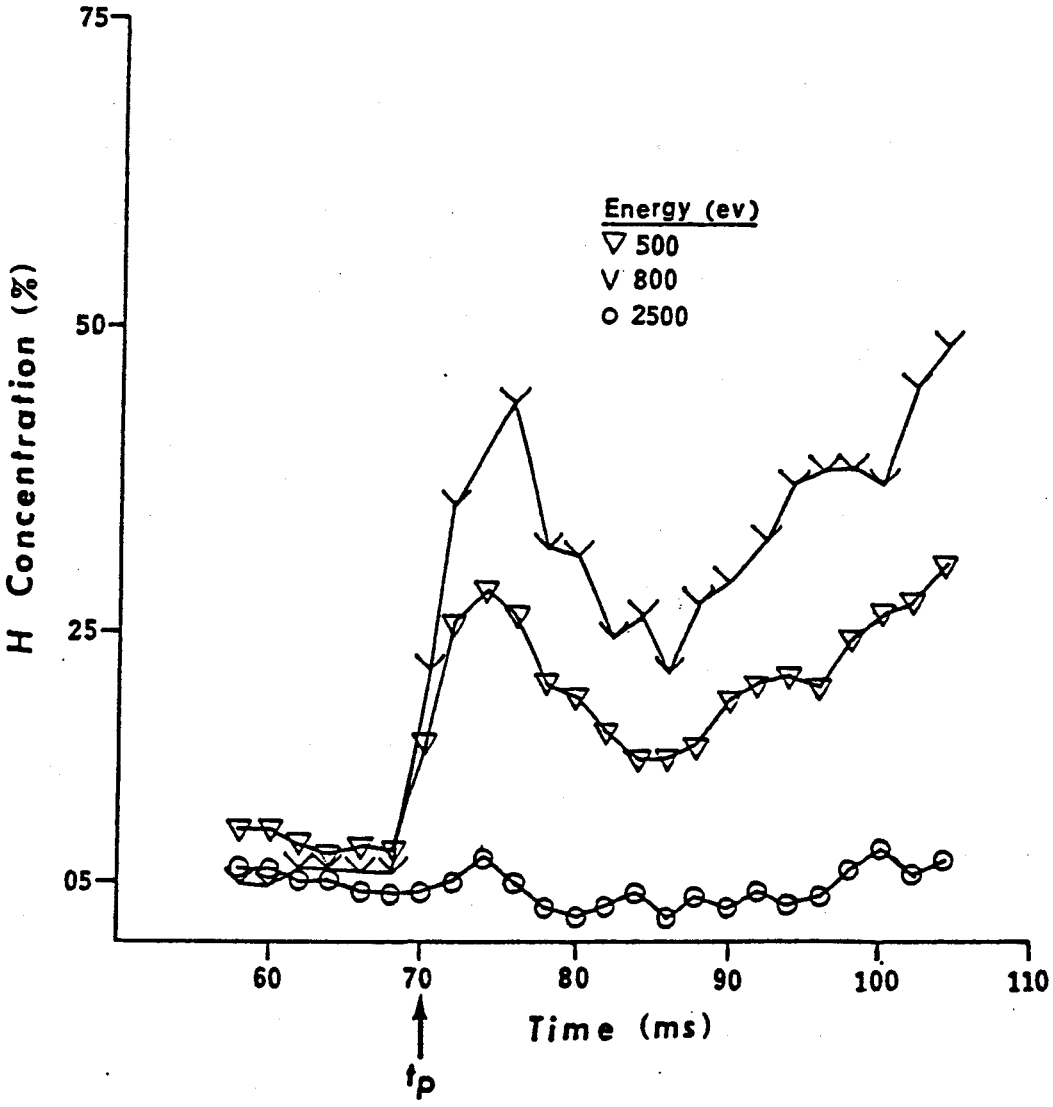

Figure 7.16. Charge exchange signals resulting from neutral hydrogen gas injected in a deuterium plasma at t_p = 70 ms. This experiment is indicative of hydrogen diffusion during the initial stages of a plasma discharge. [Data courtesy of M.Greenwald.]

A_2 Antenna (unshielded)

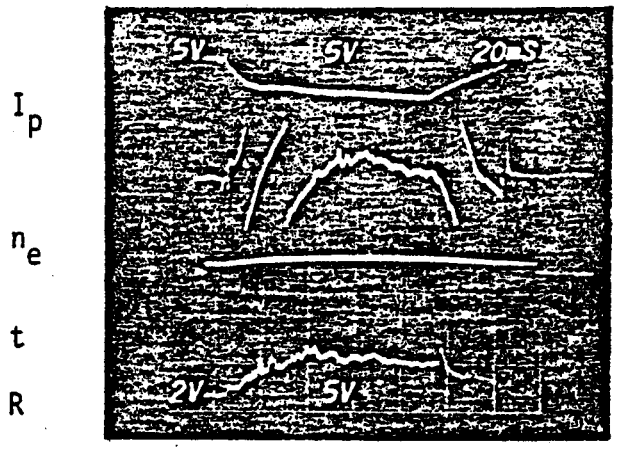

I_p

n_e

t

R

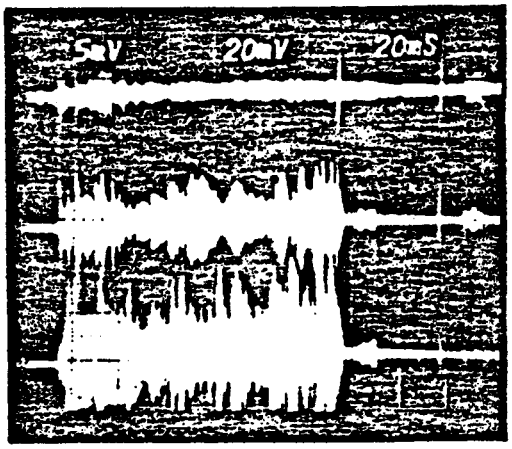

P_1

P_2

P_3

Figure 7.17. Radiation resistance as a function of time for 183.5 MHz, 100% H and 76.5 KG.

A_2 Antenna (unshielded)

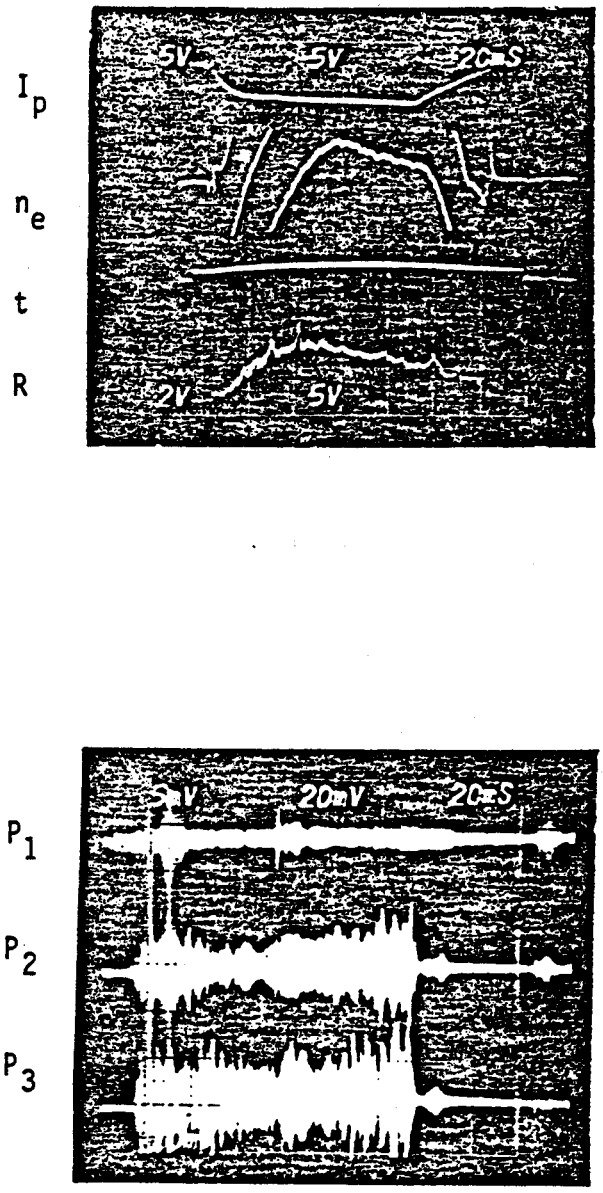

Figure 7.18. Radiation resistance as a function of time for 183.5 MHz, 100% H and 58.8 KG. In this case the resonant layer is centered in the plasma.

A_2 Antenna (unshielded)

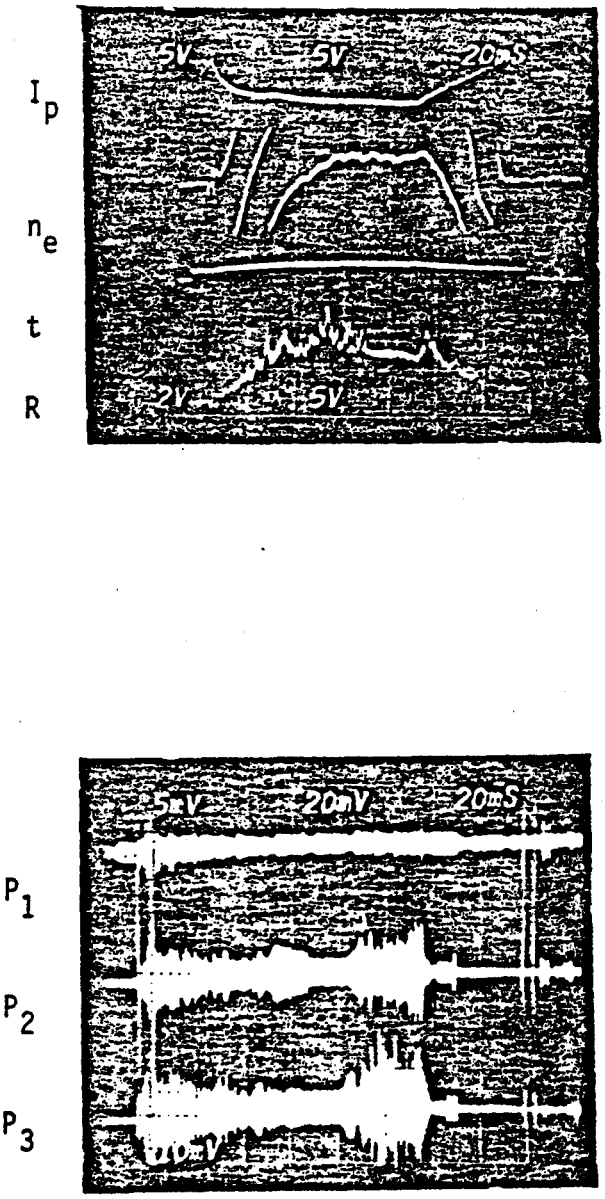

Figure 7.19. Radiation resistance as a function of time for 183.5 MHz, 100% H and 39.6 KG.

A_4 Antenna (shielded)

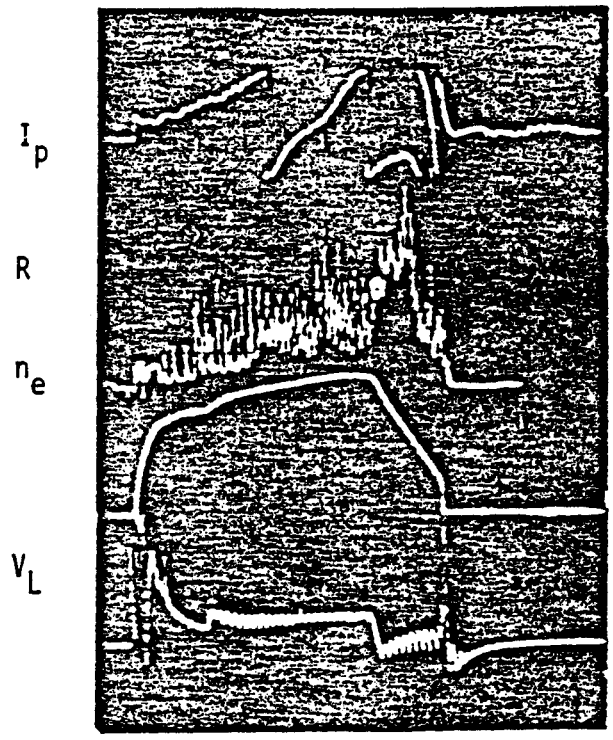

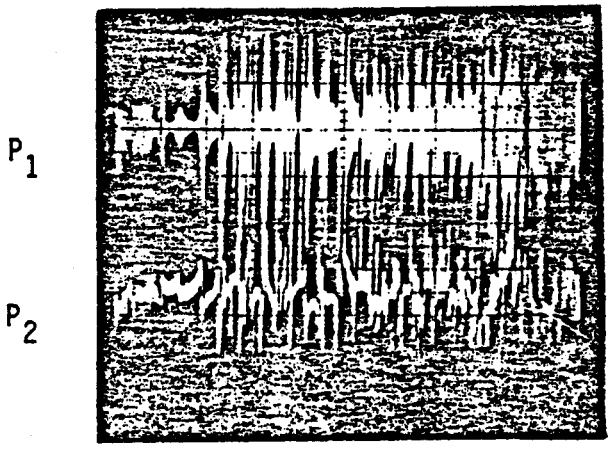

Figure 7.20. Radiation resistance as a function of time for 90 MHz, 100% H and 49.5 KG. P_1 results from the RF envelope of the radiation field while P_2 results from quadrature detection of the signal.

A_4 Antenna (shielded)

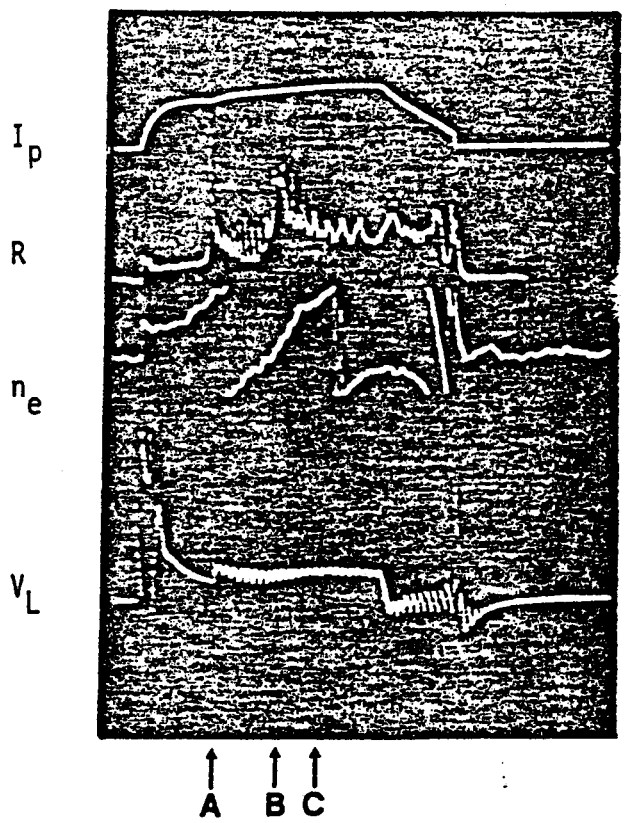

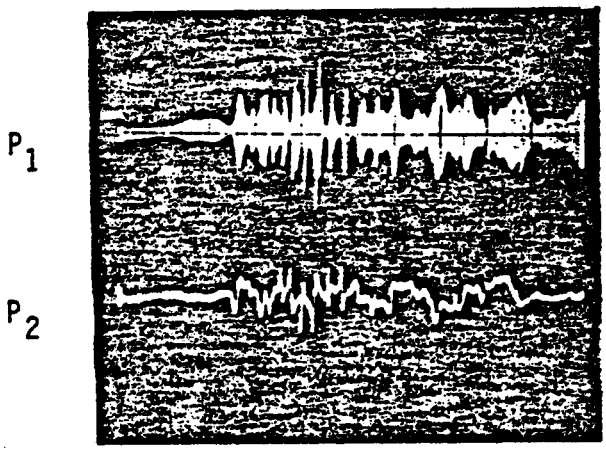

Figure 7.21. Radiation resistance as a function of time for 90 MHz, 100% H, and 58.7 KG. In this case the resonant layer is centered in the plasma.

7.3 Experimental Radiation Resistance

7.3.1 Hydrogen Plasma ($\omega = \omega_{CH}$)

The theoretical results of Chapter 4 can be used to interpret the antenna loading characteristics during the density rise of a plasma discharge. For a hydrogen plasma with a transmitter frequency of 90 MHz the experimental loading agrees reasonably well with the theoretical results. Although the fundamental regime is a poor choice for heating it is ideal for studying wave propagation because there exist good mode separation.

For 58.7 KG and $n_e = 1.5 \times 10^{14}$ cm^{-3} from equation 7.3 $k_i = 6.9 \times 10^{-3}$ cm^{-1} for $k_{\parallel} = 0.15$ cm^{-1} and $k_i = 7.1 \times 10^{-3}$ cm^{-1} for $k_{\parallel} = 0.35$ cm^{-1} using the theoretical values of Q obtained previously.

Figure 7.22 shows the theoretical radiation resistance[14] for the first 2 radial modes when $k_i = 0.007$ cm^{-1}. The value of k_i in this calculation is assumed constant even though it varies significantly for the first few toroidal eigenmodes. In this case $k_{\parallel} \cong 0$ immediately after mode onset and wall loading provides the damping rather than plasma mechanisms. After onset k_i changes slowly and can be assumed constant. In this solution the eigenmode feature is produced by the term $\cos(\beta_i L)/\sin(\beta_i L)$ in equation 4.20. The large onset resistance and the slow decay results from β_i^{-1}. However these plots are a function of density and not β_i. Therefore near cutoff the resistance decays faster than β_i^{-1} since the dispersion relation has a large slope during mode onset. Also the width of the toroidal resonance is broader for large $k_{\parallel}$ because the slope of the dispersion relation decreases as one moves away from onset.

In the experimental radiation resistance in Figure 7.21 peak A is clearly the first propagating mode and after this peak the sharp spikes

results from toroidal eigenmodes. However for this value of k_i there exist some background loading because the antiresonance resistance is not close to zero. Peak B is probably the next radial mode with corresponding toroidal eigenmodes. However after time C it is difficult to ascertain whether the peaks result from new radial or poloidal modes and the analysis is more complex.

For the corresponding values of Q at B_T = 49.5 KG and $n_e = 1.5 \times 10^{14}$ $k_i = 5.6 \times 10^{-4}$ cm^{-1} for $k_{\parallel} = 0.15$ cm^{-1} and $k_i = 5.5 \times 10^{-4}$ cm^{-1} for 0.35 cm^{-1} from equation 7.3.

Figure 7.23 portrays the results for these parameters. For this value of k_i there exists only sharp resonances and no background loading. In this figure the irregular amplitude of the modes spikes result from the finite computational grid and does not result from any physical phenomenon. Qualitatively the experimental data in Figure 7.20 agrees with the result. Figure 7.24 shows what the radiation resistance would look like for k_i = 0.1 cm^{-1}.

It should be noted that these trends are easy to describe theoretically but the exact locations of the mode cut-offs are dependent on plasma profile and not accurately predicted with the flat profile model.

With suitable approximations a realistic formula for calculating radiation resistance can be derived from the results of Chapter 4 if you include a vacuum layer. The vacuum layer will lower $\bar{E}$ at the antenna because of edge evanescence but the integral of $\varepsilon_{\perp}^{*} \cdot \varepsilon_{\perp}$ will be approximately the same. By using appropriate boundary conditions and exponential rather than modified Bessel functions Paoloni[16] has derived the radiation resistance with a vacuum layer as:

7.7 $$R' = \frac{Q\omega_0\mu_0}{\ell_T} \frac{\Delta^2 e^{-k_\parallel(2\delta-\Delta)}}{\left[\frac{1}{2k_\perp^2}\left(\frac{k_A^2}{(1+\Omega)^2}+k_\parallel^2\right)\left(\frac{1}{k_\parallel A}+1\right)^2+1\right]} \qquad (7.7)$$

For m = 0 $R = 2\pi R'$

For m = 1 $R = \frac{8}{\pi} R'$

Where δ = thickness of vacuum layer

Δ = distance between antenna center conductor and the wall.

When the A_4 antenna is used the radiation resistance calculated from equation 7.7 must be divided by four in order to account for the faraday shield suppressing the antenna flux. For a hydrogen plasma at $n_e = 1.5 \times 10^{14}$ cm^{-3} and 90 MHz the radiation resistance is listed in the table below.

Table 7.4 Radiation resistance.

B_T (KG)	$k_\parallel$ (cm^{-1})	Q	$R_{m=0}$ (Ω)	$R_{m=1}$ (Ω)	R_{EXP} (Ω)
58.7	0.15	33	1.3	0.5	0 → 0.5
	0.35	11	0.0	0.0	
49.5	0.15	1,220	26	11	0 → 15
	0.35	467	1.6	0.6	

The theoretical calculations, both qualitatively and quanitatively agree with the experimental results within the spirit of the calculation.

7.3.2 Deuterium and Hydrogen Minority Plasma ($\omega = 2\omega_{CD}, \omega_{CH}$)

The radiation resistance is listed in the table below for the minoirty regime at $n_e = 1.5 \times 10^{14}$. These results are for 95% deuterium and 5% hydrogen minority plasma at 90 MHz with the unshielded A_2 antenna.

Table 7.5 Radiation resistance.

B_T (KG)	$k_{\parallel}$ (cm^{-1})	Q	$R_{m=0}$ (Ω)	$R_{m=1}$ (Ω)	R_{EXP} (Ω)
58.6	0.15	5	0.31	0.13	1.5
	0.35	5	0.12	0.05	
71.4	0.15	1,630	95.4	38.6	1.0 → 1.5
	0.35	3,730	8.7	3.5	

These results are very interesting and indicate possible problems in coupling to the fast compressional Alfren wave. For B_T = 58.6 KG the theoretical radiation resistance is much smaller than the experimental results while for B_T = 71.4 KG the theoretical results are far too large. According to the radiation resistance in Figure 7.13 there seems to be a background loading which is proportional to density but roughly independent of wave damping mechanisms as a result of varying the toroidal magnetic field. Both the low and high field data shows eigenmode structure on the resistance but it is less than 25% of the background. However, according to the computer solutions even if there is sufficient mode stacking the background should not be independent on the damping length. For low Q modes a background resistance can occur if there exists a large number of propagating modes. On the other hand for high Q modes the sharp resonance feature and the small resistance of the anti-resonance point prevents a large background from occurring. If one assumes that the background loading is caused by parasitic losses not associated with the fast wave then the dilemma seems resolved. The equivalent antenna circuit with parasitic loses is shown on the next page.

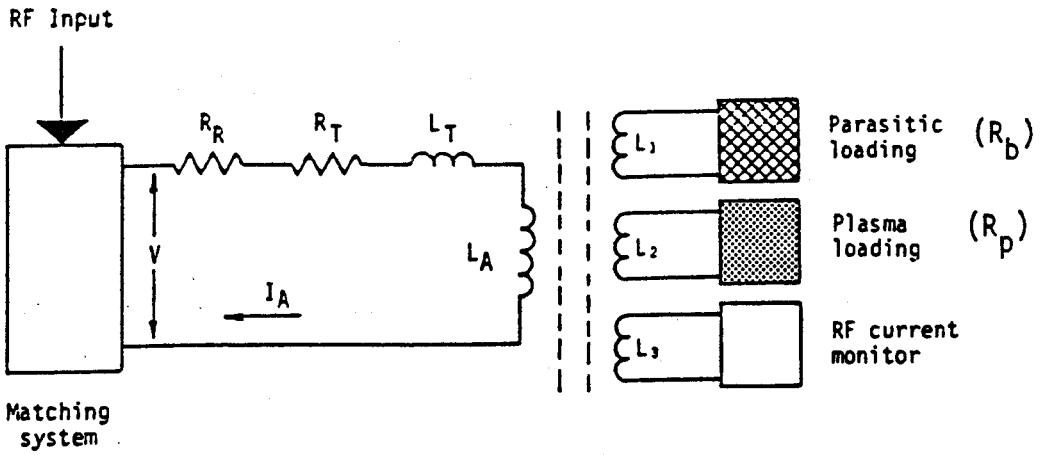

Although the loading (R_p) from the fast compressional Alfven wave exhibits a wide range of values its effect on the overall resistance is small as a result of the mutual coupling between L_1 and L_2. This coupling loads down the circuit for large values of R_p, and as a result the wave field only produces small fluctuations of the background component (R_b). This effect is indicative of the experimental data and provides strong evidence for the equivalent circuit model. If this indeed happens, then R_b will absorb a significant amount of power and the heating efficiency will be extremely poor. It should also be noted that this same background loading has been observed for second harmonic regime in a hydrogen plasma.

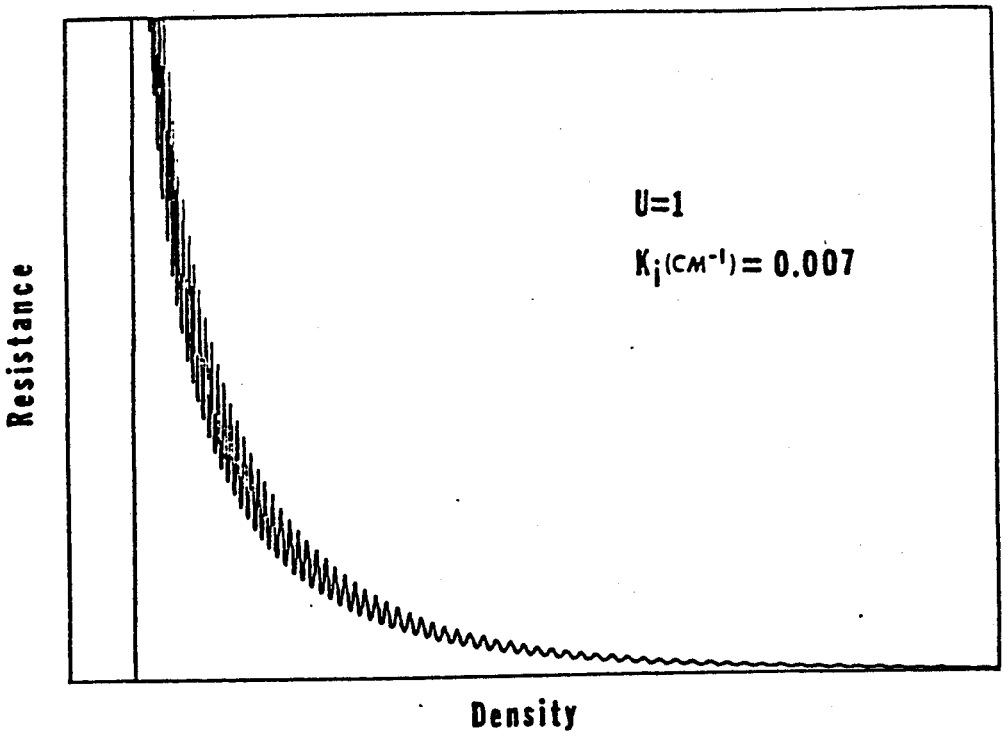

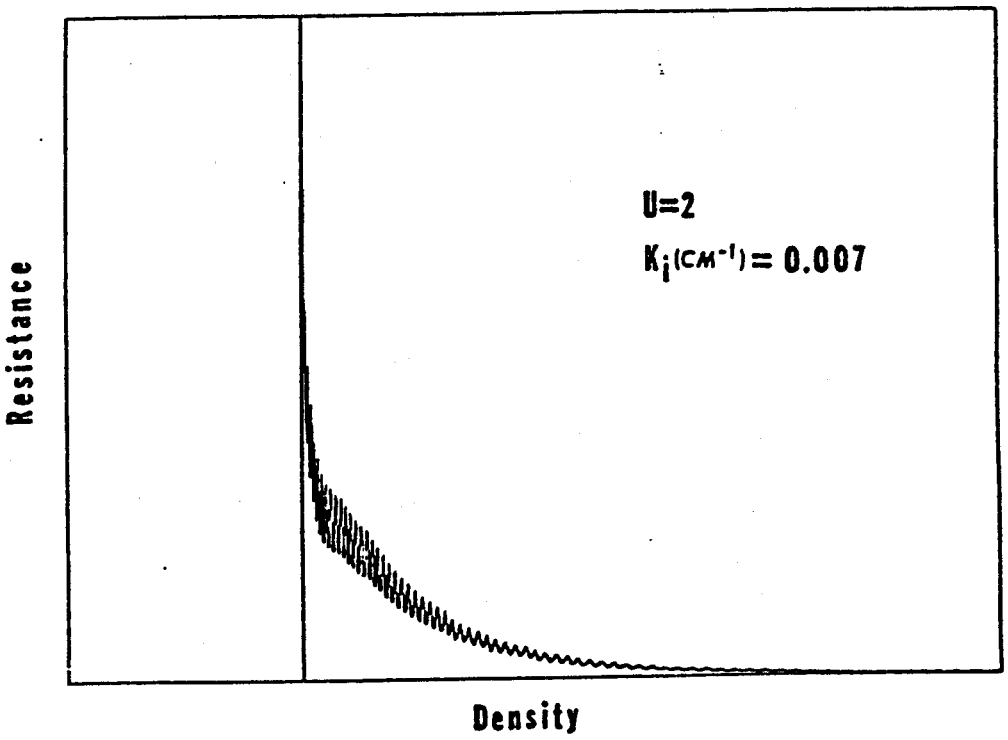

Figure 7.22. Computer solutions of the radiation resistance for the first two radial modes when k_i = 0.007 cm^{-1}.

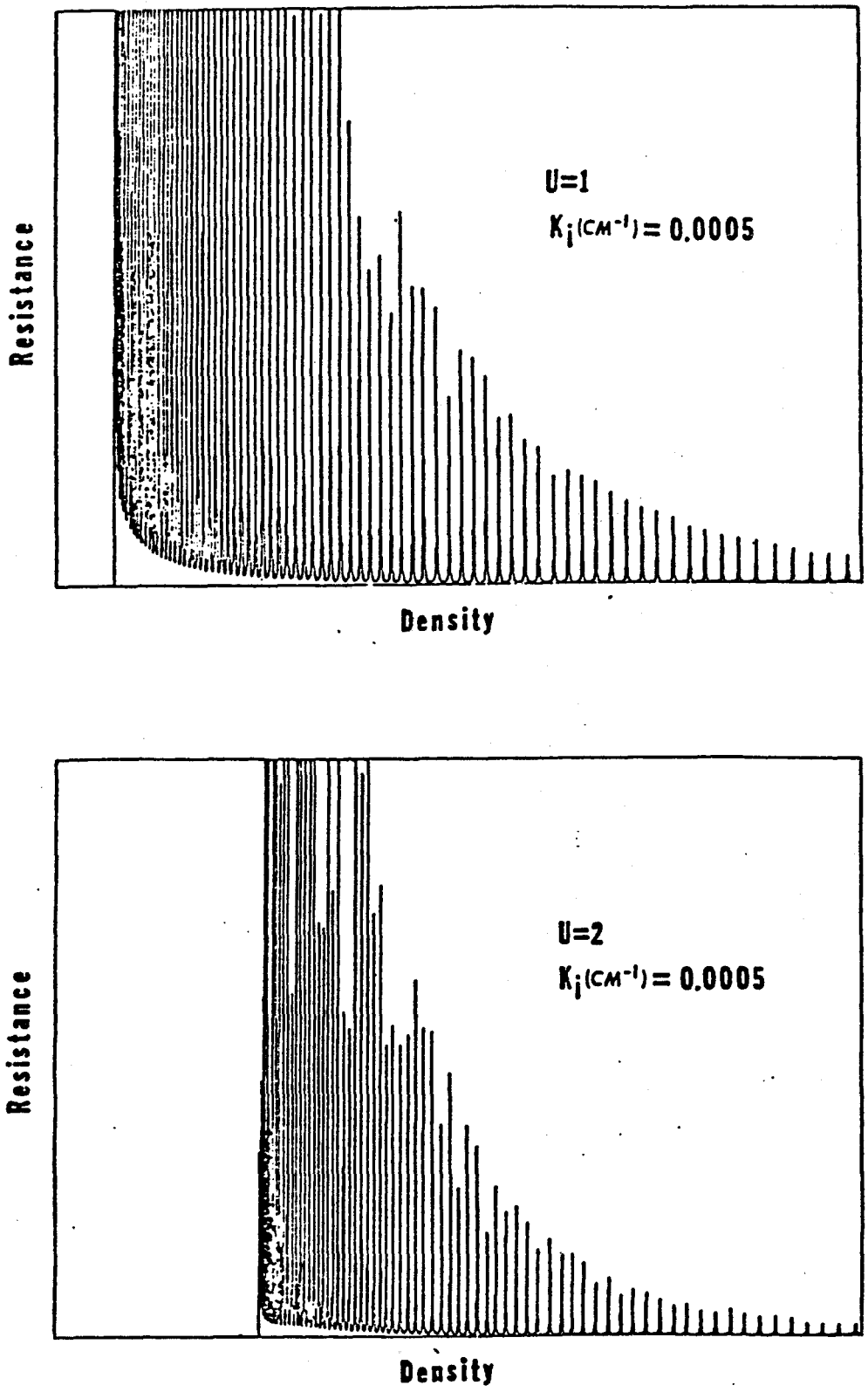

Figure 7.23. Computer solutions of the radiation resistance for the first two radial modes when $k_i = 0.0005\ cm^{-1}$.

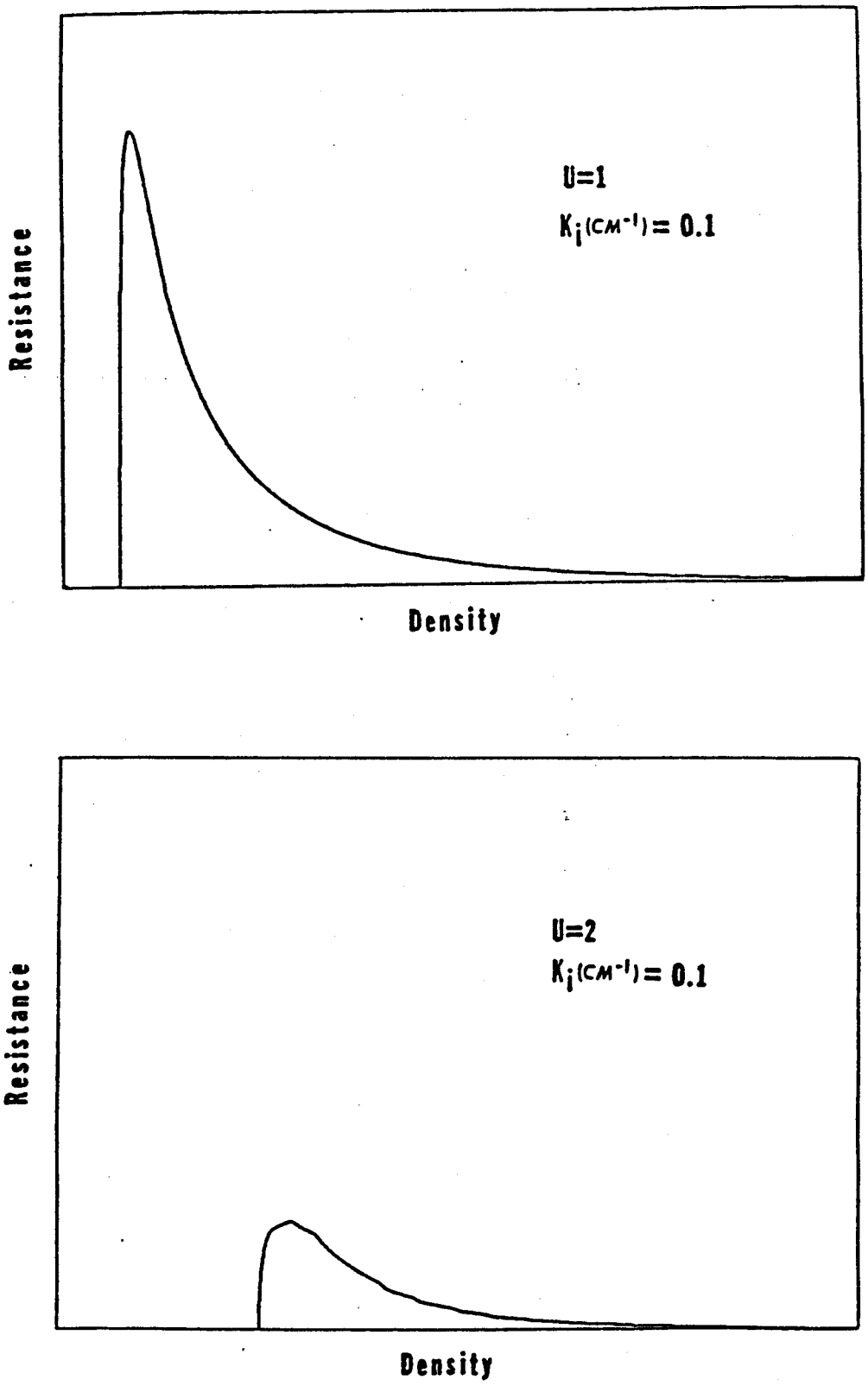

Figure 7.24. Computer solutions of the radiation resistance for the first two radial modes when k_i = 0.1 cm^{-1}.

7.4 Parasitic Near Field Loading

One important difference between the Alcator A experiment and others performed throughout the world is the rather small distance between the antenna and the plasma. In the A_4 antenna configuration there exist 0.5 cm between the faraday shield and the limiter radius. Although the antenna is well shielded, it still resides near a relatively cold dense plasma compared to other tokamaks. For example, in PLT the plasma density in the proximity of the faraday shield is between 10^{10} - 10^{11} cm^{-3}. In comparison, the edge density[15] for Alcator A is on the order of 10^{13} cm^{-3}.

Near the faraday shield in Alcator A the wave physics is very complex as a result of the collisionality and gradient of the plasma density. This narrow region has little effect on the TE component of the fast magnetosonic wave because of the small value of $k_\perp$. However, it is conceivable that antenna near-fields can launch electrostatic or electromagnetic waves of short wave lengths which could result in parasitic loading.

I propose that the parasitic loading results from the collisional absorption of the antenna near field evanescing into the plasma. This is basically a form of skin effect. In order to formulate scaling laws for this collisional absorption process, we must understand how the field evanesces into the plasma.

H_z and E_z are relatively independent near the plasma edge because $K_x \to 0$ in the dielectric tensor. The slow wave or E_z branch can be evanescent in this region and under certain circumstances this wave decays away before it reaches the region where H_z and E_z are strongly coupled. This implies that this E_z solution can be treated independently of the fast magnetosonic mode. It should be noted that the fast magnetosonic wave has a small value

of E_z near the edge because of the high conductivity of the plasma center and is not of interest in this problem. Therefore for $\omega > \omega_{ci}$ the slow wave can be used to predict the width of the evanescent zone:

$$k_{\parallel}^2 + \frac{1}{2} k_{\perp}^2 = \frac{\omega^2}{V_A^2[1 - (\omega/\omega_c)]} \tag{7.8}$$

At this point it should be mentioned that the near fields arise because the radiation fields cannot satisfy the boundary conditions of a metal antenna. In Chapter 4 we treated the antenna as a current filament and ignored the fact that the electric field must vanish at the antenna. In order to satisfy the boundary conditions at the antenna $k_{\parallel}$ can range from 0 to ∞ in Equation 7.8. The imaginary part of $k_{\parallel}$ is extremely important in this problem and $k_{\parallel} = k_r + jk_i$. For $k_r > k_i$, Equation 7.8 indicates $k_{\perp}$ will be large and therefore the field will not evanesce into the plasma, implying that k_i will be small. However when $k_r < k_i$, the field can penetrate into the plasma and resistive losses will occur. For $k_i \sim k_{\perp}$, Equation 7.8 reduces to:

$$\frac{1}{\delta^2} = \frac{\omega^2}{2V_A^2[(\omega/\omega_c) - 1]} \quad \text{where} \quad \delta = \frac{1}{k_i} \tag{7.9}$$

This produces a field solution of the following form:

$$E_z \propto e^{-xk_i} e^{z[jk_r - k_i]} \tag{7.10}$$

where x is the direction perpendicular to the magnetic field.
The power absorbed by the plasma is:

$$P = \mathrm{Re} \iiint j_z E_z^* \, dx^3 \tag{7.11}$$

In order to find a relation between j_z and E_z, consider the z component of

the following fluid equation with electron-ion collision terms:

$$mn\frac{dV_z}{dt} = enE_z - mn\nu_{ei}V_z$$

Assuming all the current is carried by the electrons:

$$j_z = neV_z = \frac{ne^2E_z(\nu_{ei} - j\omega)}{m_e(\omega^2 + \nu_{ei}^2)} \tag{7.12}$$

Using Equation 7.11 and 7.12 yields the power absorbed by the plasma:

$$P = \frac{ne^2E_z^2\nu_{ei}\delta^2\ell}{2m_e(\omega^2 + \nu_{ei}^2)} \tag{7.13}$$

Without a faraday shield, E_z is very large and proportional to the antenna current. With a faraday shield, E_z is produced by stray antenna fields and by toroidal transform effects on E_ϕ. E_z can therefore be related to the loading resistance as follows:

$$E_z = \Psi E_\phi \tag{7.14}$$

$$E_\phi = \frac{V}{\ell} = \frac{\omega L I}{\ell}$$

where ℓ is the length of the antenna and L is the inductance.

$$P = I^2R$$

$$R \propto \frac{P\omega^2L^2}{E_z^2\ell^2}\Psi^2$$

Substitution of Equation 7.13 yields:

$$R \propto \Psi^2 \frac{L^2 e^2}{\ell} \left[\frac{n \nu_{ei} \delta^2}{m_e [1 + (\nu_{ei}^2/\omega^2)]} \right] \tag{7.15}$$

For $\nu_{ei}^2/\omega^2 << 1$ and $\nu_{ei} = 1.5 \times 10^{-6}\ n \ln\Lambda / T^{3/2}$ where T is in eV:

$$R \propto \Psi^2 \frac{L^2 e^2 n^2 \ln\Lambda}{\ell m_e T^{3/2}}\ \delta^2$$

Using Equation 7.9, the loading resistance now scales as:

$$R \propto \left[\frac{L^2 e^2 \ln\Lambda}{\ell m_e m_i T^{3/2}} \right] \Psi^2 B_T^2\ \frac{n}{\omega} \left(\frac{\omega}{\omega_c} - 1 \right) \tag{7.16}$$

It is difficult to calculate the magnitude of the parasitic loading since the value of E_z produced by the antenna for a realistic geometry is not accurately known. However, for certain parameters the scaling of Equation 7.16 is extremely good which provides some justification of the model. Listed below are some of the interesting points of the parasitic loading model.

1. Equation 7.16 scales linearly with density. For hydrogen at $\omega = 2\omega_{ci}$ and deuterium at $\omega = 2\omega_{ci}$, $4\omega_{ci}$ the experimental background loading is also linearly dependent on density. See Figure 7.25 for details.

2. The experimental ratio of loading for a hydrogen plasma at 200 MHz ($\omega = \omega_{2H}$) to a deuterium plasma at 200 MHz ($\omega = \omega_{4D}$) is 1.5. The model predicts the ratio to be 1.6.

3. When $\omega \leq \omega_{ci}$ the slow wave is no longer evanescent and the background loading will not exist according to the proposed model. For a

deuterium plasma the transmitter frequency was lowered to 58 MHz, and as a result of this the background loading disappeared. For this regime only eigenmode loading existed and the experimental radiation resistance is shown in Figure 7.26.

4. For a hydrogen plasma at 90 MHz ($\omega = \omega_{CH}$) the experimental background loading is zero. The model also predicts zero loading for this case.

5. A faraday shield helps suppress the E_z component of the near field and reduce the level of parasitic loading. This implies that the ratio of eigenmode loading to parasitic loading should be larger for an antenna with a faraday shield. This theory is supported with the experimental data provided by A_2 and A_4 antenna configuration. See Figure 7.26 for details.

6. The scaling of Equation 7.16 with toroidal magnetic field for antennas A_2 and A_4 is extremely interesting. When a faraday shield is not used E_z is directly proportional to the near field which is related to the antenna current. This implies that Ψ in Equation 7.14 is not a function of the toroidal magnetic field, and in this case Equation 7.16 scales with B_T as follows:

$$B_T^2 \left(\frac{\Omega B_o}{B_T} - 1 \right) \qquad (7.17)$$

where $\omega = \Omega \left(\frac{eB_o}{mc} \right)$

The experimental background loading for various values of magnetic field is shown in Figure 7.27. In this figure, the dotted line is a plot of Equation 7.17 which has been normalized to the middle of the error bar at 60 KG.

When a faraday shield is used, the E_z component of the near field is shorted out. However, the toroidal transform of E_ϕ will produce an effective

E_z component. In this case, $\Psi \propto B_T^{-1}$ in Equation 7.14. Now Equation 7.16 scales with toroidal magnetic field as follows:

$$\left(\frac{\Omega B_o}{B_T} - 1\right) \tag{7.18}$$

Figure 7.27 shows the experimental background loading for the A_4 antenna where the dotted line is a plot of Equation 7.18.

7. The plasma current in a tokamak is constantly increasing during the density rise of a typical discharge. This changes the toroidal transform which means that the background loading does not simply scale as "n". When B_T is constant $\Psi \propto I_p$ and Equation 7.16 scales with density and plasma current as follows:

$$\left(nI_p^2\right) \tag{7.19}$$

In Figure 7.28 the experimental background loading for a hydrogen plasma with the A_4 antenna at 200 MHz is R_b. The dotted line in the figure represents a plot of Equation 7.19 (I_p was obtained from the experimental data). In this figure the background loading R_b is plotted to scale with the eigenmode component R_p, however the probe voltage V_p has been normalized to R_p at low density. It should be noted that wave damping increases for the high density regime and therefore R_p and V_p tend to decrease. In this figure R_p and V_p follow the same trends with density but R_b's dependance is quite different. This implies that R_b is produced by mechanisms not associated with the fast compressional Alfven wave.

8. The experimental background loading has no observable density cutoff. Since the parasitic model does not form radial eigenmodes it will also not have a density cutoff.

9. During the period of high power RF pulse we have observed H_α light, as shown in Figure 7.25. This is significant, because H_α light originates from the edge plasma, where the temperature is about 5 eV. This implies the presence of a large E_z field near the edge, which probably results from the antenna near fields.

The general predictions of this model are quite interesting and certainly require additional attention. They also suggest that the antenna be kept a suitable distance from the plasma surface in order to reduce parasitic loading and improve heating efficiencies.

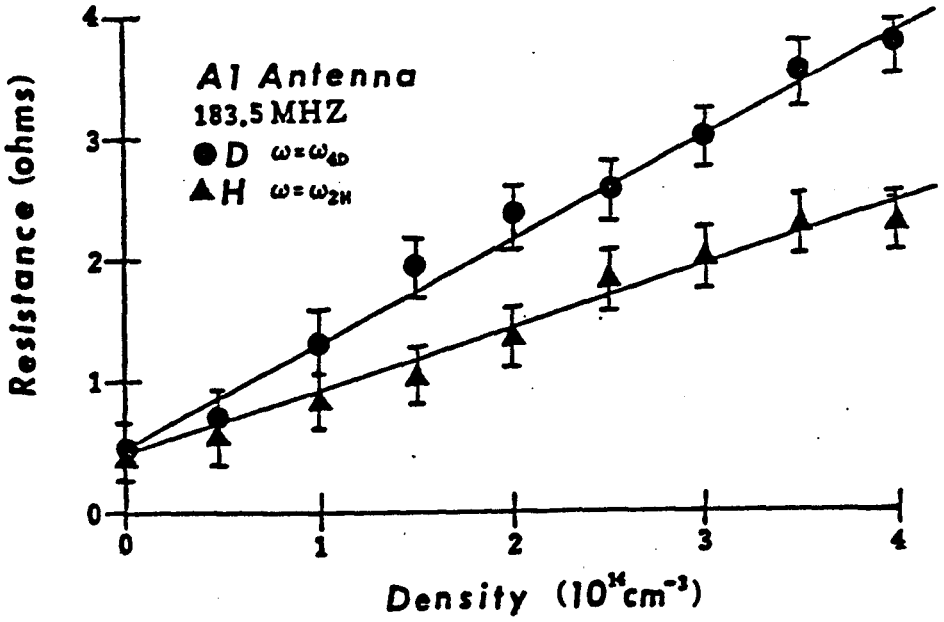

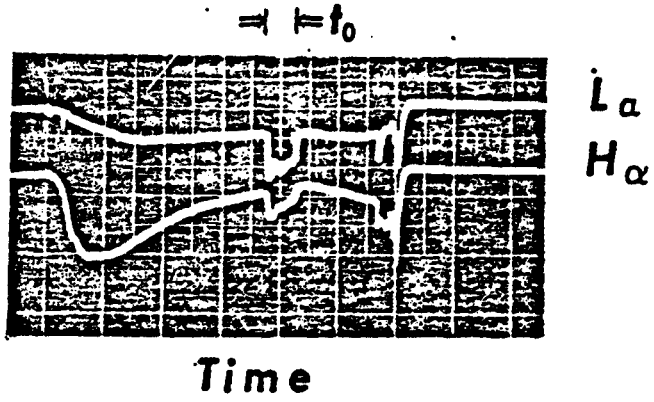

Figure 7.25. Graph of radiation resistance as a function of density for the A_1 antenna. The offset of 0.5 Ω is due to ohmic loses in the antenna structure. Also shown is photographs of the total light (L_A) and H_α light near the antenna as a function of time. Observe the increase in L_A, H_α during the time of the RF pulse (t_o).

A_2 Antenna (unshielded)

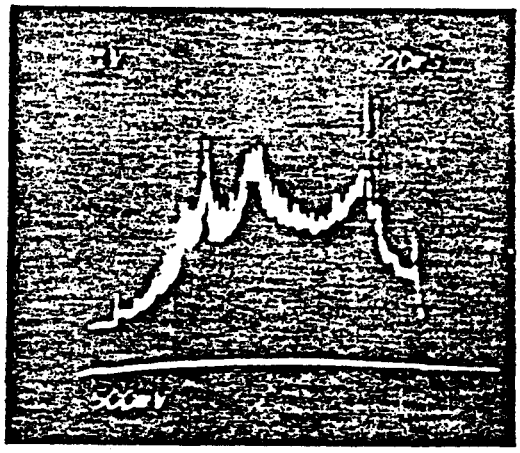

RESISTANCE

90 MHz
95% D, 5% H
50 KG

A_4 Antenna (shielded)

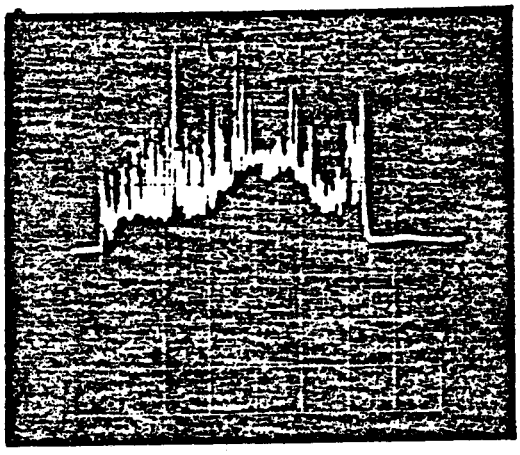

RESISTANCE

90 MHz
95% D, 5% H
50 KG

A_4 Antenna (shielded)

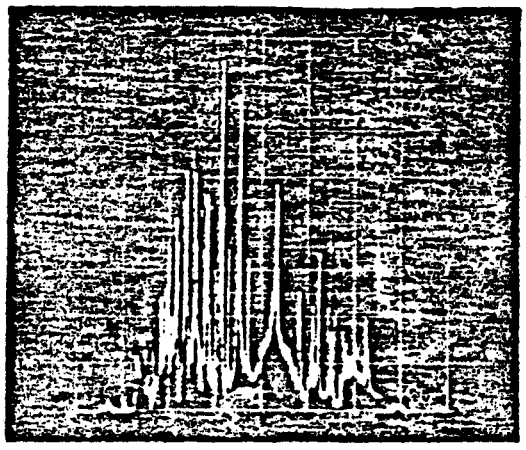

RESISTANCE

58 MHz
95% D, 5% H
58 KG

Figure 7.26. Radiation resistance as a function of time for three different cases. Note ratio of background loading to eigenmode component.

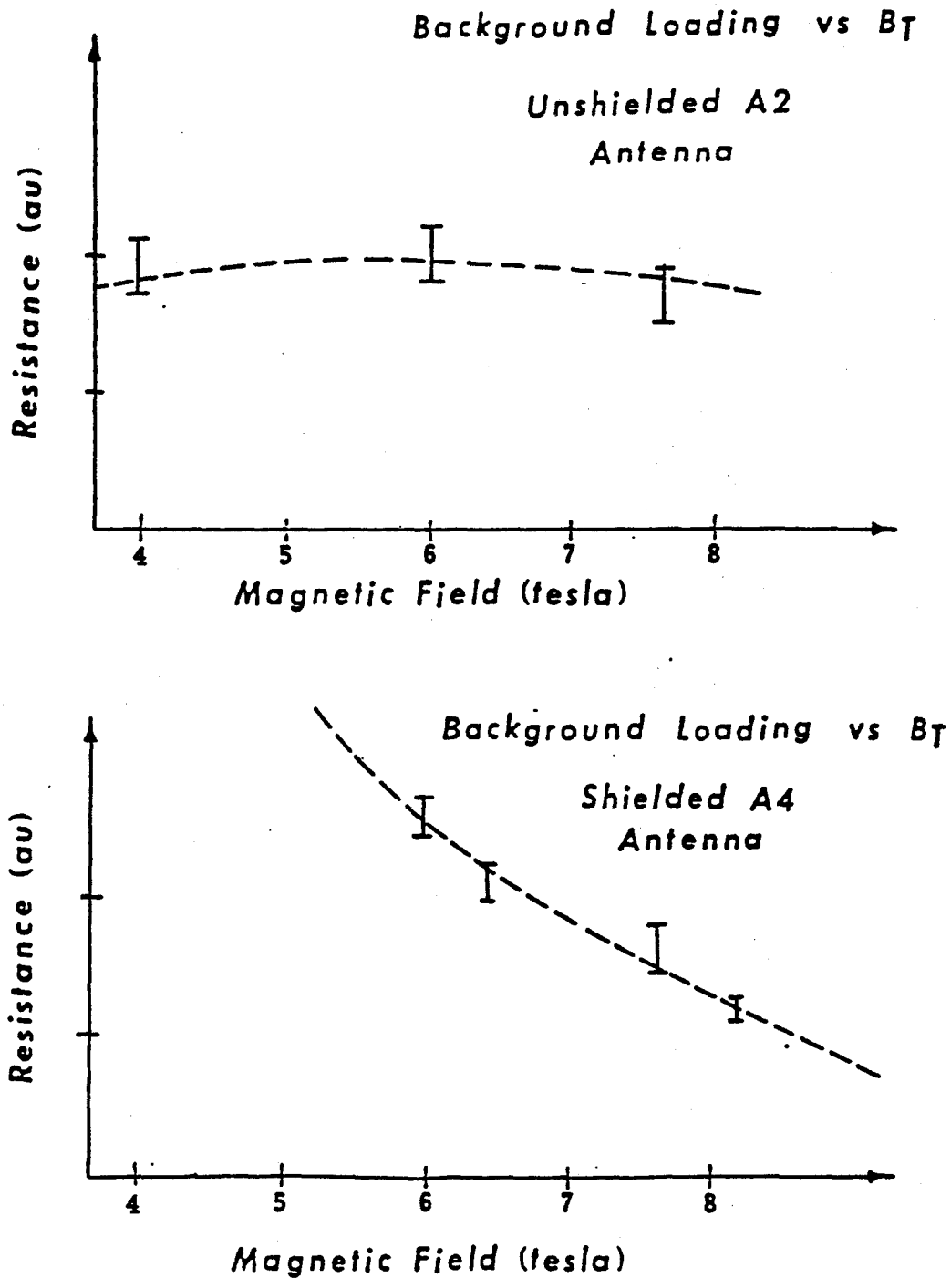

Figure 7.27. Background loading as a function of the toroidal magnetic field for shielded and unshielded antennas. The dotted lines represent the scaling of equations 7.17 and 7.18 normalized for best fit for constant I_p and n_e.

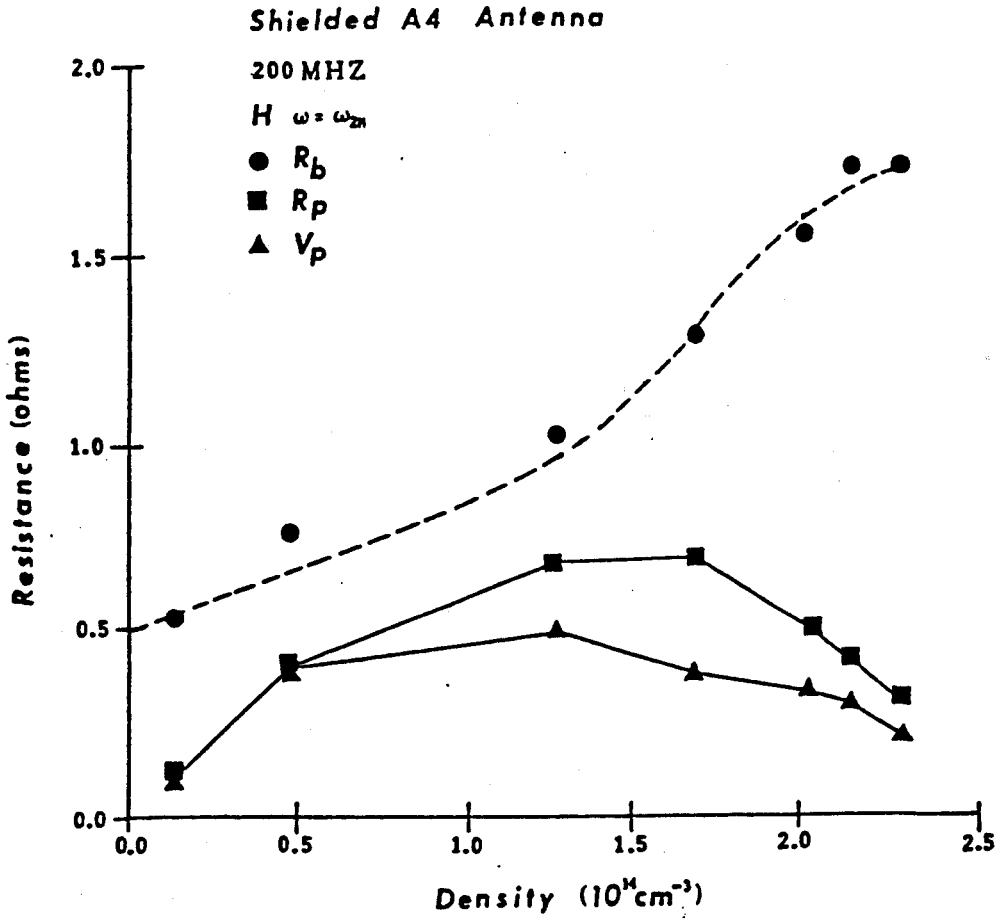

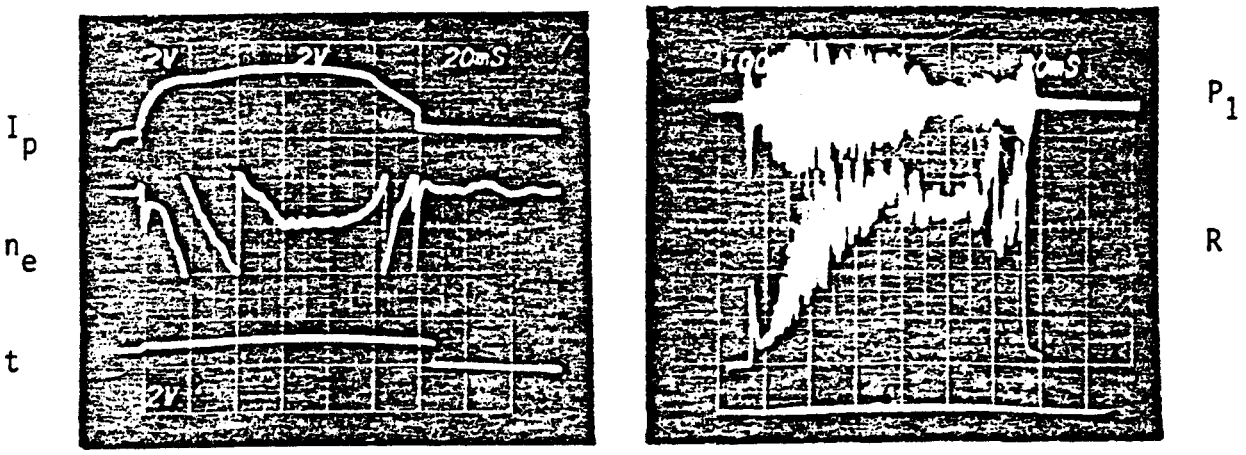

Figure 7.28. In the graph above R_b is the experimental background loading, R_p is the experimental fast wave loading and V_p is a typical RF probe signal. The dotted line in the graph represents a plot of Equation 7.19 normalized for best fit. These experimental results were obtained from the pictures above.

8. CONCLUSIONS

In this experiment, we have discovered a number of major problems in coupling to the fast compressional Alfven-wave. As a result of the stringent mechanical constraints of Alcator A, key antenna dimensions are far too small for efficient coupling. In order to overcome these problems and increase the radiation resistance, high Q eigenmodes must be excited. In general this is not a satisfactory mode of operation because these eigenmodes are difficult to maintain in toroidal resonance. For low Q modes, the impedance can be maximized by operating near mode onset. The radiation resistance in this regime is still small but should provide reasonable coupling. However, the proximity between the plasma and the antenna seems to favor coupling to a parasitic mode excited by the antenna near field, and in light of the small fast wave impedance for harmonic ion cyclotron absorption the bulk heating efficiencies are degraded. Only wave propagation near the fundamental cyclotron frequency is unaffected by this parasitic background loading. Unfortunately, this fundamental regime is not suitable for tokamak heating because most of the power will be deposited in the ion-cyclotron mode conversion layer near the plasma surface.

The probe signals for all experiments agreed very well with the theories for the propagation and damping of the fast wave. By varying the toroidal magnetic field, it was possible to vary the Q of these waves over a considerable range and isolate some of the basic absorption mechanisms. When applicable, pure second harmonic damping, minority absorption, ion-ion hybrid resonance, electron Landau damping, wall loading, pure fundamental absorption, and ion-cyclotron mode conversion have been observed.

APPENDIX I. MIXERS

Mixers are three-port nonlinear networks which translate signals at one frequency into those of another frequency. The two basic types of mixers using diodes in a nonlinear mode are single-balanced and double-balanced configurations.

A.I.1 Single-Balanced Mixers

See Figure A.I.1 for a typical mixer configuration. The most significant characteristic of the single-balanced mixer is the isolation between the local oscillator port (LO) and the RF input port (RF). In this case the loop currents i_{LO_1} and i_{LO_2} in Figure A.I.1. cancel at the RF port. Unfortunately, there exists poor isolation between the RF port and the IF port which degrades the operation of the mixer. The poor isolation results from the fact that the loop currents i_{RF_1} and i_{RF_2} add at the IF port.

A.I.2 Double-Balanced Mixers

A typical shematic for a double-balanced mixer is shown in Figure A.I.2. This type of mixer is preferred over the single-balanced configuration because it offers better isolation between all the ports. In Figure A.I.2 if CR_1, CR_2 and the LO transformer are symmetrical, then the voltage at point A is zero when a signal is applied at LO. If the characteristics of CR_3 is equal to CR_4 then the voltage at B is also zero. Therefore there exists no voltage across A and B and as a result the voltage across the RF or IF port is zero. If CR_4 is equal to CR_1 and CR_2 is equal to CR_3, then the voltage at C and D will also be zero. Thus there exists no RF leakage at the IF port or LO port for an ideal double-balanced mixer.

The IF output of a standard double-balanced mixer is:

$$\text{IF output} = B_1 \cos [(\omega_{LO} - \omega_{RF})t - (\phi_{LO} - \phi_{RF})]$$

$$+ B_2 \cos [(\omega_{LO} + \omega_{RF})t - (\phi_{LO} + \phi_{RF})]$$

$$+ [\text{higher order frequency terms}]$$

In general, B_1 and B_2 are related to the RF input signal times the amplitude of the local signal. If the local input is sufficiently high, B_1 and B_2 will be proportional only to the amplitude of the RF input signal because of diode saturation characteristics.

For heterodyne signal processing ω_{LO} was chosen so $f_{LO} - f_{RF} \approx 100$ kHz. In this case $f_{LO} + f_{RF} = 2 f_{RF} + 100$ kHz and with suitable filtering this term and higher order ones can be eliminated. The IF output is then equal to:

$$\text{IF output} = B_1 \cos [2\pi(100 \text{ kHz})t + (\phi_{LO} - \phi_{RF})]$$

For quadrature phase detection ω_{LO} was set so $\omega_{LO} = \omega_{RF}$. In this case $\omega_{LO} - \omega_{RF} = 0$ and $\omega_{LO} + \omega_{RF} = 2\omega_{LO}$. With the proper filtering the $2\omega_{LO}$ terms and higher order ones can be eliminated producing an IF output equal to:

$$IF_{out} = B_1 \cos (\phi_{RF} - \phi_{LO})$$

For both systems this filter must not only reject the high frequency component but must also properly terminate them. If there exists a large SWR between the filter and IF mixer port, the mixer will generate troublesome harmonics.

The block diagram of a typical phase measureing system is shown in Figure A.I.3. First the local oscillator and RF signal are power split. One of the RF signals is next heterodyned with one of the local signals in mixer 1 and the IF output equals:

$$IF_1 = B_1 \cos\phi \quad \text{where} \quad \phi = \phi_{RF} - \phi_{LO} .$$

A 90° phase shift has been introduced in the local signal for mixer 2 and IF output for this device is:

$$IF_2 = B_1 \cos(\phi + 90°) = B_1 \sin\phi$$

If one takes the ratio of IF_2 to IF_1, the value of the phase is:

$$\phi = \arctan \frac{IF_2}{IF_1}$$

The magnitude of the RF signal is:

$$B_1 = (IF_1^2 + IF_2^2)^{1/2}$$

When double-balanced mixers are used as phase comparators, the most important specifications are:

1) DC offset
2) maximum DC output
3) isolation between ports
4) frequency response
5) temperature variation of DC offset.

If only one input is applied to the mixer then there should be no output signal at the IF port. However, due to slight mismatch in the diodes and imperfect balance in the transformer windings, a small DC offset voltage will appear at the IF port. For frequencies above 100 MHz wiring capacitance, transformer winding capacitance and physical location of the components will also upset the balance. Normally transformer tolerance is carefully controlled and the major contribution is the mixer's diodes. The value of the DC offset from the diodes varies with temperature and it is advantageous to select diodes whose characteristics track with temperature. This can be accomplished by using diodes manufactured from the same wafer. The Mini-Circuits ZAD-1 mixer uses this procedure and their units using Schottky diodes have a typical offset voltage of 1 mV. See Figure A.I.2 for the important specifications of this unit.[17] For applications as phase comparators, this offset effects the value of the absolute phase. If, for example two signals are 90° out of phase with respect to each other, then the phase detector output should be zero. However, with offset there will be a slight DC output and this would be interpreted as a phase difference other than 90°. A careful calibration procedure was followed in order to compensate for this problem.

DC offset can be measured statically or dynamically. For a static measurement the RF port must be terminated with 50 ohms and a signal must be applied only to the LO input. The DC at the IF port is the DC offset. The disadvantage of this approach is that it does not include offset contributed by the RF input signal. In a dynamic test the RF input frequency is shifted slightly from the LO frequency and the resulting phase difference is constantly varying from 0° to 360° at a rate equal to the frequency difference of the two sources. The phase detector output will be sinusoidal and the DC offset can be calibrated under typical operating conditions. This was the main method used in calibrating the phase and amplitude of the entire system (mixers, coax cables, amplifiers and attenuators).

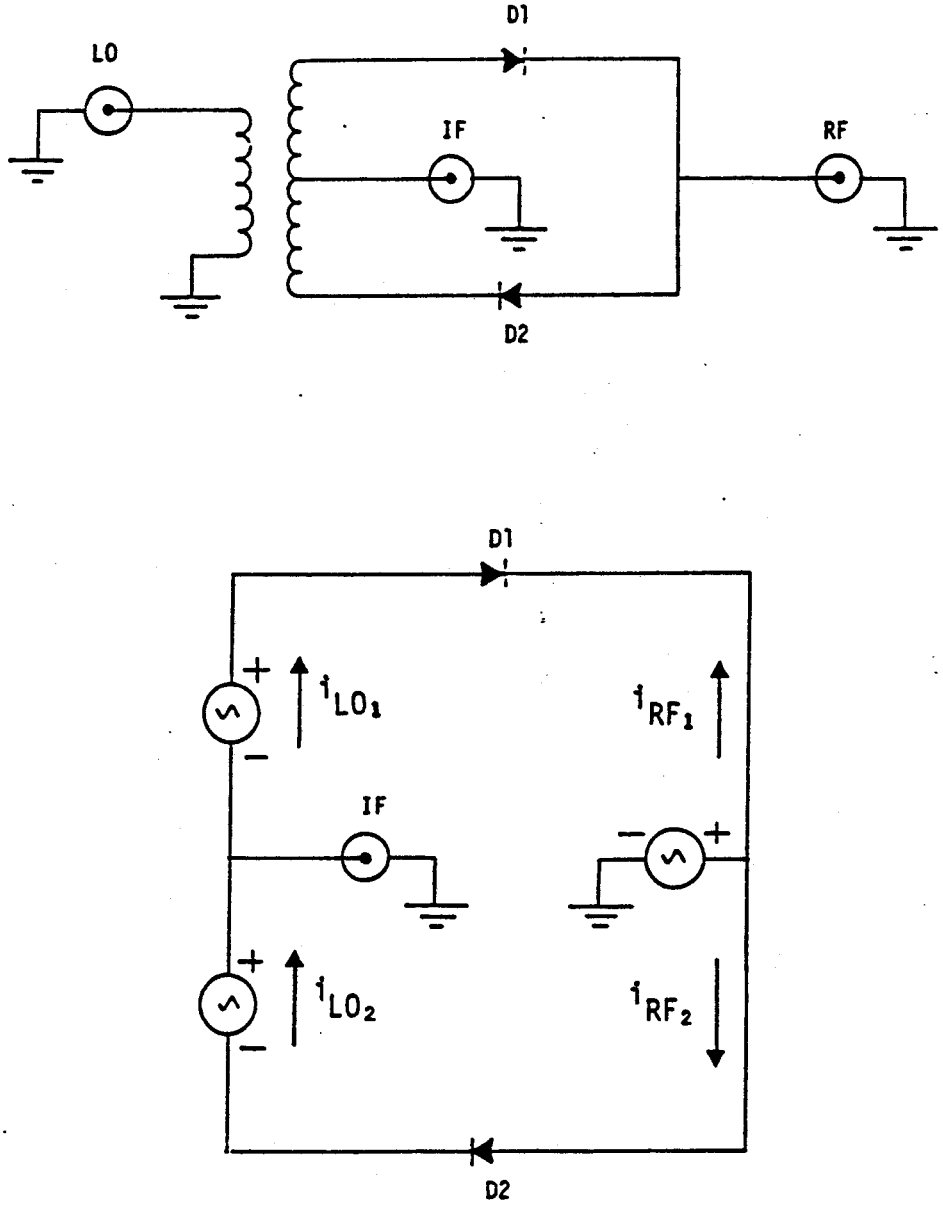

Figure A.I.1. Electrical model of a single-balanced mixer.

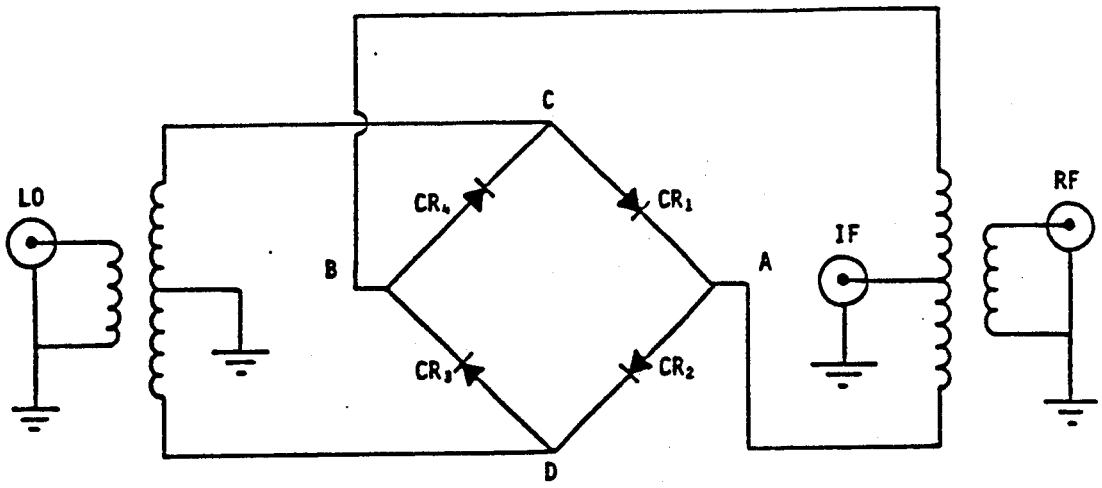

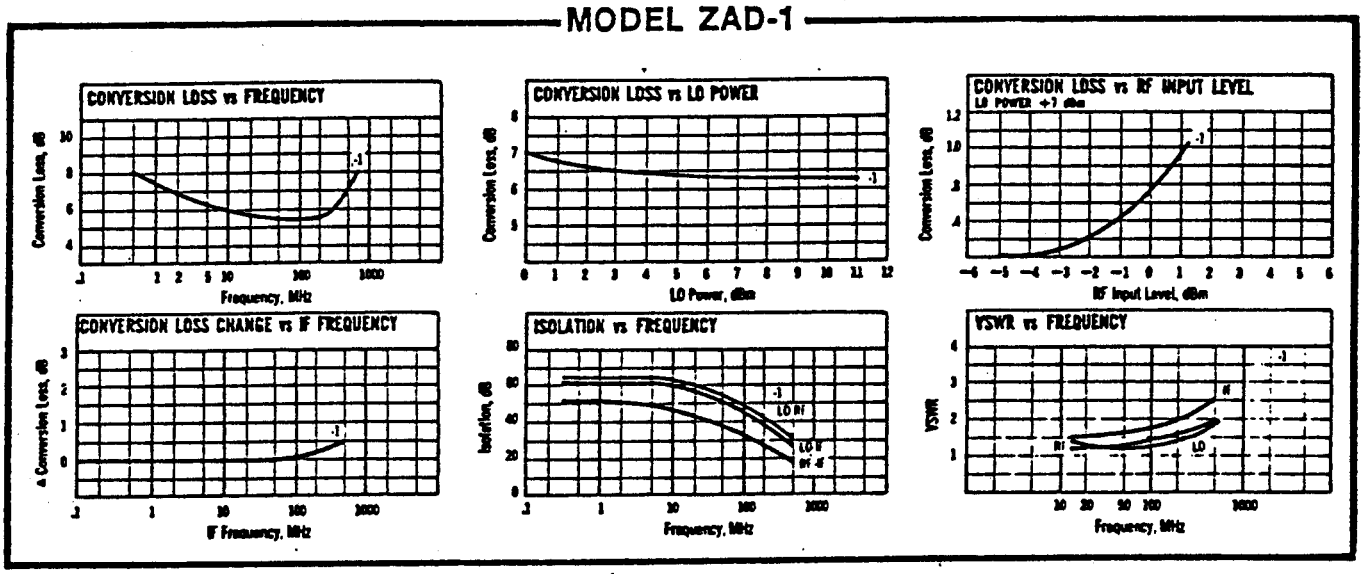

Figure A.I.2. Schematic of a typical double-balanced mixer. Also shown is the specifications of the ZAD-1 Mini Circuits mixer used in the experiment.

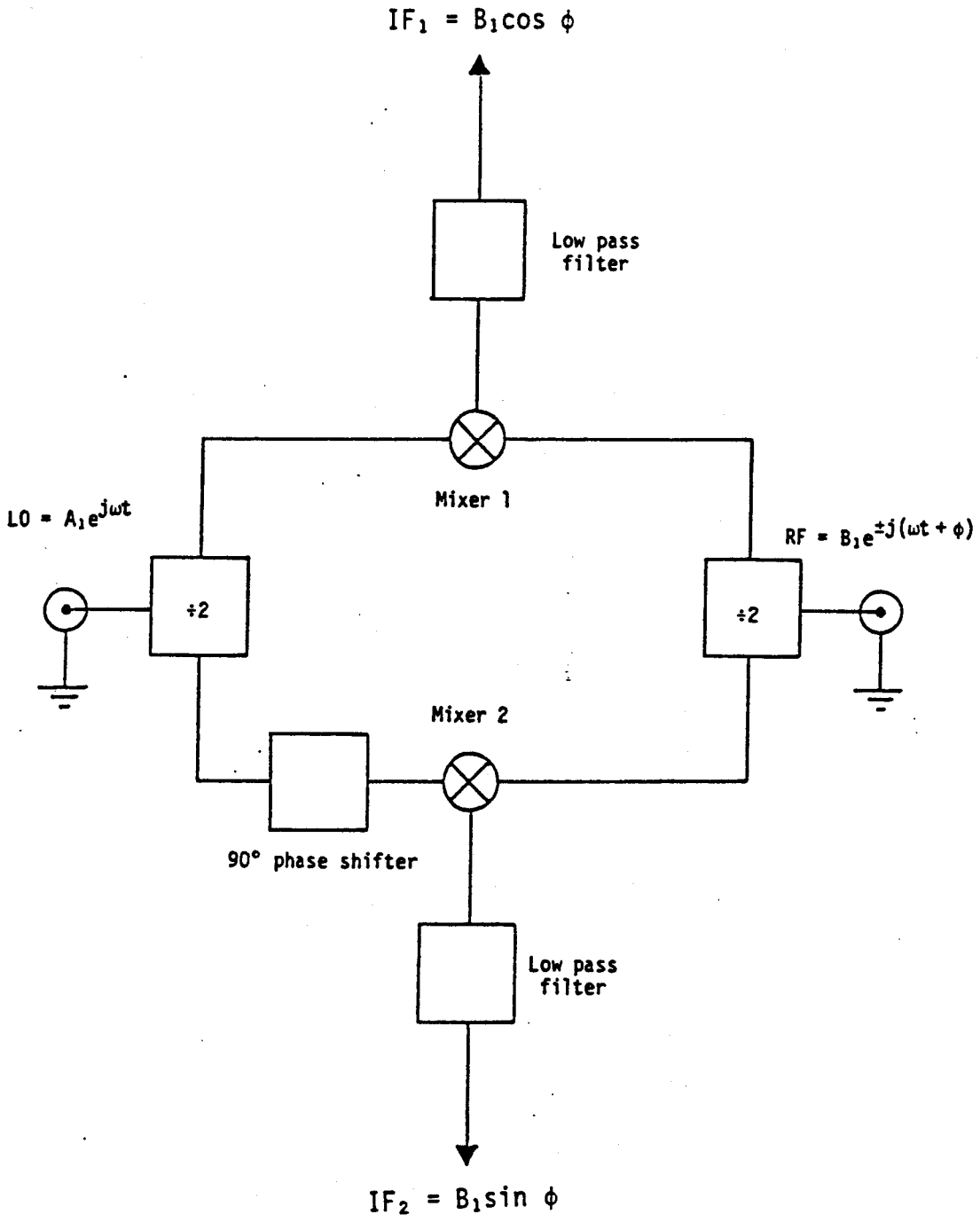

Figure A.I.3. Block diagram of a one channel quadrature phase detection system.

REFERENCES

1. Stix, T.H., Theory of Plasma Waves, McGraw-Hill, New York, 1962.

2. Allis, W.P., et al., Waves in Anisotropic Plasmas, MIT Press, Cambridge, Massachusetts, 1963.

3. Kraus, J.D. Carver, K.R. Electromagnetics, McGraw-Hill Book Co., 1973.

4. Parker, R.R. "Excitation and Propagation of Ion-Cyclotron Waves in a Plasma Column", Dept. Electrical Engineering, MIT, August 14, 1967, Ph.D. Thesis.

5. Walker, L.R. "Orthogonality Relation for Gyrotropic Wave Studies", Journal of Applied Physics, 28, No. 3 (1957).

6. Bresler, A.D. "Orthogonality Properties for Modes in Passive and Active Uniform Wave Guides", Journal of Applied Physics, 29, No. 5, May, 1958.

7. Stix, T.H. "Fast-Wave Heating of a Two-Component Plasma", Nucl. Fusion 737 (1975).

8. Paoloni, F.J. "Coupling to Fast MHD Eigenmodes in a Toroidal Cavity", PPPL, Princeton University, MATT-1119, May, 1975.

9. Perkins, F.W. "Heating Tokomaks Via the Ion-Cyclotron and Ion-Ion Hybrid Resonances", PPPL, Princeton University, Princeton, NJ, PPPL-1336, April, 1977.

10. Swanson, D.G. "Mode Conversion of Toroidal Alfven Waves", Phys. Fluids 18, 1269 (1975).

11. Takahashi, H. "ICRF Heating and Wave Generation in the ATC Tokamak", PPPL=1545, Princeton University, April, 1979.

12. Jackson, J.D., Classical Electrodynamics, John Wiley & Sons, Inc., 1962.

13. Gaudreau, M., Sansone, M., et al., "Medium Power ICRF Results on the Alcator A Tokamak", Proceedings of the Fourth Topical Conference on Radio Frequency Plasma Heating, Feb., 1981, Austin, Texas.

14. Sansone, M., et al., "The Alcator A ICRF Experiment", Bull. Am. Phys. Soc. 26, 930 (1981).

15. Scaturro, L.S., Kusse, B. "Electric Probe Measurements Near the Plasma Edge in Alcator", Alcator Internal Memo, #5, FBNML, MIT, 1977.

16. Paoloni, F.J. "Waveguide and Loop Coupling to Fast MHD Toroidal Eigenmodes", MATT-1173, Princeton, December, 1975.

17. "Signal Processing Components Guide", Mini-Circuits Co., CAT. 80-1, New York, NY, 1980.

PFC BASE LIST

INTERNAL MAILINGS (MIT)

G. Bekefi
36-213

A. Bers
38-260

D. Cohn
NW16-250

B. Coppi
26-201

R.C. Davidson
NW16-202

T. Dupree
38-172

S. Foner
NW14-3117

J. Freidberg
38-160

M.O. Hoenig
NW16-176

M. Kazimi
NW12-209

L. Lidsky
38-174

E. Marmar
NW16-280

J. McCune
31-265

J. Meyer
24-208

D.B. Montgomery
NW16-140

J. Moses
NE43-514

D. Pappas
NW16-272

R.R. Parker
NW16-288

N.T. Pierce
NW16-186

P. Politzer
NW16-286

M. Porkolab
36-293

H. Praddaude
NW14-3101

D. Rose
24-210

J.C. Rose
NW16-189

R.M. Rose
4-132

B.B. Schwartz
NW14-5121

R.F. Post
NW21-203

L.D. Smullin
38-294

R. Temkin
NW16-254

N. Todreas
NW13-202

J.E.C. Williams
NW14-3210

P. Wolff
36-419

T.-F. Yang
NW16-164

Industrial Liaison Office
ATTN: Susan Shansky
Monthly List of Publications
39-513

MIT Libraries
Collection Development
ATTN: MIT Reports
14E-210

B. Colby
PFC Library
NW16-255

EXTERNAL MAILINGS

International

Professor M.H. Brennan
Willis Plasma Physics Dept.
School of Physics
University of Sydney
N.S.W. 2006, Australia

Division of Plasma Physics
Institute of Theoretical Physics
University of Innsbruck
A-6020 Innsbruck
Austria

c/o Physics Section
International Atomic Energy Agency
Wagramerstrasse 5
P.O. Box 100
A-1400 Vienna, Austria

Laboratoire de Physique des Plasmas
c/o H.W.H. Van Andel
Dept. de Physique
Universite de Montreal
C.P. 6128
Montreal, Que H3C 3J7
Canada

Plasma Physics Laboratory
Dept. of Physics
University of Saskatchewan
Saskatoon, Sask., Canada S7N OWO

The Library
Institute of Physics
Chinese Academy of Sciences
Beijing, China

Mrs. A. Wolff-Degives
Kernforschungsanlage Julich GmbH
Zentralbibliothek - Exchange Section
D-5170 Julich - Postfach 1913
Federal Republic of Germany

Preprint Library
Central Research Institute for Physics
H-1525 Budapest, P.O. Box 49
Hungary

Plasma Physics Dept.
Israel Atomic Energy Commission
Soreq Nuclear Research Center
Yavne 70600
Israel

The Librarian (Miss DePalo)
Associazione EURATOM - CNEN Fusione
C.P. 65-00044 Frascati (Rome)
Italy

Librarian
Research Information Center
Institute of Plasma Physics
Nagoya University
Nagoya, 464
Japan

Dr. A.J. Hazen
South African Atomic Energy Board
Private Bag X256
Pretoria 0001
South Africa

EXTERNAL MAILINGS

National

Argonne National Laboratory
Argonne, IL 60439
ATTN: Library Services Dept.

Battelle-Pacific Northwest Laboratory
P.O. Box 99
Richland, WA 99352
ATTN: Technical Information Center

Brookhaven National Laboratory
Upton, NY 11973
ATTN: Research Library

U.S. Dept. of Energy
Washington, D.C. 20545
ATTN: D.O.E. Library

Roger Derby
Oak Ridge National Lab.
ETF Design Center
Bldg. 9204-1
Oak Ridge, TN 37830

General Atomic Co.
P.O. Box 81608
San Diego, CA 92138
ATTN: Library

Lawrence Berkeley Laboratory
1 Cyclotron Rd.
Berkeley, CA 94720
ATTN: Library

Lawrence Livermore Laboratory
UCLA
P.O. Box 808
Livermore, CA 94550

Oak Ridge National Laboratory
Fusion Energy Div. Library
Bldg. 9201-2, ms/5
P.O. Box "Y"
Oak Ridge, TN 37830

Dr. D. Overskei
General Atomic Co.
P.O. Box 81608
San Diego, CA 92138

Princeton Plasma Physics Laboratory
Princeton University
P.O. Box 451
Princeton, NJ 08540
ATTN: Library

Plasma Dynamics Laboratory
Jonsson Engineering Center
Rensselaer Polytechnic Institute
Troy, NY 12181
ATTN: Ms. R. Reep

University of Wisconsin
Nuclear Engineering Dept.
1500 Johnson Drive
Madison, WI 53706
ATTN: UV Fusion Library